

DISSERTATION ZUR ERLANGUNG DES DOKTORGRADES DER FAKULTÄT FÜR CHEMIE UND
PHARMAZIE DER LUDWIG-MAXIMILIANS-UNIVERSITÄT MÜNCHEN

Nanoparticles and human health

**Development and application of an experimental strategy to
estimate cytotoxicity of nanoparticles**

Julia Blechinger

aus

München, Deutschland

2012

DISSERTATION ZUR ERLANGUNG DES DOKTORGRADES DER FAKULTÄT FÜR CHEMIE UND
PHARMAZIE DER LUDWIG-MAXIMILIANS-UNIVERSITÄT MÜNCHEN

Nanoparticles and human health

**Development and application of an experimental strategy to
estimate cytotoxicity of nanoparticles**

Julia Blechinger

aus

München, Deutschland

2012

Erklärung

Diese Dissertation wurde im Sinne von §7 der Promotionsordnung vom 28. November 2011 von Herrn Prof. Dr. Christoph Bräuchle betreut.

Eidesstattliche Versicherung

Diese Dissertation wurde eigenständig und ohne unerlaubte Hilfe erarbeitet.

München, 09.08.2012

Julia Blechinger

Dissertation eingereicht am	09.08.2012
1. Gutachter:	Prof. Dr. Christoph Bräuchle
2. Gutachter:	Prof. Dr. Achim Wixforth
Mündliche Prüfung am	01.10.2012

Für meine Eltern und Ondrej

Abstract

The potential toxicity of nanoparticles currently raises many discussions in public and scientific life. The question whether nanoparticles are a threat to human health cannot be answered to complete satisfaction at the current state of knowledge. A versatile tool to investigate nanotoxicity are fluorescence microscopy and live-cell imaging as they provide excellent resolution and direct insight into cellular processes. In this work fluorescence based methods are used to investigate the influence of silica nanoparticles on human health, more precisely on the blood vessel system.

At first, the synthesis and characterization of the following three different types of perylene labeled amorphous SiO₂ nanoparticle species is described: surface-labeled monodisperse particles, particles with a dye-containing silica core and a non-fluorescent silica shell and a surface-labeled nanoparticle network. The labeling of nanoparticles should not induce artificial cytotoxic effects when they are used for cytotoxicity assessment. This is achieved either by incorporating the dye into the nanoparticle's structure or by covering only a minor surface fraction by dye molecules. The surface-labeled silica species are used to investigate nano-toxicity throughout this thesis.

Another prerequisite for reliable dose-dependent nanotoxicity studies is the knowledge about the number of nanoparticles taken up by an individual cell. We therefore developed the Nano_In_Cell_3D ImageJ macro which is able to quantify nanoparticle uptake into cells. Nano_In_Cell_3D uses the fluorescence image of the cell membrane to segment the cell into an intracellular space, a transition region (e-membrane region) and an extracellular space. The number of present nanoparticles is calculated from the fluorescence intensity of each region. This custom-made method offers the possibility to quantify nanoparticles in the individual cellular regions. Nano_In_Cell_3D was validated by comparing the results to the well established quenching method.

By using Nano_In_Cell_3D we could show that the cytotoxic impact of nanoparticles onto different cell lines correlates to their intracellular uptake. Primary human vascular endothelial cells (HUVEC) take up 310 nm silica nanoparticles more efficiently and are more sensitive to this nanoparticle species than cancer cells derived from the cervix carcinoma (HeLa). Upon nanoparticle contact, cellular viability of HUVEC is strongly reduced and membrane permeability increases leading to apoptosis. In contrast, HeLa cells show a considerable lower effect in both cellular viability and membrane permeability and do not show apoptosis. In consistence to these findings, HUVEC take up approximately 20 times more particles than HeLa cells within 4h. Interestingly nanoparticle uptake is clathrin mediated in both cell types.

HUVEC grow in the blood vessel system under natural conditions and are therefore exposed to blood flow conditions. The latter can be simulated using a microfluidic system. We chose a microfluidic system based on the surface acoustic wave (SAW) technology which was characterized concerning fluid evaporation behavior, fluid temperature and flow velocities. Based on these results the system can be further improved to allow the assessment of nanotoxicity at blood flow conditions in a next step.

The last part of the thesis focuses on interactions between silica nanoparticles and giant unilamellar vesicles (GUV)s. The latter serve as a simple model for the cell membrane. Nanoparticles in contact with the lipid membrane influence the morphological behavior of the vesicles during phase transition. In absence of nanoparticles, vesicles typically show extracellular budding processes. Nanoparticles

in contact with the cell membrane induce intravesicular budding of daughter vesicles, similar to endocytosis observed in living cells. Furthermore exocytosis processes were observed where daughter vesicles crossed the GUV membrane and were transferred from the intravesicular to the extravesicular space. These observations suggest that the fundamental mechanism of endocytosis can partly be explained by simple physical effects.

In summary, this theses provides an experimental strategy to investigate the impact of nanoparticles onto human cells using SiO₂ nanoparticles as an example. Starting with the synthesis and characterization of nanoparticles it tackles the question how to quantify nanoparticle uptake into cells. Furthermore we could prove that cytotoxic effects can be correlated to nanoparticle uptake and were able to show that nanoparticles influence artificial membranes which is a first step to understand the basic mechanisms of nano-toxicity. The methodology developed in this thesis is expected to provide insight into cytotoxicity of a broad variety of different nanoparticle types.

Contents

Abstract	vii
1 Introduction	1
2 Nanoparticles	3
2.1 Sources of nanoparticles	5
2.1.1 Nanoparticles of natural origin	5
2.1.2 Artificial nanoparticles	5
2.2 Risk assessment of nanoparticles	6
2.2.1 Uptake of nanoparticles into the human body	6
2.2.2 Molecular basis of nanoparticle cytotoxicity	8
2.2.3 The challenge of nanoparticle-risk assessment studies	11
2.2.4 State of the art cytotoxicity of amorphous silica nanoparticles	12
2.3 Methods for nanoparticle characterization	16
2.3.1 Size and morphology	16
2.3.2 Zeta potential	17
3 Fluorescence techniques	21
3.1 Molecular excitation and relaxation processes leading to fluorescence	21
3.2 Fluorescence quenching	23
3.3 Fluorescence anisotropy	24
3.4 Fluorescence microscopes	27
3.4.1 Widefield microcopy	27
3.4.2 Confocal microscopy and confocal spinning disk microscopy	29
3.4.3 Experimental setups	30
4 Cellular internalization pathways	33
4.1 Phagocytosis	33
4.2 Pinocytosis	33
4.2.1 Macropinocytosis	33
4.2.2 Clathrin-mediated endocytosis	34
4.2.3 Caveolin-mediated endocytosis	34
4.2.4 Clathrin- and caveolin-independent processes	35
4.3 The role of the actin and tubulin networks	35
5 Synthesis and characterization of SiO₂ nanoparticles	37
5.1 Synthesis of perylene labeled Silica nanoparticles	37
5.2 Transmission electron microscopy analysis	40
5.3 Overlay of TEM and fluorescence widefield images	40

Contents

5.4	Fluorescence emission spectra	41
5.5	Fluorescence anisotropy	43
5.6	Cellular uptake	46
5.7	Number of dye molecules per nanoparticle	46
5.8	Terminology of the particles used in this work	51
5.9	Summary and conclusions	51
6	Image analysis by Nano_In_Cell_3D	53
6.1	The Nano_In_Cell_3D ImageJ macro	54
6.1.1	Three-dimensional reconstruction of the cellular ROI	54
6.1.2	Input of analysis parameters	56
6.1.3	Nanoparticles assignment to different regions according to cell position	57
6.1.4	Analysis of nanoparticles and results	57
6.1.5	Auxiliary routines	59
6.2	Setting of parameters and validation of Nano_In_Cell_3D	59
6.2.1	Threshold and intensity of individual nanoparticles	60
6.2.2	E-membrane width	66
6.2.3	Absolute number of nanoparticles	66
6.2.4	Validation of Nano_In_Cell_3D by comparison to quenching experiments	68
6.3	Summary and conclusions	69
7	SiO₂ nanoparticles and cells	71
7.1	Nanoparticle characterization	71
7.2	Quantification of cellular nanoparticle uptake	72
7.3	Uptake pathways	75
7.3.1	Clathrin mediated endocytosis	76
7.3.2	Dependency of nanoparticle uptake on the actin and tubulin networks	79
7.4	Correlation of nanoparticle uptake to cytotoxicity	80
7.4.1	Dose-dependent cytotoxicity of silica nanoparticles	80
7.4.2	Influence of the perylene-surface functionalization on the toxicity of silica nanoparticles	82
7.4.3	Silica nanoparticle-induced cell death	82
7.5	Summary and conclusions	85
8	Microfluidic system	87
8.1	Design and working principle	87
8.2	Assembly of the microfluidic system	88
8.3	Characterization and adaption to live-cell imaging requirements	89
8.3.1	Fluid evaporation from the microfluidic channel	89
8.3.2	Temperature characteristics	90
8.3.3	Flow rates	92

8.4	Summary and conclusion	93
9	Interaction of nanoparticles with lipid vesicles	95
9.1	Lipid membranes and giant unilamellar vesicles	95
9.2	Experimental details	96
9.3	Observations and discussion	97
9.3.1	Phase transition of giant unilamellar vesicles	97
9.3.2	Phase transition of giant unilamellar vesicles in the presence of nanoparticles	98
9.4	Summary and conclusions	101
	Bibliography	103
	Appendix: Deposition of Nanoparticles	117
	Acknowledgements	125
	List of publications	127

1 Introduction

“The dwarfs are with us” (Die Zwerge sind unter uns) was the title of a newspaper article published in the German journal Stern in may 2011 [1]. The author uses the term dwarfs as a synonym for all kinds of nanoparticles thereby referring to the small size of this material type. In the article, the author claims that nowadays nanoparticles are incorporated into a broad variety of commercially available products without knowing their potential harm to human health. Furthermore, as no obligation for indication exists up to now, customers cannot recognize whether a product contains nanoparticles or not. This points out a serious problem that has come into existence with the vast development in nanotechnology throughout the last years. On the one hand, research aiming at synthesis and development of nano-related products was generously funded by industry and governments whereby on the other hand, only minor attention was given to risk assessment. This disequilibrium might change slowly as the awareness of potential nano-risks is increasing. At the end of 2006, the German government founded the “Nano-Kommission” where representatives of science, economy, environmental and consumer associations, labor unions and of the government tried to develop the main principles for a responsible handling of nanotechnologies. But, following the opinion of the “Bund für Umwelt und Naturschutz”, one of the big German environmental organizations, this aim was not reached. Also within the European union and on an international basis nano-safety is widely discussed and attempts for developing a generally accepted handling procedure for nanoparticles are made. Nevertheless, a strict legislation for nanotechnology and nanoparticles is a distant prospect as main basic agreements, like a standardized definition for the term “nano” and appropriate test procedures to estimate the risk of nanoparticles are still missing [2]. The investigation of nanoparticle’s impact on human health is long overdue and reliable test systems accounting for the special properties of nanomaterials need to be developed. For this reason, the Deutsche Forschungsgemeinschaft DFG has created in 2007 the priority program SPP 1313 - “biological responses to nanoscale particles”. The main aim of this project is to “identify and understand the elementary physical, chemical and biological processes by which manufactured nano-sized particles cross the phase boundaries of biological systems, interact with biomolecules, cells and cell constituents as well as affect their biological functions” [3]. One of the projects enclosed is called NPBIOMEM. It was founded to investigate the bioactivity and cellular uptake of distinct nanoparticles in human endothelial cells. It deals with the question by which mechanism and how efficiently nanoparticles can enter these cells, and how cellular viability is influenced by nanoparticle impact. Endothelial cells, which cover the walls of the blood vessel system, play an important role in human health as they partly control blood flow, blood pressure, inflammation and coagulation. Any disturbance of these regulatory processes can have major impact on human health. Nanoparticles, having crossed the physiological barriers like the lung, skin or gastro-intestinal tract, reach the blood vessel system

1 Introduction

where they can interact with the endothelial cells and affect their viability. The experimental strategy of the MPBIOMEM project is to use commercially relevant nanoparticles, optimized for live-cell imaging, and to investigate their interplay with human vascular endothelial cells (HUVEC) from a biological and a physical point of view. HUVEC are primary cells, extracted from the umbilical cord. The natural blood flow conditions for these cells will be simulated by a microfluidic device incorporated into the experiments.

In this thesis, which is part of the NPBIOMEM project, the synthesis and characterization of nanoparticles which are suitable for live-cell imaging cytotoxicity investigations is discussed. Furthermore nanoparticle cell interactions are investigated by quantifying nanoparticle uptake into cells and by characterizing their uptake pathway and cytotoxicity. In addition, the impact of nanoparticles on artificial cells is monitored to learn about the basic physical principles influencing this process. Furthermore, the microfluidic system is characterized. The project was done in close cooperation with the groups of Prof. A. Reller (University of Augsburg; synthesis and characterization of nanoparticles), Prof. A. Wixforth (University of Augsburg; microfluidic system and lipid membranes), Prof. M. Schneider (Boston University; microfluidic system), Prof. S.W. Schneider (University of Mannheim; endothelial cells, cytotoxicity) and Prof. C. Bräuchle (Ludwig-Maximilians-Universität Munich; nanoparticle characterization and live-cell imaging).

This work is structured as follows: After the introductory **Chapter 1** natural as well as artificial sources of nanoparticles are highlighted in **Chapter 2**. Furthermore uptake pathways of nanoparticles into the human body, the molecular basis of nanoparticle cytotoxicity and the challenge of nanoparticle risk assessment studies are shown and the current knowledge about cytotoxicity of SiO₂ nanoparticles are summarized. The chapter closes with a description of methods for nanoparticle characterization. In **Chapter 3** fluorescence as well as fluorescence based methods are explained and the microscopy techniques used in this work are described. **Chapter 4** contains a brief summary about cellular internalization pathways. In the following **Chapters 5 - 9** the experiments and outcomes of this work are presented in a partly cumulative way. Synthesis and characterization of the used SiO₂ nanoparticles are described in **Chapter 5**, which is based on a paper published in Small [4]. In **Chapter 6** the custom made ImageJ macro *Nano_In_Cell_3D* is presented which allows quantifying nanoparticle uptake into cells. This part is based on a paper submitted to Nanomedicine [5]. This ImageJ macro was used to quantify nanoparticle uptake into HeLa and HUVEC cells as is shown in **Chapter 7**. Furthermore nanoparticle uptake pathways and the cytotoxic impact of SiO₂ nanoparticles on both cell lines are investigated. A publication of this work was recently submitted to Small [6]. In a further project, a microfluidic system designed for live-cell imaging applications was characterized. The results are discussed in **Chapter 8**. The interaction of nanoparticles with lipid vesicles, as a model system for the cell membrane is addressed and pure physical effects of nanoparticle membrane interactions are described in **Chapter 9**.

2 Nanoparticles

Since several years, the prefix “nano” is used to form catchwords for publications and advertisements, indicating innovative new products with sophisticated properties. The term “nano” is derived from the Greek word “nanos”, meaning dwarf [8, 9]. This implies that “nano”-products contain very small building blocks, the nanomaterials. Outer or inner dimensions of these nanomaterials are in the nanometer range ($1\text{nm} = 10^{-9}\text{m}$). As shown in Figure 2.1 the vast field of nanomaterials can be classified into subgroups, starting with nanoobjects and nanostructured materials. These two groups are distinguished by either having nanoscaled outer (nanoobjects) or inner dimensions (nanostructured materials). The latter include nanoporous systems and nanofoams. The subgroup of nanoobjects is further divided into nanoplates (nanoscale in one dimension), nanofibers (nanoscale in two dimensions) and nanoparticles (nanoscale in three dimensions). Due to their size, nanoparticles form the transitional zone between individual atoms or molecules and the corresponding bulk materials [10]. As they have a very high surface-to-volume ratio, most of their atoms are located on their surface and the behavior of the surface atoms dominates the physics and chemistry of the particle [11]. Compared to bulk materials, the reduced size of nanoparticles leads to discontinuous crystal planes followed by an increase of structural defects disrupting the well structured electronic configuration of the material [10]. This is the reason why nanoparticles e.g. show high turnover rates when used in catalysis or have soil-repellent surfaces. Furthermore, nanoparticles can form optically transparent layers or become superparamagnetic. Another effect observed is the so called size-dependent quantum effect. Due to their small dimensions the energy levels of the particles are not discrete but rather dispersed bands. Therefore nanoparticles, called semiconductor quantum dots, have a size-dependent color and luminescence. These special properties are the reason why nanoparticles are very interesting for novel applications and are increasingly used in industry and science [9].

Due to their vast spread and to emerging concerns about nano-safety many different definitions for nanoparticles have been developed trying to define a universally valid size range for the use of the term “nanoparticle”. National and international institutions, like ISO, OECD, BSI and DIN assigned the term nanoparticle to particles with diameters between 1nm and 100nm. Nevertheless, other organizations claim that the biological effects of particles are not restricted to this size range and that particles of 300 nm or even 500 nm could just as well affect human health [7]. A strict limitation of the term nanoparticles to a special size range is therefore questionable, especially when considering their chemical, physical and biological effects [7, 9]. For this reason all nanometer sized particles used in this work are termed nanoparticles.

2 Nanoparticles

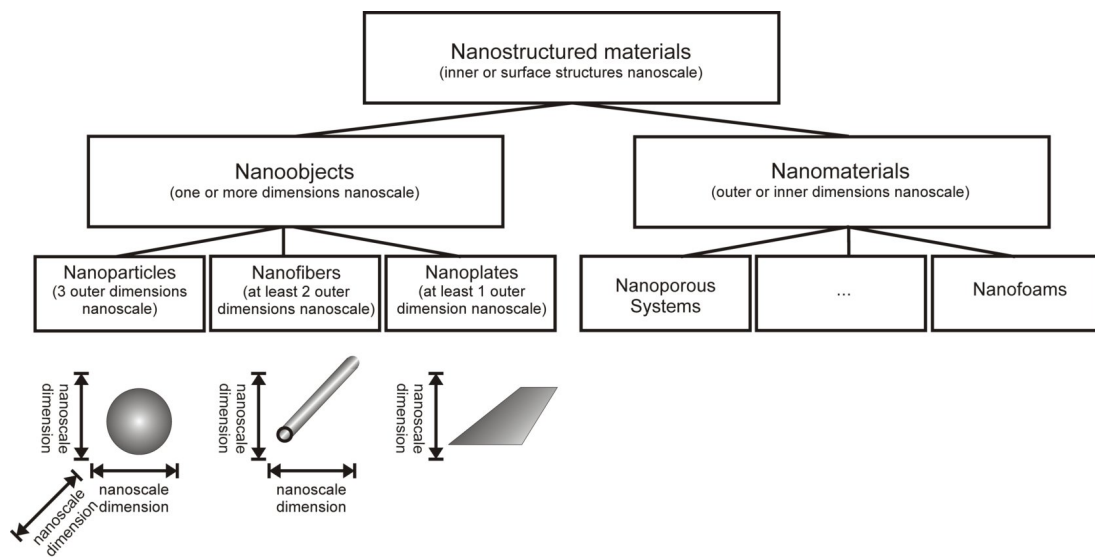


Figure 2.1: Classification of nanostructured materials into several subtypes. Depending on their morphology, nanostructured materials are classified as nanoobjects (nanoscaled outer structure) or nanomaterials (nanoscaled inner structure). Nanoobjects are further divided into nanoplates (one nanoscaled outer dimension), nanofibers (two nanoscaled outer dimensions) or nanoparticles (all dimensions in the nanoscale). In contrast to nanoobjects, the outer dimensions of nanomaterials are not necessarily restricted. This material class is defined by a nanoscaled inner structure like present in nanoporous systems or nanofoams. The scheme was adapted from [7].

2.1 Sources of nanoparticles

The current nano-hype gives the impression that nanoparticles are a recent achievement of science. This is not true as nanoparticles have been produced by natural processes since the beginning of earth and are omnipresent in the environment. Only in the recent years, modern science has discovered the advantages of nanoparticles and learned to synthesize and design them at will. A short overview about the origin and distribution of both natural and synthetic nanoparticles is given in the next sections.

2.1.1 Nanoparticles of natural origin

About 90% of nanoparticles have natural origin [12]. Natural nanoparticle sources include erosion, terrestrial dust storms, fires, volcano eruptions and ocean as well as fresh water evaporation. The largest source for environmental nanoparticles are dust storms, mainly occurring in areas like the Salton Sea, Patagonia or the Sahel region. Particles produced in a dust storm have sizes from 100 nm to several μm [8, 12]. Like dust storms, forest and grass fires can spread ash and smoke over thousands of square miles. The latter occur predominantly in the savannas of Africa, Australia, Brazil, North America, Europe and Asia [8]. Another nanoparticle source are volcanoes, ejecting up to $30 \cdot 10^6$ tons of ash during a single eruption. The nano- to micrometer sized particles contained in the ash and gases can reach heights over 1800 m [12]. Nanoparticles are also formed from ocean and fresh water evaporation or when wave-produced water drops are ejected into the atmosphere. The latter are called sea salt aerosols [12, 13]. Evaporation produced particles have sizes from 100 nm to several μm [8]. Nanoparticles of natural sources have been related to diverse health effects like asthma, emphysema or eye and skin irritations as well as diseases of lympho-endothelial origin [12]. Interestingly, sea salt aerosols cannot be correlated with adverse health effects but seem to be healthy for patients with respiratory diseases [14].

2.1.2 Artificial nanoparticles

Human-made nanoparticles provide approximately 10% to all environmental nanoparticles [12]. Sources of human-made nanoparticles include cooking, cars, industry and chemical manufacturing. Although the fraction of man-made nanoparticles seems negligible compared to nanoparticles from natural sources, their importance concerning health considerations should not be underestimated. Human-made nanoparticles are especially designed and produced for the incorporation into commercial products [8]. Therefore they are often in very close or direct contact with the human body. Nanoparticles are for instance added to sunscreen, paints, soaps or detergents. They can furthermore be contained in electronic devices or pharmaceuticals [15, 16]. Common commercially used nanoparticles are composed of silicon dioxide, titanium dioxide, zinc oxide, silver, gold or carbon-containing compounds. Silica nanoparticles, which were investigated in this work, are used as solid lubricants, in cleaning agents, paint, drugs, or cosmetic products like makeup or sunscreens [8, 15, 16]. If sandwiched between two glass panels, silica monolayers made of fumed silica nanoparticles render windows fireproof. The addition of silica nanoparticles to concrete densifies it's

2 Nanoparticles

micro and nanostructure improving the mechanical properties. Furthermore silica nanoparticles, in combination with alumina nanoparticles are incorporated into hydrophobic polymers, generating a water repellent coating similar to the surface of lotus leaves [17].

2.2 Risk assessment of nanoparticles

Nanoparticles are an ubiquitous part of human life. Being surrounded by nanoparticles a close contact with this type of materials is unavoidable for humans and can happen in both an intended or unintended way. We e.g. apply nanoparticles onto the skin when using cosmetic products, inhale or swallow them. Once nanoparticles crossed the physiological barriers like lung, skin or gastrointestinal tract, they can interfere with cellular structures and biological processes of the human body. The concern for potential toxicological effects of nanoparticles on humans has increased during the last years [18] and the need for well structured studies dealing with risks and chances of nanoparticles raises constantly [19–21]. But nanoparticle cytotoxicity studies are challenging as it is not always possible to transfer the well established characterization methods used for new chemicals to nanoparticle risk assessment. The special properties of nanomaterials have to be taken into account and may interfere with standardized methods, asking for new parameters to be considered. In the following possible nanoparticle uptake routes into the human body and the molecular basis of nanoparticle-cell-interactions will be discussed. In addition, the challenges of nanoparticle-risk assessment are further described.

2.2.1 Uptake of nanoparticles into the human body

Nanoparticles can be taken up into the human body throughout a variety of different pathways including the lung, the gastro-intestinal tract or the skin. The lung is the most common way for nanoparticle uptake. It consists of airways and aveoli (see Figure 2.2). The airways transport the air in and out of the lungs whereas the alveoli are the gas exchange areas [22]. Approximately 300 millions alveoli are contained in the human lung having a total surface of around 140 m^2 . Within the alveoli, an only few nanometer thick barrier of epithel- and endothel cells separates air and blood [7, 22]. In general, spherical nanoparticles with an aerodynamic diameter of less than $10 \text{ }\mu\text{m}$ can be inhaled. The smaller their size, the further they can travel into the lung. Nanoparticles with sizes below $2.5 \text{ }\mu\text{m}$ can reach the alveoli and particles with sizes less than 100 nm are also mainly deposited into the alveolar region [22]. If foreign material is inhaled, it is usually removed from the airways by mucociliary clearance. Inside the alveoli, where mucociliary clearance is not possible, foreign material is taken up by macrophages [7]. Whether particles stay in the lung or whether they are cleared depends mostly on their mass, their size an on their surface [23]. Less than 0.05% of nanoparticles that are inhaled are translocated into the blood, depending on the physical-chemical properties of the particles [7, 24]. Nevertheless several experiments showed that this fraction is enough to find a considerable number of particles within the blood [25–28].

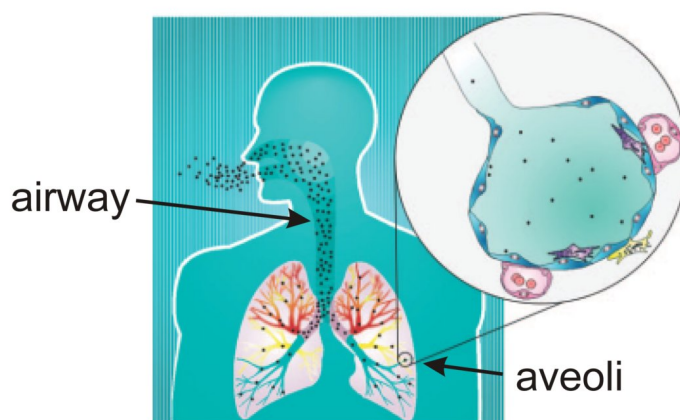


Figure 2.2: Scheme of the respiratory system. NP taken up into the lung cross the airways before reaching the aveoli which are the gas exchange areas. The interface between aveoli and blood consists of an only few nanometer thick barrier of epithel- and endothel cells. NPs are cleared from aveolis by macrophages. This figure was adapted from [7].

Another portal for nanoparticle uptake into the human body is the gastro-intestinal tract. Nanoparticles can either enter via nutrients or by swallowing particles that are ejected from the lungs via mucociliary clearance. The gastro-intestinal tract, which is drafted in Figure 2.3, is a very complex barrier system with a surface area of up to 200 m². The epithelial cells on the surface of the intestine mediate the uptake of nutrients into the blood flow. The intestinal epithelial cells and the blood vessels are separated by several cell layers hindering the uptake of macromolecules or nanoparticles [7]. Nevertheless, the uptake of particulate matter by the gastrointestinal epithelium is widely accepted [22, 29]. Uptake of inert particles was shown to occur trans- or para-cellularly, at Peyer's Patches (aggregations of lymphoid tissue) or via M-cells. The latter are microfold cells which are specialized in transporting particles and organisms from the gut lumen to immune cells across the epithelial barrier [7].

A third passage way for nanoparticle uptake is the skin. Its total surface area adds up to 1.5-2 m². The skin is composed of the three layers: epidermis, dermis and subcutis (see Figure 2.4). The epidermis is composed of a 5-20 μm thick layer of dead keratinocytes and two layers of living cells. Dead cells from these two layers constantly replace the dead keratinocytes. The underlying dermis contains hair follicles and sebaceous glands. It is followed by capillary vessels [7, 30]. The most investigated particle type concerning uptake via the skin are TiO₂ nanoparticles as they are contained in sunscreen and therefore commonly applied onto the skin. Up to now, different types of TiO₂ nanoparticles were found to pass the upper layers of the epidermis and were present in hair follicles or wrinkles. None were found in deeper skin regions [7, 31, 32]. By contrast, studies with 70 nm SiO₂ nanoparticles showed that these particles translocate into the lymph nodes, the liver, the hippocampus and cerebral cortex after topical applications inside the ears of mice [33]. After crossing physiological barriers, nanoparticles reach the blood vessel system. Once inside the blood

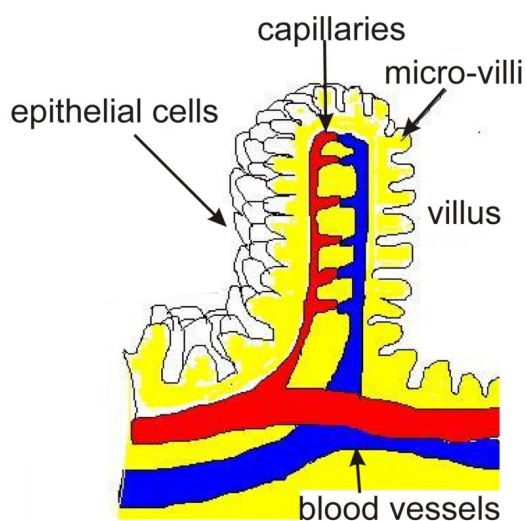


Figure 2.3: Scheme depicting a section of the gastro-intestinal tract. The intestine is covered by villi which in turn are covered with microvilli. This surface structure results in a surface area of up to 200 m^2 . The blood vessels in the villi are separated from the intestinal epithelial cells by several cell layers. The figure was adapted from [22].

they can be transported to every part of the human body. Until now, the uptake of nanoparticles from the blood vessel system into cellular target structures has hardly been investigated. This work aims to unravel the basic mechanisms of nanoparticle uptake from the blood vessel system and to link this process to possible cytotoxic effects. We chose to investigate the interactions between nanoparticles and endothelial cells, the cells covering inner surface of the blood vessel system, as a main project throughout this work.

2.2.2 Molecular basis of nanoparticle cytotoxicity

Once inside the human body, nanoparticles have access to a variety of biological components like cells or proteins. Each of these components is a potential target and might interact with the foreign substance. The interaction of nanoparticles with any biological environment is very complex as its nature is influenced by nanoparticle properties like chemical composition, shape, angle of curvature, porosity, surface crystallinity, functionalization and roughness as well as charge, state of aggregation and stability [10, 34]. In addition, nanoparticles carry the fingerprint of their synthesis. This means that all individual components like ligands or solvents having contact with the particles during synthesis or purification leave their traces on the nanoparticles, influence their surface and therefore their reactivity [35]. As soon as nanoparticles interact with biological fluids like blood, plasma or the interstitial fluid, their surface gets covered by proteins creating a biological interface. This protein corona has been subject to several studies throughout the last years, all showing that the formed corona is unique for each particle type and biological medium [34, 36, 37]. Its composition

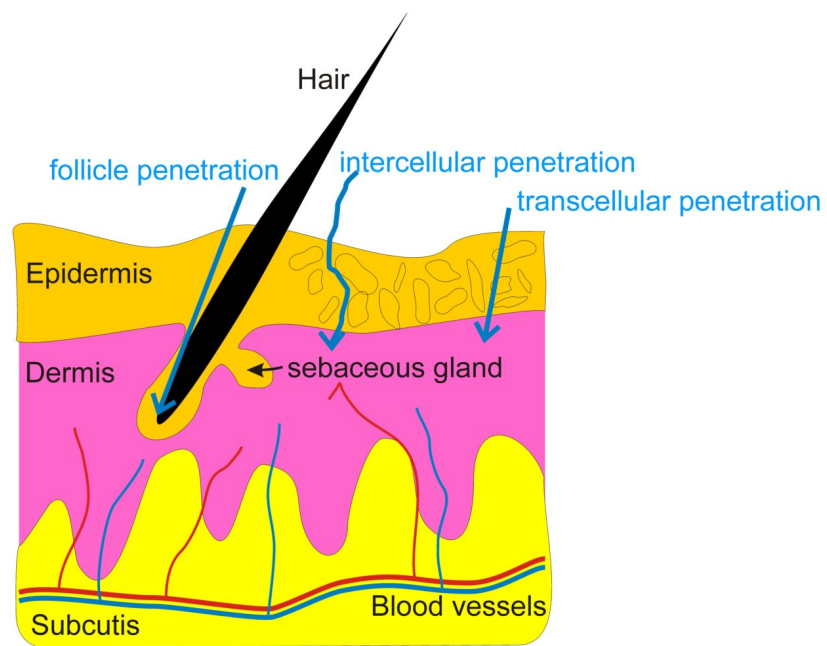


Figure 2.4: Scheme of the skin. It consists of three layers. The outer layer is the epidermis, formed by keratinocytes. It is followed by the dermis containing hair follicles and sebaceous glands. The lowest layer is called subcutis. It contains connective and adipose tissue and encloses the blood vessels. In theory, particles can cross the skin by intercellular, transcellular or by follicle penetration. By now particles were only found in hair follicles or wrinkles but not in deeper skin regions [31].

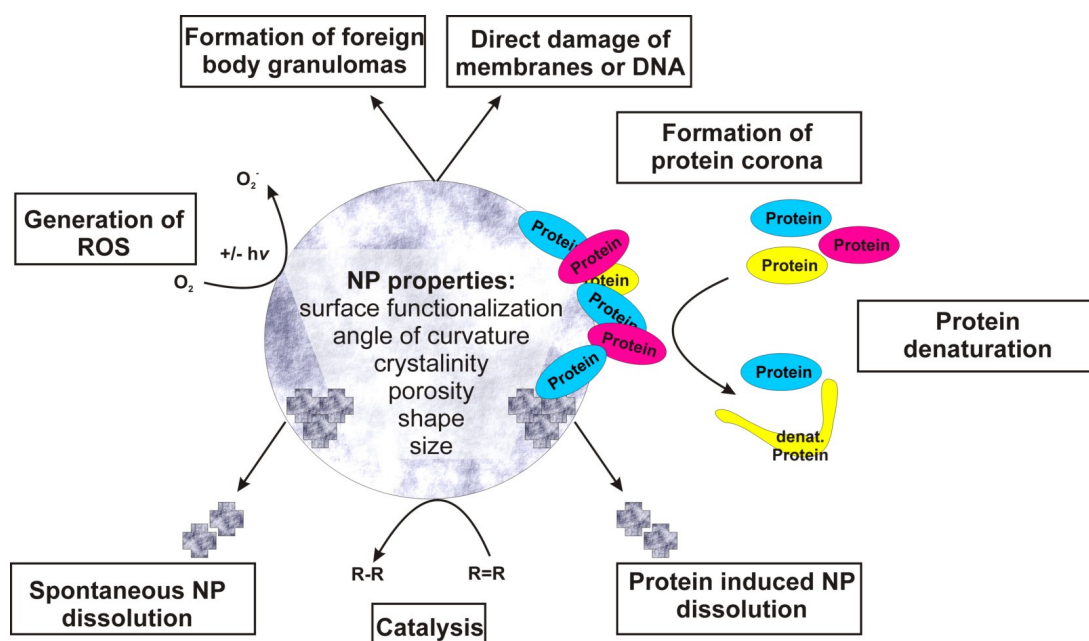


Figure 2.5: Scheme of nanoparticle interaction with their environment. The interaction is governed by specific particle properties including surface functionalization, angle of curvature, crystallinity, porosity, shape and size. Being in contact with proteins, a protein corona can be formed around the nanoparticles, nanoparticles can denature the proteins or the proteins might induce nanoparticle dissolution in addition to spontaneous nanoparticle dissolution. Furthermore the nanoparticle surface can have catalytic properties and e.g. induce ROS production. Nanoparticles might as well induce the formation of foreign body granulomas or directly damage membranes or DNA.

changes constantly in dependency on the local environment, modifying the fundamental forces that govern the interaction of the nanoparticles with other structures. The protein corona determines the in vivo organ distribution and the clearance of the particles from the circulation. It furthermore governs the interactions of particles with individual cells. [35, 38–41]. When nanoparticles get in touch with the cell membrane, receptor-ligand interactions as well as unspecific interactions occur. Ligands are thereby not necessarily of biological origin. They can also be chemical moieties, metallic sites, polymers or functionalities on the particle’s surface that promote binding affinity. Also nonspecific attractive forces which result from surface charges, hydrophobicity and surface roughness can promote cellular contacts [35]. All these effects influence the nanoparticle uptake into cells.

Due to their interactions with cells, nanoparticles are suspected to induce toxic effects in biological systems. These toxic effects may have several molecular reasons. First, nanoparticle-protein interaction might induce protein denaturation leading to functional and structural changes of the proteins [10, 35, 42]. These changes can result in the exposition of normally hidden epitopes and therefore to interferences in enzyme function and to disturbances in the metabolism [10, 43, 44]. But proteins might influence nanoparticles as well. Proteins as well as other organic substances attached to the surface of nanoparticles can increase their dissolution and thereby contribute to their degradation [35]. When nanoparticles dissolve within the cellular structure, the released salts can induce toxic effects as was shown for ZnO nanoparticles [45]. Another source for cytotoxicity is the possible catalytic activity of the nanoparticle surface which is especially important for photoactive particles like TiO₂. Surface groups or defects of the particles may act as active sites and react as electron donor or acceptor [10]. One prominent example is the formation of reactive oxygen species (ROS). The generation of low ROS amounts in the mitochondria is normal under natural conditions being easily neutralized by the cell via antioxidants like glutathion (GSH) and specialized enzymes [46]. An excess of ROS leads to the accumulation of oxidized glutathion (GSSG) and to oxidative stress. Cells react to this oxidative stress by activating protective or injurious responses [10, 46–48]. Furthermore, ROS radicals might interact with cellular components leading to a damage of cellular structures [7, 49]. Nanoparticles can also directly damage membranes or DNA or lead to the formation of foreign body granulomas, an accumulation of immune cells which occurs if the immune system reacts on foreign substances but is unable to eliminate them [10]. An overview of the described processes is shown in Figure 2.5.

2.2.3 The challenge of nanoparticle-risk assessment studies

As shown before, nanoparticles can interact with cellular structures in many different ways and are most likely interfering with cellular processes. Nevertheless, in contrast to risk assessment for new soluble chemicals, protocols and standardized procedures for nanoparticle cytotoxicity studies are not available [7, 19]. Moreover, no standard system for nanoparticle cytotoxicity investigations exists, enabling the comparison of different nanoparticle-systems and/or the results obtained in different labs [50, 51]. But why is the assessment of the cytotoxicity of nanoparticles so challenging and what are the differences to classical investigations carried out for new chemicals? The most

2 Nanoparticles

apparent difference is probably dosimetry. Concentrations of classical chemicals are well defined by specifying the amount of substance and the solvent volume used. But what are the right metrics to be used for nanoparticles? Should one compare experiments depending on the amount of substance, the number of nanoparticles or the surface area exposed to the test system [7, 40]? Depending on nanoparticle properties like size, aggregation or density, a given amount of substance results in e.g. different particle numbers when two particle species are compared [40, 50]. Furthermore, when cell culture experiments are considered, the nanoparticle concentration in proximity to the cell layer can significantly differ from the concentration added due to nanoparticle deposition effects [52, 53] whereas classical chemicals have a homogeneous concentration distribution in solution.

Other issues to be considered are the choice of the target system, the dose to be used and the exposition time in order to reproduce biologically relevant conditions. Each nanoparticle type is taken up differently by the human body and varies in its biokinetics. Thus the biokinetics of each nanoparticle species has to be assessed separately in order to unravel the most significant target organs or cells [40]. Furthermore the particle dose that is in contact with the target structure in “real life” has to be estimated whereby possible exposition hot spots like in the lung or macrophages have to be taken into account [7, 40]. In addition, it is necessary to differentiate between different types of exposure. What happens if the human body is exposed constantly to small amounts of nanoparticles or after a single exposure with a large particle number? And what are the resulting long term effects [7]? But beyond all these considerations, the most important factor complicating nanoparticle cytotoxicity assessment is probably the immense variety of nanomaterials that needs to be considered. Like every single “classical” chemical substance, each nanoparticle type needs to be investigated separately [19]. In contrast to “classical” chemicals, where the parameters “elemental composition” and “mass” are enough to describe their properties, new parameters are needed to classify nanoparticles thoroughly. Amongst these properties are their state of appearance (e.g. suspension, powder, film), their internal structure (amorphous, kristallin, core-shell particle), or their coating [50]. As even slight differences in the chemical and physical structure of the nanomaterial could lead to strong changes in biological activity, each of these parameters needs to be taken into account [18]. The combination of all these parameters results in an immense number of particles to be investigated [19]. What is more is that many properties of nanomaterials are still unknown and might even vary from batch to batch. For this reason, a huge number of control experiments is necessary for determining their exact properties [50].

In summary, a lot of open questions have to be addressed before a universal way for nanoparticle cytotoxicity assessment can be developed. Especially the correlation between dosimetry, nanoparticle deposition and cytotoxicity needs to be revealed before a generalized link between the influence of size, state of appearance, morphology or internal structure on cytotoxicity is possible.

2.2.4 State of the art cytotoxicity of amorphous silica nanoparticles

Amorphous silica species are a sub-type of silica substances that are produced by industry or found in nature. In contrast to cristaline silica like quartz or cristobalite which are known to be carcinogenic and which cause the lung disease silicosis after chronic inhalation, amorphous silicas were classified

as harmless in 1997, as there is inadequate evidence for carcinogenicity [54, 55]. What sounds like an all-clear for amorphous silicas needs to be considered with care as the amorphous silica species tested did not include nanoparticles. The reason for this becomes obvious when searching for the key word “silica nanoparticles” in online databases like “pubmed” which is provided by the National Center for Biotechnology Information and the U.S. National Library of Medicine [56]. In august 2011, 3579 entries could be found for this keyword, only 7 of them published before 1997 and 248 before 2005. When adding the keywords “toxicity” and “cytotoxicity”, 295 publications are found, the first published in 2000. Beyond these 295 publications, only 34 deal explicitly with amorphous silica nanoparticles. This shows that cytotoxicity of amorphous silica nanoparticles is a rather novel question. In the following section, recent findings concerning cytotoxicity of amorphous silica nanoparticles are summarized.

Several indications for cytotoxic effects induced by amorphous silica nanoparticles were found in vitro throughout the last years. Cytotoxicity of silica nanoparticles was observed to be dependent on nanoparticle size [33, 57–64], particle concentration, number or surface area [58, 59, 61, 65], surface properties and porosity [58, 60], incubation time [65], proteins in the cell medium [62, 63] and the cell type [66, 67] as well as the metabolic activity of the cells [67]. The experiments were carried out on a variety of cells including endothelial cells [58], human and mouse macrophages [60, 64, 66], liver cells [59, 65], keratinocytes [33, 61], epithelial cells [67], dendritic cells [66], several types of fibroblasts [62, 67], cancer cells [63], and Langerhans cells [57].

Metabolic activity of the cells

The most frequently analyzed parameter concerning nanoparticle toxicity in cell culture is the metabolic activity of the cells. Several publications showed that cellular metabolic activity decreases in response to nanoparticle impact in both a concentration and size dependent manner. Decreasing cellular activity of fibroblasts and epithelial cells could be correlated to an increase in nanoparticle mass concentration for particles with 21 and 80 nm for concentrations up to 66 $\mu\text{g}/\text{mL}$ [67]. The same influence was observed for 15, 30 and 365 nm sized nanoparticles on HaCaT cells (2.5 - 15 $\mu\text{g}/\text{mL}$) [61] and particles between 19 and 68 nm on HepG2 cells (12.5 - 2000 $\mu\text{g}/\text{mL}$). Nanoparticles with a diameter of 498 nm induced no or only a slight decrease in cellular viability in the same study [59]. In addition metabolic activity was found to increase with increasing nanoparticle diameter [59, 61].

All experiments mentioned above were carried out in presence of serum proteins. This is of great importance as serum proteins contained in the cell medium may alter the influence of nanoparticles onto cells. Drescher *et al.* found that the viability of fibroblasts after nanoparticle addition depends strongly on the concentration of fetal calf serum (FCS) in the medium: the more FCS was present (0-10%), the less toxic effect was observed for 38 nm particles [62]. Similar results are presented for 50 $\mu\text{g}/\text{mL}$ 70, 200 and 500 nm sized particles which did not diminish cellular viability in presence of proteins whereas viability was reduced by the 70 nm particles in absence of serum proteins. 200 and 500 nm sized particles had no effect on cellular viability [63]. A reason for the influence of serum proteins might be protein induced agglomeration which increases the effective particle size exposed to the cells [62]. Furthermore the protein shell could passivate the surface of the nanoparticles

2 Nanoparticles

[62, 63]. Nevertheless, studies carried out in absence of serum proteins with particles between 7 and 300 nm in macrophages [64] and particles between 13 and 335 nm particles in endothelial cells [58, 68] indicated a similar size and mass concentration dependency of cytotoxicity as observed in presence of proteins. The authors further calculated the nanoparticle surface area presented to the cells in both studies. They could show that the observed cytotoxicity is proportional to the surface area. Besides its dependency on size, concentration and incubation time, the nanoparticle induced decrease of metabolic activity was found to be dependent on the general metabolic activity of the cells. By comparing the cytotoxicity induced by 10, 21 and 80 nm silica particles on different types of fibroblasts and cancer derived epithelial cells a clear anticorrelation was observed between the cellular doubling times and the cytotoxic impact of the particles. This means that cancer cells are less sensitive to nanoparticle impact than healthy cells [67].

Permeability of the cell membrane - LDH assay

In many publications cellular viability is discussed together with the permeability of the cell membrane. The latter is correlated to the release of lactate dehydrogenase (LDH) from the cytoplasm into the medium and is a sign for membrane damage and hence cell death. Usually LDH release increase is observed simultaneously to a decrease in cell viability [58, 59, 63, 67]. It was also found to be correlated to an inhibition in cellular proliferation upon impact of 70 to 1000 nm nanoparticles upon Langerhans cells or keratinocytes [33, 57].

Cell death

Some groups directly investigate cell death in response to nanoparticles. In HepG2 cells apoptosis was observed after impact of 43 nm particles in a time and a concentration dependent manner (100 and 200 $\mu\text{g}/\text{mL}$) [65] and was found to be size dependent for 19 nm - 498 nm particles at a concentration of 100 $\mu\text{g}/\text{mL}$ [59]. Similar results were obtained with HaCaT cells. Applying the same dosages, smaller particles induced more apoptosis than bigger ones [61]. Hoet *et al.* and Bauer *et al.* proved that necrosis is induced in endothelial cells after the impact of 14 - 104 nm as well as 30 nm sized silica particles [22, 68]. Necrosis is rapid cell degradation accompanied by membrane damage whereas apoptosis, the slow-acting form of cell death, is an energy-dependent sequence of events [58]. In contrast to these findings, 100 $\mu\text{g}/\text{mL}$ 300 and 1000 nm amorphous silica nanoparticles induce apoptosis in macrophage-like cells whereas the smaller 30 - 70 nm sized nanoparticles don't [60].

Reactive oxygen species (ROS)

The reduction in cellular viability or the appearance of apoptotic effects are often assigned to the generation of reactive oxygen species (ROS). An extensive increase in ROS production can exceed the capacity of the antioxidant mechanisms what might be leading to injury in lipids, proteins or DNA [69]. Sun *et al.* found an increase in intracellular ROS level with increasing nanoparticle concentration (0 - 100 $\mu\text{g}/\text{mL}$) when applying 43 nm particles on HepG2 cells. Interestingly, a further increase in concentration to 200 $\mu\text{g}/\text{mL}$ lowered the ROS level. Nevertheless a rising apoptotic rate and change in membrane potential was observed for the whole concentration interval. Therefore they think that ROS production, in combination with other processes, might be the key factors for

cytotoxicity in this case [65]. Another study reported on a size dependent increase in ROS level which was observed when 100 µg/mL 19 to 498 nm sized amorphous silica particles were incubated on HepG2 cells. The authors claim that the size dependency might be influenced by the bigger surface area and surface reactivity of smaller compared to larger particles. However other processes should also influence cellular viability in this case as the ROS level is only slightly changed by the 498 nm particles whereas clear apoptotic effects were observed for this particle size [59].

Alteration in the gene expression level

Yang *et al.* found a nanoparticle dependent alteration in the expression level of oxidative stress associated proteins for 15 and 30 nm amorphous silica particles in HaCaT cells. In addition they found alterations in the gene expression level of cytoskeleton-associated proteins, molecular chaperones, energy metabolism-associated proteins and apoptosis as well as tumor-associated proteins. They think that this alteration in protein expression level may indicate that the investigated nanoparticles might promote tumorigenesis [61]. These findings are in agreement with other studies showing the alteration in expression of apoptosis related factors [65] and an increase in inflammatory protein secretion upon nanoparticle impact [64].

DNA damage, cellular morphology, cell cycle arrest, and hemolytic activity

In addition to the effects discussed before, nanoparticle impact was found to induce DNA damage [33, 59], cellular morphology changes, like the appearance of multinucleated cells or irregular shapes and cell cycle arrest [59, 61]. Furthermore hemolytic activity is described for silica nanoparticles in dependency on nanoparticle size, concentration and surface structure. Amorphous silica nanoparticles are reported to induce more membrane damage to red blood cells compared to mesoporous silica nanoparticles. This effect probably comes from the fewer silanol groups present on the surface of mesoporous in comparison amorphous silicas which can interact with the cells [70].

Procoagulatory response, cell migration and cell proliferation

A recent study on silica nanoparticle impact onto HUVEC cells showed that 310 nm sized SiO₂ nanoparticles induce procoagulatory response after 24 h of particle incubation. The procoagulatory response was monitored measuring the exocytosis of the von Willebrand factor, a protein associated with blood clotting, and the subsequent formation of ultralarge fibers. Furthermore, it was shown that the nanoparticles affect cell migration and proliferation after 16 h of incubation [68].

Localization of nanoparticles within the cells

In addition to the cytotoxic impact, the localization of nanoparticles within the cells was investigated by electron microscopy and fluorescence imaging. In absence of serum proteins, non-agglomerated 38 nm particles were found in endosomal and lysosomal structures inside 3T3 cells as well as in intracellular vesicles. No particles were located in the cytoplasm. In presence of media less particles seem to be taken up, as probably only big aggregates are in contact with the cells [62]. In another study cellular uptake of 70, 200 and 500 nm particles into HeLa cells was investigated. After 24h of exposure all particle types were found to accumulate mostly in vesicular structures. No particles could be found in mitochondria. The 70 nm were preferentially located in lysosomes compared to the bigger nanoparticle species. Furthermore no particles were present in the nucleus [63]. This is

2 Nanoparticles

in contrast to another study claiming that 70 nm silica nanoparticles enter the nucleus of HaCaT cells [33]. A study on 43 nm particles showed that these particles enter HepG2 cells via endocytosis as particles were found to be wrapped in the different stages of endocytic vesicles like endosomes and lysosomes. Additionally some of the particles were directly penetrating the cell membrane [65].

In conclusion, nanoparticle cytotoxicity seems to be dependent on nanoparticle size, incubation time, concentration and cell type in vitro. The nanoparticles influence the cellular viability, the membrane integrity and the ROS level of the cells. Furthermore they can damage DNA, change protein expression patterns and arrest the cell cycle. Bigger sized nanoparticles were only found within endosomal structures whereas small particles (43 and 70 nm) were localized within the cellular nucleus and were shown to directly penetrate the membrane.

2.3 Methods for nanoparticle characterization

Nanoparticles are characterized by their size, morphology and surface charge. In the following section, the techniques used to determine the size and morphology of the investigated nanoparticles are presented. Furthermore, the term zeta potential, a value used to specify the particle's surface charge, is explained.

2.3.1 Size and morphology

Each nanoparticle type behaves differently in biological media, depending on its size and morphology. Processes like particle diffusion and sedimentation are dependent on the nanoparticle size. In addition, a combination of nanoparticle size and morphology might influence the probability of nanoparticle's uptake and the uptake pathway into cells. Throughout this work size and morphology of the nanoparticles were determined by transmission electron microscopy or scanning electron microscopy. In addition, the hydrodynamic diameter of the nanoparticles was investigated by dynamic light scattering (DLS).

Transmission electron microscopy and scanning electron microscopy

Electron microscopy uses the interaction of electron beams with the sample to obtain highly resolved images. Due to the short wavelength of the electrons, electron microscopy can reach resolution down to the atomic level. For obtaining a transmission electron (TEM) image, an electron beam is generated by an electron gun and then guided onto the sample by magnetic lenses reaching the sample in a parallel mode. In the bright field mode the image contrast is formed by electrons absorbed or occluded by the sample. Thicker regions and regions with higher atomic numbers appear dark in the image whereas empty spots and thin sample regions are bright. In scanning electron microscopy (SEM) a focused electron beam is scanned across the sample. The signal of interest is detected and the image is formed spot by spot. The topography of the sample can be assessed by detecting the backscattered electrons or the secondary electrons released by the sample after impact

of the primary electron beam. The intensity of these electrons is depending on the atomic number of the atoms composing the investigated material. In secondary electron contrast mode resolutions down to few nanometers can be reached. Both TEM and SEM have to be operated in vacuum as the electrons would interact with air. Due to this restriction electron microscopy cannot be used to investigate living objects [71].

Dynamic light scattering

Dynamic light scattering (DLS) is a non-invasive technique used to characterize particles in suspension. During the measurement, a beam of monochromatic light crosses the sample and the intensity of light scattered by the particles is detected. The intensity of the scattered light is time dependent due to brownian motion of the particles. This time dependency is used to determine the translational diffusion coefficient D which is converted into the hydrodynamic diameter (R_H) using the Stokes-Einstein equation [72].

$$R_H = \frac{kT}{6\pi\eta D} \quad (2.3.1)$$

η represents the viscosity of the solvent, k is the Boltzmann constant and T the temperature of the medium [73]. It is important to note that by DLS, the hydrodynamic diameter of a particle is determined whereas TEM and SEM are used to measure the size of the particle without the solvation shell.

2.3.2 Zeta potential

The surface charge of particles mediates a variety of factors governing nanoparticle-cell interaction. Depending on their charge nanoparticles can attach to or are repelled by the negatively charged cellular surface. Furthermore the interaction of nanoparticles with different sets of proteins is also mediated by charge effects [74, 75]. The surface charge of particles is specified by their zeta potential. The latter is the electric potential of the solid-liquid interface between the particle surface and the surrounding fluid [76]. This solid-liquid interface is also called the slipping plane [77]. Ions around the particle form an electrical double layer (see Figure 2.6.) The inner part of this double layer is called the Stern layer, the outer part belongs to the diffuse layer. Ions within the Stern layer are firmly attached to the particles. Ions in the diffuse layer are more loosely attached. Within this outer region an additional boundary, the slipping plane, is defined. Ions between Stern layer and slipping plane move with the particle whereas ions on the other side of the slipping plane do not follow a particle's movement [78]. This definition of the slipping plane is widely accepted. Nevertheless it's exact position cannot be determined [77].

When an electric field E is applied across an electrolyte containing colloidal particles, the particles start moving towards the oppositely charged electrode. For uniform and weak electric fields, the linear relation between the steady state-electronic velocity of the particles v_e and the applied electric field can be used to calculate the electrophoretic mobility U_e of the particles [77].

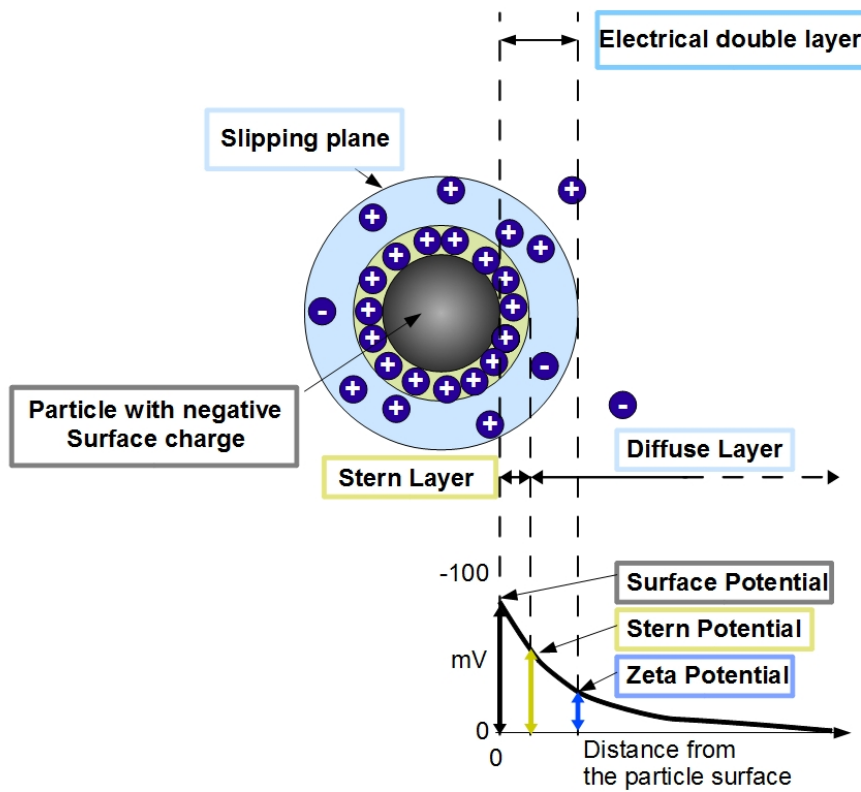


Figure 2.6: Scheme of the electrical double layer surrounding a nanoparticles in solution. The negatively charged particle is surrounded by firmly attached positively charged ions forming the Stern layer. The electric potential at the Stern layer is called Stern Potential. Ions outside this inner layer are more loosely attached and belong to the diffuse layer. Within this outer region an additional boundary, the slipping plane, is defined. Ions between Stern layer and slipping plane move with the particle whereas ions on the other side of the slipping plane do not follow a particle's movement. The electric potential at the slipping plane is called the zeta potential. This figure was adapted from [78].

2.3 Methods for nanoparticle characterization

$$v_e = U_e E \quad (2.3.2)$$

The zeta potential z can then be calculated applying the Henry equation [78].

$$U_e = \frac{2\epsilon z f(ka)}{3\eta} \quad (2.3.3)$$

The Henry's function $f(ka)$ is equal to 1.5 for zeta potential measurements done in aqueous solutions with moderate electrolyte concentrations. The electrophoretic mobility is dependent on the dielectric constant ϵ and the viscosity η of the medium as well as on the zeta potential [78]. The latter is dependent on the charge present on the surface of the particle, the pH of the system, the electrolyte concentration of the solution, the type of electrolyte and the type of solvent. It is obvious that the zeta potential is only well defined if all these parameters are well controlled and fixed [77].

3 Fluorescence techniques

Many techniques dealing with the analysis and investigation of single molecules or small functional unities are based on fluorescence. Fluorescence is the spontaneous emission of light by a molecule in an electronically excited state occurring to induce energetic relaxation. Usually, fluorescent marker molecules are used to label the structure of interest. The behavior of the markers allows to draw conclusions about the properties of the sample. Throughout this work we used several fluorescence based methods to characterize the nanoparticles and to investigate their interaction with cells on a single cell level. By fluorescence emission spectra and fluorescence anisotropy we differentiated between dye molecules bound to the particle's surface and dye molecules incorporated into the particle's structure. Furthermore we used widefield fluorescence microscopy and confocal fluorescence microscopy as well as confocal spinning disc microscopy to, e.g. estimate the flow velocities in a microfluidic system, to characterize the uptake pathways of nanoparticles into cells or to quantify the number of dye molecules bound to an individual nanoparticle. In the following sections the molecular excitation and relaxation processes leading to the emission of photons and thereby to fluorescence are described. Furthermore fluorescence quenching is defined and the used fluorescence microscopy techniques are presented. In the last part fluorescence anisotropy, a technique which can be used to probe the motility of the dye, is explained.

3.1 Molecular excitation and relaxation processes leading to fluorescence

Fluorescence can occur when a molecule undergoes a cycle of excitation and emission processes. The schematic representation of these processes is shown in the Jablonski diagram (see Figure 3.1). Before excitation, molecules are in their electronic ground state. In most cases, the electronic ground state is a singlet state, termed S_0 . When the molecule is excited, e.g. by a light beam, one of the electrons located in the highest occupied molecular orbital (HOMO) is promoted into an energetically higher unoccupied orbital, retaining the orientation of its spin. The molecule hereby reaches an excited electronic singlet state like S_1 or S_2 . In each electronic state molecular vibrations can be induced, leading to additional molecular energy levels which can be occupied by electrons. The energy difference between the electronic ground state and the excited states of the molecule determines which energies and thus which wavelengths are absorbed. The green arrows in Figure 3.1 show examples for possible electronic transitions from S_0 into excited vibrational states of S_1 , and a direct transition into S_2 . The probability of such a transition is equal to the square of its transition dipole moment. The latter represents the direction and magnitude of the charge distribution during

3 Fluorescence techniques

the transition. An optimal excitation of a transition is reached when the electronic field vector of the light and the transition dipole moment of the molecules are aligned parallel to each other [79, 80]. The absorption spectra of a molecule reflect its probability of photon absorption in dependency on the wavelength [79]. The excited molecule has several possibilities for a subsequent de-excitation back into its ground state. The relaxation can either occur radiationless or be accompanied by the emission of light [80]. In aqueous environment, the dominant relaxation process is vibrational relaxation. The molecule reaches its lowest vibrational state of its electronic state by transferring the energy stored in the vibrational levels to the surrounding solvent molecules within femto to picoseconds (see red arrow in Figure 3.1). Another possible way leading to de-excitation is internal conversion. Like the vibrational relaxation, the internal conversion is radiationless. It occurs if the energy difference between electronic states is very low and highly excited vibrational states of the lower excited state overlap with the energy levels of the higher electronic state. As indicated by the blue arrow in Figure 3.1, the molecule can then directly switch between the energy levels. By both vibrational relaxation and internal conversion, the molecule usually reaches the vibrational ground state of the first excited state S_1 [79]. In good fluorophores, the relaxation from the first excited state to the ground state is mediated by photon emission. This process is called fluorescence and occurs within nanoseconds. The molecule is transferred to one of the excited vibrational states of S_0 (see Figure 3.1, purple arrows), from where it is de-excited into the ground state via vibrational relaxation. As several excited vibrational states can be occupied after photon emission, fluorescence light of various wavelengths is emitted. As the energy level structure of the electronic ground state and the excited state is usually very similar, but energy is lost between excitation and emission due to relaxation of the molecule into the ground state of the excited electronic state, absorption and the emission spectra have mirror symmetry but are shifted in energy, the so called Stokes shift [80]. Similar to absorption processes, the probability of fluorescence emission is proportional to the square of the transition dipole moment. Furthermore, the emitted photons are preferentially polarized parallel to the transition dipole moment [79]. A parameter used to characterize the fluorescence efficiency of a molecule is the quantum yield. It is equal to the number of photons emitted as fluorescence divided by the total number of photons absorbed [79]. Good fluorophores have quantum yields around 0.9 [80].

Another process following the excitation of a molecule is intersystem crossing. It is the radiationless transition from the S_1 state into vibrational energy levels of the triplet state T_1 which can occur if the energy levels overlap (Figure 3.1, yellow arrow). During this transition one of the electrons has to change its spin. As the angular momentum of an isolated system must remain constant, this spin-flip is forbidden but may take place to some extent as few processes exist which can compensate the change in angular momentum. Intersystem crossing is mostly followed by vibrational relaxation whereby the molecule reaches the vibrational ground state of T_1 . De-excitation into S_0 can be either non-radiative or via emission of a photon. The latter is called phosphorescence (Figure 3.1, gray arrow). As the relaxation back into S_0 is accompanied by another forbidden spin flip, it often takes up to μs until this transition occurs. Due to the long lifetime of the triplet state, triplet state molecules are removed from the pool of excitable molecules. In addition they can easily undergo

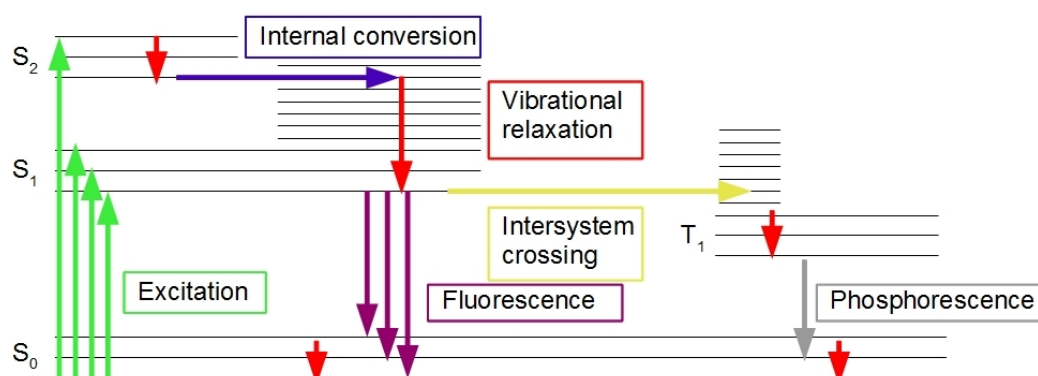


Figure 3.1: Jablonski diagram visualizing possible excitation and relaxation processes of a molecule. During absorption (green arrows), the molecule is transferred from the electronic ground state S_0 into excited electronic states (e.g. S_1 or S_2) and the corresponding excited vibrational levels. The molecule can go back into the vibrational ground state via vibrational relaxation (red arrow). Another possible way leading to radiationless de-excitation is internal conversion (blue arrow). From the vibrational ground state of the excited state, the system relaxes back into excited vibrational states of S_0 via photon emission (purple arrow). This process is called fluorescence. Afterwards vibrational relaxation occurs until the system is back in the fully de-excited state. From the S_1 state, the system can also undergo intersystem crossing (yellow arrow). This process is forbidden and therefore only occurs in the minority of cases. The molecule is transferred into the triplet state T_1 from where it may relax back into S_0 via phosphorescence (gray arrow). The Jablonski diagram was adapted from [80].

photochemical reactions that cause photobleaching or phototoxicity. For these reasons, the transition into the triplet state is not desired [79, 80].

3.2 Fluorescence quenching

The intensity decrease of fluorescence upon impact of an additional molecule is called quenching. Two main quenching types are differentiated depending on their mechanism. During collisional quenching, the excited-state of a fluorophor is deactivated upon collision between fluorophor and quencher which is mediated by diffusion. The fluorophor is returned to its ground state without emission of a photon or chemical alteration. In live-cell imaging it is used to distinguish whether a particle has been taken up into the cell or whether it is present in the extracellular space. For this, a membrane impermeable quencher that is added to a cell culture prevents the fluorescence of nanoparticles in the extracellular space whereas particles taken up by the cell remain bright. The second process is static quenching where the fluorophor and the quencher form a nonfluorescent complex. Furthermore quenching can also occur by attenuation of emitted light by the fluorophor itself or by an absorbing species. [81].

3.3 Fluorescence anisotropy

The term anisotropy expresses a directional dependence of a property or a process. Fluorescence anisotropy thereby describes the emission of fluorescent light with a preferred polarization. By measuring the fluorescence anisotropy of a sample, the rotational diffusion of an fluorescent object in the time gap between excitation and emission can be determined. When a randomly oriented sample is illuminated by linearly polarized light, a subpopulation of molecules is excited having their transition dipole moment aligned in the same or similar direction as the polarization of the light. If no rotational diffusion occurs and the transition dipole moment of fluorescence has a similar orientation as the transition dipole moment of the absorption, photons are preferentially emitted with similar polarization as the excitation light. The sample is anisotropic. The fluorescence of an isotropic sample is unpolarized, as the orientation of the fluorescence light is lost due to fast rotational diffusion of the excited molecules between excitation and emission. The orientation of the emitted light is detected by a polarization analyzer consisting of two polarization filters which are orthogonal to each other. The light intensity is measured in parallel (I_{\parallel}) or perpendicular (I_{\perp}) to the polarization of excitation. Imagine an experimental setup with the excitation source along the x- and the detector along the y-axis (see Figure 3.2). When the system is excited along the x-axis with z-polarized light (I_z), the emitted light will have x- (I_x), y- (I_y) and z- (I_z) polarized components when reaching the detector. The z component emitted by the fluorophor is equal to I_{\parallel} measured by the detector. The intensity of the second polarization which can pass the polarizer, I_{\perp} is equal to the light polarized along the x-axis I_x . Light polarized in y-direction (I_y) is not measured directly. However, as depolarization by rotational diffusion is a random process, I_y is equal to I_x , as both directions of depolarization have the same probability. The fluorescence anisotropy r_0 is expressed as the difference between light emitted in parallel and perpendicular direction compared to the excitation light, normalized by the total emitted fluorescence intensity.

$$r_0 = \frac{I_{\parallel} - I_{\perp}}{I_{\parallel} + 2I_{\perp}} = \frac{I_z - I_x}{I_x + I_y + I_z} \quad (3.3.1)$$

r_0 can reach a maximum value of 0.4 for samples with a random distribution of molecules with parallelly aligned excitation and transition dipole moments. This is not immediately apparent from Equation 3.3.1 and needs further considerations. If a sample is excited with e.g. z-polarized light, the probability for excitation P_{exc} is dependent on the angle Θ between the z-axis and the excitation transition dipole moment of the individual molecule.

$$P_{exc}(\Theta) \propto \cos^2(\Theta) \quad (3.3.2)$$

This means that maximum excitation is reached when the transition dipole moment is exactly parallel to the polarization vector of the light, hence when Θ is equal to 0° or 180° . Excitation vanishes for Θ values of 90° or 270° . In a randomly oriented sample, the dipoles are distributed homogeneously with respect to the exciting light. The population of molecules having a transition moment with an angle in the range between Θ and $\Theta + d\Theta$ is proportional to the surface area on

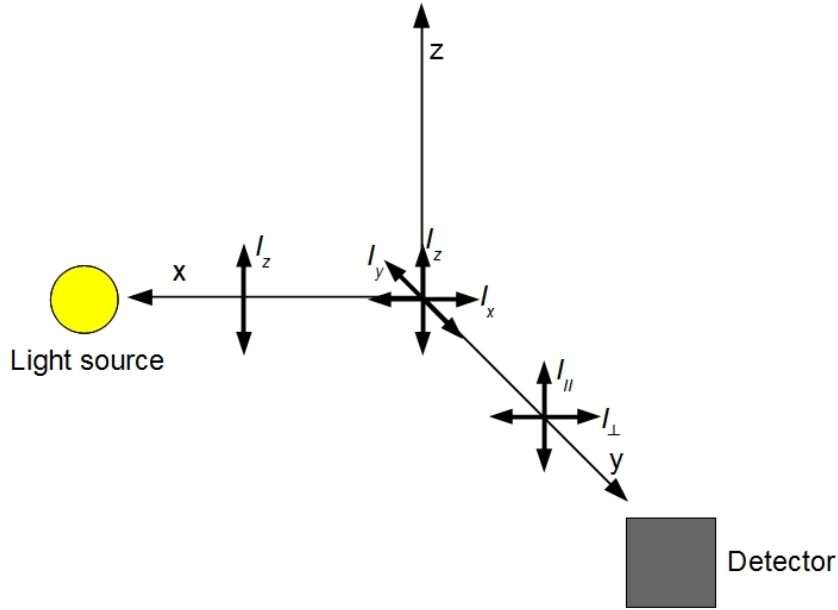


Figure 3.2: Schematic representation of a setup used to measure fluorescence anisotropy highlighting the relations between I_{\parallel} , I_{\perp} as well as I_x , I_y and I_z . The scheme is adapted from [79]

a sphere and therefore equal to $\sin\Theta d\Theta$. Hence, the fraction of molecules excited in a randomly oriented sample by linearly polarized light enclosing an angle Θ between their transition dipole moment and the polarization of the light can be calculated as following.

$$f(\Theta)d\Theta = \cos^2 \Theta \sin \Theta d\Theta \quad (3.3.3)$$

In the next step, the average emission anisotropy of molecules contained in a randomly oriented sample is calculated. The molecules have a parallelly aligned absorption and emission dipole. The intensities I_{\parallel} and I_{\perp} radiated from the sample are proportional to the square of the projection of the transition dipole moment vector onto the observation axis.

$$I_{\parallel}(\Theta) = \alpha \cos^2 \Theta \quad (3.3.4)$$

$$I_{\perp}(\Theta, \Phi) = \alpha \sin^2 \Theta \sin^2 \Phi \quad (3.3.5)$$

Θ represents the angle between transition dipole moment and the z-axis, Φ the angle which the transition dipole moment encloses with the yz plane, projected onto the xy plane (see Figure 3.3). As the excitation probability is only dependent on Θ , the angle between the transition dipole moment and the z-axis but independent on Φ , we can simplify Equation 3.3.5 by using the average value of $\sin^2 \Phi = \frac{1}{2}$. Using these relations, the fluorescence anisotropy depending on the angle Θ can be

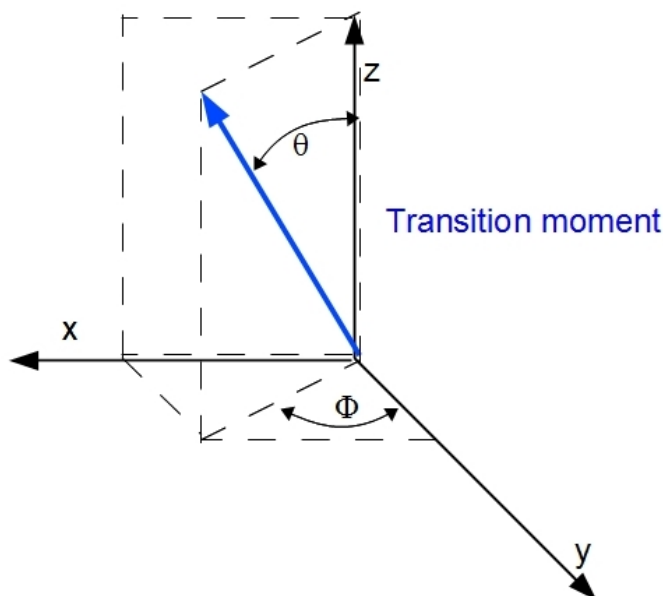


Figure 3.3: Scheme depicting the definitions of the angles Θ and Φ which are used to calculate the anisotropy of a molecule, depending on the orientation of its transition dipole moment. The scheme is adapted from [79]

rewritten as

$$r(\Theta) = \frac{I_{\parallel} - I_{\perp}}{I_{\parallel} + 2I_{\perp}} = \frac{3 \cos^2 \Theta - 1}{2} \quad (3.3.6)$$

The maximal anisotropy for a randomly distributed sample r_0 is now calculated by integrating the product of the excited fraction of molecules $f(\Theta)$ and its average anisotropy $r(\Theta)$, normalized by the total excited molecule fraction, over all angles Θ .

$$r_0 = \frac{\int_0^{\pi} f(\Theta) r(\Theta) d\Theta}{\int_0^{\pi} f(\Theta) d\Theta} = 0.4 \quad (3.3.7)$$

The maximum anisotropy value for a randomly oriented sample with parallel excitation and emission dipole moment without rotational diffusion is therefore equal to 0.4. If absorption and emission dipole are tilted towards each other by an angle α , the following variation of 3.3.6 is applies:

$$r_0 = 0.4 \left(\frac{3 \cos^2 \alpha - 1}{2} \right) \quad (3.3.8)$$

If rotational diffusion occurs, the anisotropy value of the molecules is reduced, depending on the

relative ratio between fluorescence lifetime τ and the rotational correlation time ρ . If the correlation time is much larger than the lifetime, the molecule does not move within excitation and emission and high anisotropy values are reached. The shorter the correlation time in comparison to the excited state lifetime, the more rotation takes place in the time span between excitation and emission reducing the fluorescence polarization and the anisotropy values [79, 81].

3.4 Fluorescence microscopes

Since the first glass magnifiers and microscopes have been developed more than 500 years ago, techniques for optical magnification have been improved and refined constantly [82]. Until today a broad variety of microscopes has been developed giving fascinating insight into tiny structures. Amongst them are fluorescence microscopes which are widely used for live-cell imaging applications. The most common techniques, laser illuminated widefield- and confocal fluorescence microscopy as well as spinning disk confocal microscopy are discussed below. A scheme of these microscopy techniques is presented in Figure 3.4.

3.4.1 Widefield microscopy

The left panel of Figure 3.4 shows the typical beam path of a widefield setup where a sample region of several micrometers in diameter is illuminated simultaneously. This is achieved by focusing the excitation laser beam into the back focal plane of the objective. The emitted fluorescence light is detected via the same objective in epi-fluorescence mode, separated by the excitation light via a dichroic beam splitter and focused onto a CCD camera. The image of a point-like light source shows a very distinct intensity distribution which is called the intensity point spread function, PSF. This PSF has an airy diffraction pattern. The pattern is formed, as the light waves that are emitted from a point source can not be focused into an infinitely small point by the objective. They rather converge together and interfere near the image plane. This interference results in a three-dimensional diffraction pattern. When an image is focused into the image plane of an optical microscope, every point of the image is represented by such a point spread function [82]. The maximal achievable resolution is defined by the Rayleigh criterium (see Equation 3.4.1). It states that two point emitters with equal intensity can be resolved, when the first intensity maximum of the first coincides with the first intensity minimum of the second point [83].

$$r_0 = \frac{0.61\lambda}{NA} \quad (3.4.1)$$

$$z_0 = \frac{2n\lambda}{(NA)^2} \quad (3.4.2)$$

The minimal resolvable distance between two point emitters in lateral r_0 and axial z_0 direction is dependent on the wavelength λ , the refraction index of the medium n and the numerical aperture of the objective NA [84]. The numerical aperture NA is a parameter defining the resolving power

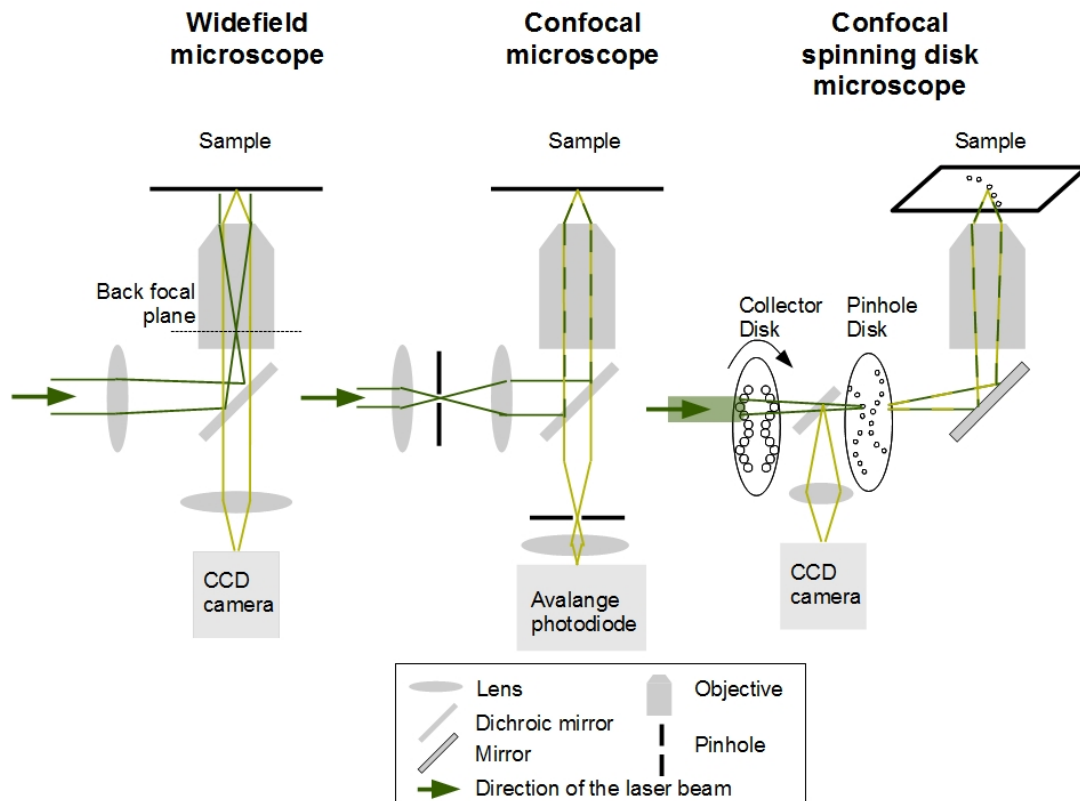


Figure 3.4: Schematic representation of the beam paths of widefield microscopy (left), confocal microscopy (middle) and spinning disk confocal microscopy (right). In the widefield microscopy setup, the exciting light is focused into the back focal plane of the objective. A sample area of several micrometers in diameter is illuminated simultaneously. During confocal imaging, the excitation beam is focused onto the sample, only illuminating a diffraction limited spot. Out of focus fluorescence is suppressed by focusing the laser light through a pinhole. To achieve a confocal image, the laser beam needs to be scanned over the sample. The resulting long acquisition time per image can be reduced applying spinning disk microscopy. Several spots of the sample are monitored simultaneously by focusing the laser light through an array of microlenses onto an array of pinholes. In all microscopy techniques, fluorescence is separated from the exciting light by a dichroic mirror before being captured by a detector.

and the light efficiency of the objective. It is calculated as the product of the index of refraction of the medium, and the sine of the semi aperture angle of focusing α [80, 83].

$$NA = n \sin \alpha \quad (3.4.3)$$

The axial resolution z_0 of the widefield microscopy given by the Rayleigh criterium should be used with care. As by widefield illumination a thick layer of the of the sample is illuminated, not only fluorescent dyes in the the focal plane but also above and below are excited. All these molecules will emit fluorescent light and contribute to the signal [85]. For this reason most of the 3D information of the image is lost and projected into the two dimensional widefield image.

During widefield microscopy, a lateral sample region with several micrometers in diameter is excited simultaneously and many individual chromophores can be observed at a time. This allows to record movies of the sample with time resolutions at near video rates [86]. The position of individual chromophores or objects within a widefield image can be determined by fitting a Gaussian function to the diffraction limited spots. It is thereby possible to gain time-resolved 2D trajectories of individual molecules. If 3D information is needed, confocal microscopy is the method of choice.

3.4.2 Confocal microscopy and confocal spinning disk microscopy

In confocal fluorescence microscopy 3D resolution is achieved by suppressing fluorescence coming from out of focus plane by confocal pinholes. Light from the focal area can pass through the pinhole whereas light from other planes is blocked [83]. In the middle panel of Figure 3.4 a scheme of a confocal setup is shown. The exciting laser beam is focused through a first pinhole onto the sample exciting only a diffraction limited spot. The emitted fluorescence light is collected by the objective and separated from the excitation light by a dichroic mirror. A second pinhole is placed “confocal” to the first one effectively suppressing out of focus fluorescence. The fluorescence light is collected by a point detector, e.g. an avalanche photodiode. The incorporation of the two pinholes into the beam path leads to an improvement of both the lateral and the axial resolution as the intensity of the side lobes and the width of the PSF are reduced. Thus the resolution is dependent on the pinhole size. For infinitely small pinholes, and the assumption of equal excitation and detection wavelengths ($\lambda_{exc} = \lambda_{em}$) the axial resolution r_0 and the lateral resolution z_0 are calculated as follows

$$r_0 = \frac{0.61 \lambda_{exc}}{\sqrt{2} NA} \quad (3.4.4)$$

$$z_0 = \frac{1}{\sqrt{2}} \frac{2n \lambda_{exc}}{NA^2} \quad (3.4.5)$$

where NA is the numerical aperture of the objective and n the refractive index of the medium [83].

By this configuration only one specific point of the sample is imaged at a time, allowing to count the number of photons emitted by this distinct region and to obtain time dependent fluorescence intensity trajectories with high temporal resolution. These intensity trajectories can be used to calculate the number of dye molecules present in this distinct region (see Chapter 5.7). To obtain

3 Fluorescence techniques

information about a larger sample area, a region needs to be scanned. This is either achieved by moving the sample or by moving the laser beam. The latter is quicker and therefore preferred [83]. Nevertheless, due to this scanning process, the time resolution of confocal microscopy is much lower than time resolution in widefield microscopy taking about 1 to 2 seconds per frame for one image plane [84] and several planes need to be monitored for a 3D representation of the sample. The scanning speed of a classical confocal microscope is usually too slow to allow live-cell imaging experiments as relevant events take place on shorter timescales than image acquisition. The scanning speed can be greatly enhanced by multifocal imaging. The excitation beam is thereby split into multiple foci and data of several confocal spots is collected simultaneously with a CCD camera. One commercially available technique is Nipkow disk confocal microscopy (see right panel in Figure 3.4). Here, the exciting laser light is simultaneously focused by several microlenses of the collector disk through the pinholes of the Nipkow disk onto the sample. The resulting spot pattern is scanned over the sample by spinning both disks. The fluorescence light is detected through the pinhole disk and separated from the excitation light by a dichroic mirror. Images are recorded by a CCD camera. With this setup, imaging speeds of 360 frames per second can be achieved allowing for live-cell imaging applications [83, 85].

3.4.3 Experimental setups

In the following, the configurations of the microscopes used for the experiments presented in this work are shown in detail.

Widefield microscopes

The experimental setup was based on a Nikon Eclipse TE 200 microscope. Two different lasers were used throughout the experiments providing 633 nm (HeNe, Coherent) and 488 nm (Coherent Sapphire) excitation light. The laser lines were spatially overlaid via dichroic mirrors, coupled into a multimode fiber (Amphenol, Wallingford, CT) to simplify the alignment and parallelized by a camera lens (AF Nikkor 50mm, $f = 45$ mm). The area of excitation was adapted to the area of detection by a rectangular pinhole. The laser lines were focused into the back focal plane of the 60x Nikon Plan APO water immersion objective by an additional lens ($f = 200$ mm). The emitted light was collected by the objective and separated from the excitation light by a trichroic mirror. The light was focused by a tube lens ($f = 160$ mm) and a telescope composed of two lenses with 150 mm and 135 mm focal length was used to reduce the image by a factor of 1.1. The fluorescence signal was split by a dichroic mirror (separation at 640 nm) in two separate paths. In both channels, the fluorescence signal was separated from background fluorescence by bandpass filters (575/80 nm for $\lambda < 640$ nm, 720/150 nm for $\lambda > 640$ nm). Both emission signals were then detected by one half of the EM-CCD camera chip (iXon DV884, Andor Technology, Belfast, UK). In addition, a second widefield setup based on a Nikon Eclipse Ti microscope was used. The main difference to the setup described above is that the fluorescence light is imaged by two separate EMCCD cameras depending on the wavelength. Therefore a bigger region of interest can be monitored at a time.

Confocal microscope

Confocal fluorescence microscopy and single photon counting was performed with a ZEISS LSM 410 microscope. The sample was excited with circular polarized 532 nm laser light (Solitron DLTS 200). High spatial resolution and detection efficiency were achieved with a high-numerical aperture oil-immersion objective (Zeiss 63x, oil). The fluorescence was separated from the excitation light by a LP 535 dichroic mirror and an emission filter (BP 675/250) and detected as a function of time by an avalanche photodiode (APD, EG&G SPCM-AY 141).

Confocal spinning disk microscope

The confocal spinning disk microscope (Andor technology) was based on a Nikon Eclipse TE 2000-E microscope in combination with a Yokogawa Spinning Disc unit (CSU 10). The samples were placed on a piezo-stage (NanoScanZ, Prior Scientific) enabling z-stacking. For illumination, a 488 nm (Coherent Sapphire diode laser) and a 635 nm (Coherent Cube diode laser) laser were used. The fluorescence light was separated from the excitation light by a quatochroic mirror (Di01-T405/488/568/647, Semrock) and a cleanup filter (NF01-405/488/561/635, Semrock). It was further guided into an OptoSplit II filter cube unit (Cairn Research LTd.) and split in two channels by a LP 593 dichroic mirror (AHF BS 593). Residual background fluorescence was removed by a 525/100 and a 730/140 filter respectively. Image sequences were captured with an electron multiplier charge coupled device camera (iXon DV887ECCS-BV, Andor Technology, Belfast, UK) whereby the two emission paths were focused on one half of the camera chip each. Several planes of the cells were imaged with a spacing of 166 nm and a detection time of 300 ms per plane. In addition a confocal spinning disk microscope (Zeiss) was used. It is similar to the one described above but was equipped with the spinning disc unit (CSU-X1), and two electron multiplier charge coupled device cameras (Evolve 512, Photometrics, USA), one for each emission path.

4 Cellular internalization pathways

The cell membrane is the gate between the intracellular and the extracellular space. All substances that are necessary for the cellular metabolism must be transported across this barrier. The cell membrane comprises specialized pumps and channels which enable the uptake of small molecules like amino acids, sugars or ions. Macromolecules, like proteins or nanoparticles are transported into the cell by endocytic pathways [87]. During endocytosis, membrane-bound vesicles are formed by invagination or by extrusion of the cell membrane enclosing the cargo. Then, these vesicles are released from the membrane into the cytoplasm and transported to their intracellular destination [88]. Endocytosis processes can be subdivided into two main classes, phagocytosis and pinocytosis. Phagocytosis is responsible for the uptake of large particles like e.g. bacteria and is typically restricted to specialized mammalian cells, whereas pinocytosis is used for the uptake of fluids as well as solutes and occurs in all cell types [87]. A schematic representation of all endocytosis processes can be found in Figure 4.1.

4.1 Phagocytosis

Phagocytosis is primarily used by specialized cells like macrophages, monocytes and neutrophils and serves to internalize large particles such as bacteria, dead cells or arterial deposits. During phagocytosis actin is assembled at the endocytosis site and cup-like membrane extrusions are formed that zipper up around the cargo to be engulfed [87, 88].

4.2 Pinocytosis

Extracellular fluids and solutes are taken up via different pinocytosis processes. Compounds can either be taken up directly from the fluid, attach to the membrane via unspecific binding (adsorptive pinocytosis) or be captured by specific high-affinity receptors (receptor-mediated endocytosis). Pinocytosis can be further subdivided into macropinocytosis, clathrin-mediated endocytosis, caveolae-mediated endocytosis and clathrin- and caveolae- independent endocytosis [87].

4.2.1 Macropinocytosis

Large amounts of fluids and growth factors are internalized via macropinocytosis [88]. After the activation of receptor tyrosin kinases like the epidermal growth factor receptor or the platelet derived growth factor receptor the actin polymerization at the inner side of the cell membrane increases resulting in an actin-mediated surface-ruffling. The newly formed actin branches grow and lead

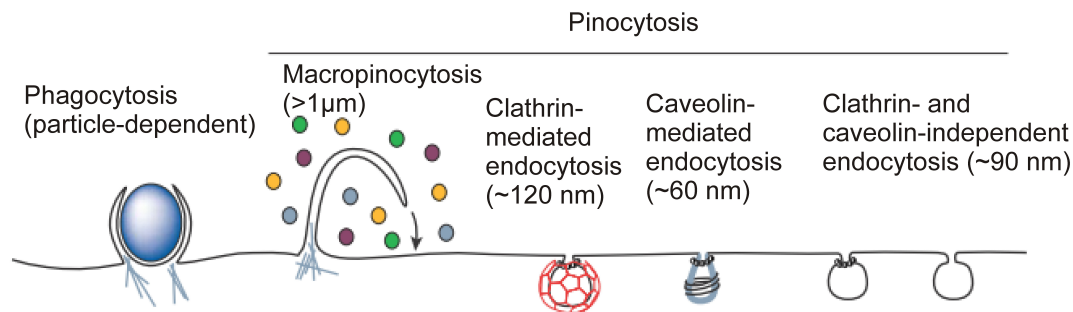


Figure 4.1: Cellular uptake pathways can be divided into two major groups: phagocytosis and pinocytosis. Whereas phagocytosis is restricted to specialized cells, pinocytosis can be found in most cell types. Pinocytosis includes several uptake processes: macropinocytosis, clathrin- and caveolin-mediated endocytosis as well as clathrin- and caveolin-independent processes. The image is taken from [87]

to plasma membrane extrusions. These extrusions collapse onto and fuse with the plasma membrane encapsulating a large volume of extracellular fluid. Further processing of the macropinosomes depends on the cell type. They are either transported towards the late endosomal or the lysosomal system, or they fuse back with the plasma membrane [89]. Several functions are fulfilled by macropinocytosis including the down regulation of activated signaling molecules or the antigen representation by the immune system [87, 89].

4.2.2 Clathrin-mediated endocytosis

Clathrin-mediated endocytosis occurs in all mammalian cells [87]. It is crucial for many cellular processes like intercellular communication or the regulation of signaling receptors [90, 91]. By controlling the levels of surface signaling receptors it modulates signal transduction and mediates the rapid clearance and downregulation of activated signaling receptors. Furthermore clathrin-mediated endocytosis is responsible for the continuous uptake of essential nutrients [87]. The formation of clathrin-coated endosomes starts with clathrin nucleation which is coordinated by adapter and accessory proteins. This nucleation takes place at specialized internalization sites of the plasma membrane. The clathrin polymerizes into curved lattices and thereby stabilizes the deformation of the attached membrane. The membrane scission protein dynamin forms a helical polymer around the neck of the vesicle and mediates its release from the plasma membrane. The clathrin basket detaches from the free vesicle and its components are recycled [92].

4.2.3 Caveolin-mediated endocytosis

Caveolae are flask-shaped plasma membrane invaginations with sizes between 50-100 nm [87, 93, 94] which form relatively immobile functional units at the cell surface [93]. Shape and structure of caveosomes are induced by the dimeric protein caveolin which forms a caveolin coat on the surface

of the membrane invaginations. It is embedded into the inner leaflet of the plasma membrane [87, 92]. During caveolin-mediated endocytosis, caveolae bud from the cell membrane. After their release, they can fuse with the caveosome or with the early endosome and the caveolar unit can be recycled back to the plasma membrane [93]. Caveolae are very common in specific cell types like smooth muscle cells, fibroblasts, endothelial cells and adipocytes [93, 95]. Depending on the cell type, caveolin-mediated endocytosis is a highly regulated event and occurs only after a specific stimulus [96]. The transported cargo is probably also cell type dependent and includes lipids, proteins and pathogens [88]. In addition to endocytosis, caveolae can play a role in transcytosis and cellular signaling where they act as signaling platforms [93, 97, 98].

4.2.4 Clathrin- and caveolin-independent processes

Clathrin- and caveolin independent processes include a variety of endocytic mechanisms which are based on several different substitutes [92]. A detailed description of all these processes would exceed the scope of this work. For details about these endocytic pathways please refer to corresponding reviews [88, 92, 94, 99].

4.3 The role of the actin and tubulin networks

The role of actin filaments in endocytic pathway of mammals is still discussed controversially. Despite the fact that several studies investigated the role of actin in endocytosis, it's function is not revealed yet. There are several different ways how actin might influence endocytic processes: spatial organization of the endocytic machinery, deformation and invagination of plasma membrane, dissolution of cortical actin barrier, force generation during or after fission reaction, vesicle movement into the cytoplasm or spatial organization e.g. marking of endocytosis hot spots [100]. Actin seems to play a crucial role in clathrin mediated and caveolin dependent processes [92]. It was shown that actin is recruited to clathrin-coated structure formation spots in 3T3 cells and is released as soon as the clathrin coated structures move into the cytosol [101]. Furthermore actin polymerizes on at least a subset of clathrin-coated pits assembled at the plasma membrane in cultured fibroblasts [102]. Nevertheless, clathrin coated vesicle formation was also found to be independent on actin in mammalian cells [103]. Actin seems to be involved in phagocytosis, macropinocytosis [88, 92, 94] as well as in several other clathrin and caveolin independent processes [88, 92, 94, 104, 105]. In addition it is possible that actin forms endocytic hot spots since it might serve as anchor for scaffold assembly. During the further progress of the endocytosis event it might propel nascent endocytic vesicles through the dense cytoskeletal apparatus via actin-comet tails [87].

Receptor mediated endocytosis is usually unaffected by microtubule depolymerization. Therefore microtubule seem not to be necessary for in cargo uptake [106]. It is rather involved in the subsequent vesicle transport. Long distance transport of cargo usually occurs in a directed way along microtubule tracks and is mediated by motor proteins [99, 104, 107, 108]. However, older publications indicate that microtubule might sometimes play a role in fluid-phase uptake which is slowed down after microtubule depolymerization [109–111].

5 Synthesis and characterization of SiO₂ nanoparticles

For nanoparticle risk assessment studies via live-cell imaging, the properties of the used nanoparticles are very critical. The nanoparticles should be as similar as possible to commercially applied species but should be detectable via fluorescence microscopy methods. It is of major importance, that the dye used for labeling the particles does not interact with the cells or dissolve in the cellular environment as this could lead to an artificial cytotoxic effect. In principle, it is possible to label particles either at their surface or in their core. Surface labeling has the advantage, that the dye is accessible by the solvent enabling e.g. quenching experiments, but the dye is also accessible for the cell and might interact with cellular structures. If the particle has a fluorescent core and an unlabeled shell, this interaction is prevented.

We chose silica nanoparticles, as they are commonly applied in industry and the basic synthesis procedures are well known. The particles were surface- or core-labeled with the dye perylene. All particles within this work, were synthesized and optimized by Dr. R. Herrmann (AK Prof. Reller, University of Augsburg), if not stated differently. Characterization of the particles was done in Munich and Augsburg in a close cooperation and with constant feedback to improve particle synthesis. In the following section, which is based on and adopted from the publication "Perylene-labeled Silica Nanoparticles: Synthesis and Characterization of Three Novel Silica Nanoparticle Species for Live-Cell Imaging" published in *Small* [4], the synthesis and characterization of these systems is described.

5.1 Synthesis of perylene labeled Silica nanoparticles

We chose two perylene-based fluorescent dyes (see Figure 5.1) to label the silica particles as perylene is known for its good photophysical properties, high photochemical stability and outstanding fluorescence quantum yield [112, 113]. The high photostability of perylene is very useful as photobleaching limits the observation time in microscopy [114, 115]. The monofunctional perylene derivative (MPD) (Figure 5.1, top) was prepared from a known precursor [116–118] by reaction with aminopropyltriethoxysilane, while the bifunctionalized perylene derivative (BPD) (Figure 5.1, bottom) is a known perylene species [119–121].

For the preparation of MPD labeled SiO₂ nanoparticles (MPD-SiO₂) and BPD labeled nanoparticles (BPD-SiO₂) we used a modification of the well-established Stöber method [122]. This method is based on the slow hydrolysis of ethoxysilane groups of the silica precursor tetraethoxysilane (TEOS)

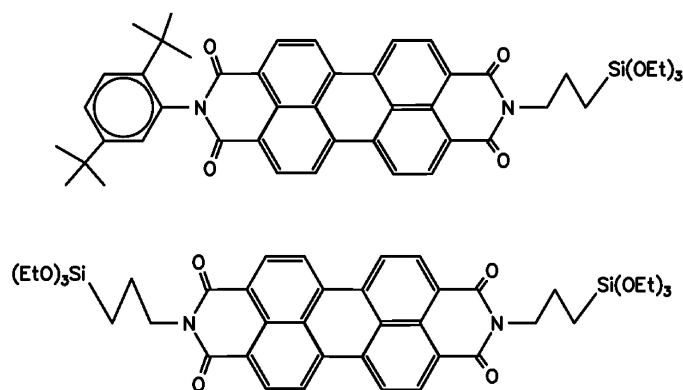


Figure 5.1: Monofunctionalized perylene derivative, MPD (top) and bifunctionalized perylene derivative, BPD (bottom) which were used for silica-nanoparticle labeling.

in presence of ethanol. During this process covalent Si-O-Si bonds are formed between the precursor molecules. This interconnection of the precursor molecules finally leads to the formation of silica nanoparticles. As MPD provides one and BPD two propyltriethoxysilane linkers, they can be attached covalently to the silica network during Stöber synthesis. The dye is directly added at the beginning of the reaction. Since its reactivity towards hydrolysis is considerably lower than that of TEOS the dye molecules are preferentially attached to the surface of the already formed nanoparticles. When MPD is used, isolated silica nanoparticles which are morphologically similar to unlabeled silica nanoparticles are obtained, while BPD leads to a network of connected silica nanoparticles when employed in higher concentrations as can be seen in TEM images (Figure 5.2). For further details about the synthesis procedure please see the corresponding publication [4].

A higher amount of reactive dye in the synthesis generally leads to more dye molecules per nanoparticle. The quantification of the number of dye molecules per nanoparticles is a challenging task and will be discussed in Section 5.7. By changing the amount of ammonia and water, the size of the particles can be influenced. The final particle sizes range from 15 to 500 nm.

In addition to MPD-SiO₂ and BPD-SiO₂, silica-nanoparticles with a fluorescent silica core and a non fluorescent silica shell (core-shell nanoparticles) were prepared. The fluorescent silica core is formed by incorporation of BPD into the silica network via cocondensation of BPD, diethoxydimethylsilane and trimethoxymethylsilane in a micelle [123–127]. A thin silica shell is subsequently added by introducing TEOS into the micelles in order to prevent aggregation. The resulting fluorescent nanoparticles are coated with a thicker silica shell, again using a modified Stöber method. The nanoparticles have an average size of 30-100 nm, where 10-30 nm account for the dye-containing silica core.

5.1 Synthesis of perylene labeled Silica nanoparticles

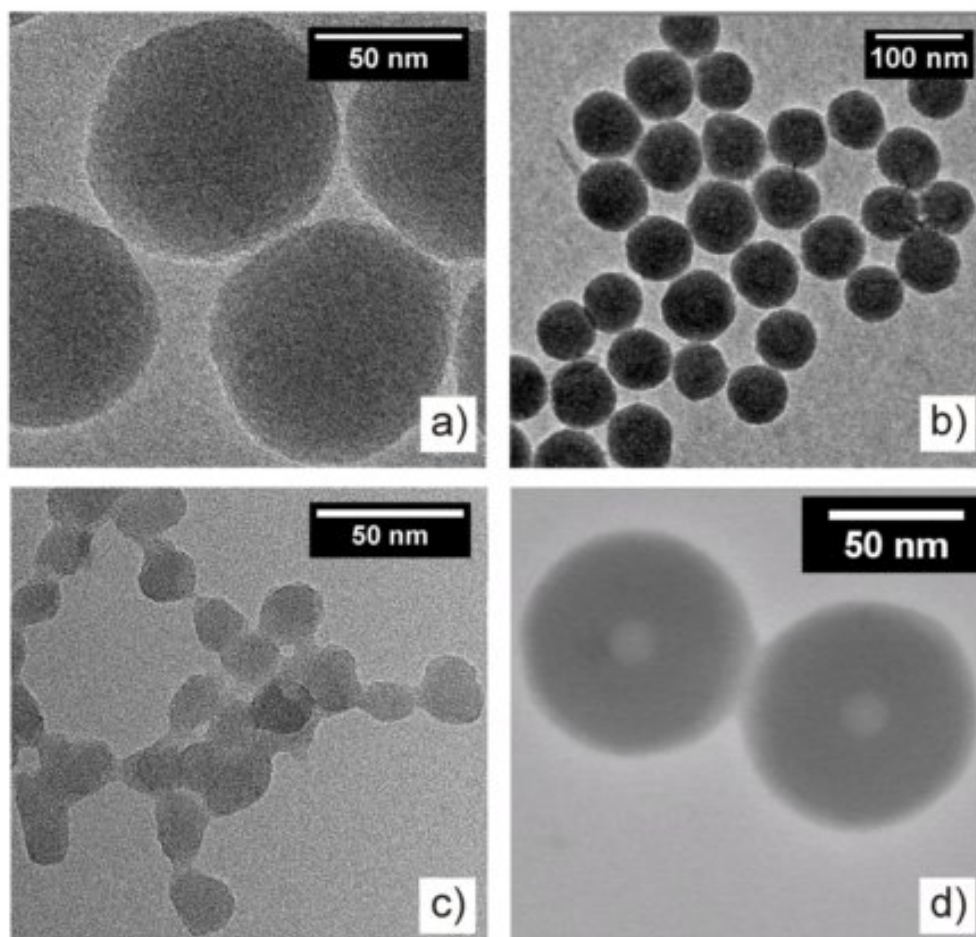


Figure 5.2: TEM images of different SiO₂-nanoparticle species. The addition of the monofunctionalized dye MPD during Stöber synthesis leads to a) nicely shaped, homogeneous spheres (MPD-SiO₂), which are comparable to b) unlabeled SiO₂ nanoparticles, whereas the addition of the bifunctionalized derivative BPD results in the formation of c) a nanoparticle network (BPD-SiO₂). d) Nanoparticles with perylene-containing core and silica shell (core-shell nanoparticles) have been synthesized via micelles. Please note the different scale bars.

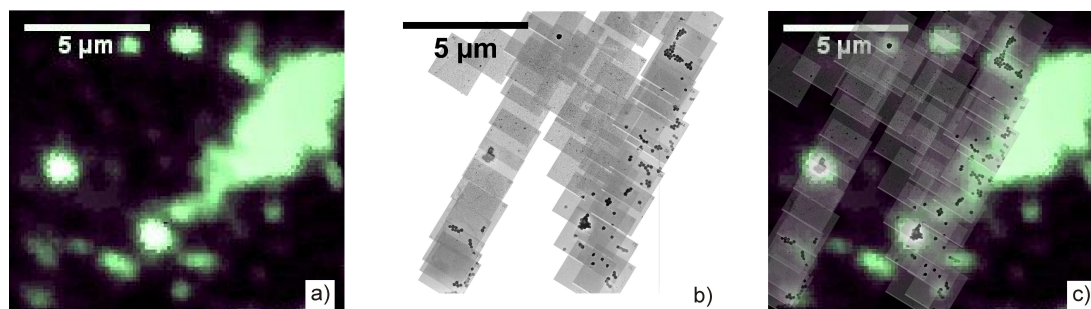


Figure 5.3: a) Background-corrected widefield fluorescence image and b) TEM images of the same sample region of MPD-SiO₂ nanoparticles, which are dispersed on a Si₃N₄ membrane. c) Overlay of the widefield fluorescence image and the TEM images. The correlation between nanoparticles and fluorescence is clearly visible and proves that the dye has attached to the nanoparticles.

5.2 Transmission electron microscopy analysis

The size and morphology of different types of silica nanoparticles was determined by transmission electron microscopy (TEM). TEM images were obtained by a JEM 2011 (JEOL, Tokyo, Japan) and a Titan (FEI, Eindhoven, Netherlands) transmission electron microscope respectively. The nanoparticle dispersion was diluted with EtOH or MeOH and applied onto a carbon coated copper grid (Plano, Formvar/coal-film on 200 mesh-net). Nanoparticle sizes were determined from TEM pictures by the ImageJ software (<http://rsb.info.nih.gov/ij/>). Figure 5.2 a shows MPD-SiO₂ nanoparticles with an average diameter of 80 nm. Typically, MPD-SiO₂ nanoparticles are homogeneous spheres with a narrow size distribution. They do not show aggregation. The morphology of the MPD-silica nanoparticles is similar to the morphology of unlabeled SiO₂ nanoparticles (Figure 5.2 b). The average diameter of the depicted, unlabeled nanoparticles is 70 nm. In the case of the BPD-SiO₂ nanoparticles, the presence of the bifunctionalized dye has a strong influence on the morphology of the nanoparticles. The corresponding TEM images (e.g. Figure 5.2 c) reveal that the nanoparticles are linked by necks. This interconnection, caused by the bifunctionalized dye, leads to the formation of a nanoparticle network. The nanoparticles within this structure have an average diameter of 18 nm and a slightly elongated shape. Figure 5.2 d) shows a TEM image of the core-shell nanoparticles. The core of the nanoparticles contains carbon atoms which have a lower atomic number than the silicon atoms of the shell. Therefore the core appears brighter than the shell and both structures are clearly distinguishable.

5.3 Overlay of TEM and fluorescence widefield images

After examining that the labeling with MPD has no influence on the morphology of the MPD-SiO₂ nanoparticles compared to the unlabeled nanoparticles the question still remained whether MPD has attached to the silica nanoparticles or if a separate fluorescent species consisting of pure perylene agglomerates has formed during synthesis. If the perylene molecules had attached to the nanopar-

ticles we expect a spatial correlation between the nanoparticles and the fluorescence signal. This correlation is shown by superimposing TEM images and widefield fluorescence images of the same region of a dried MPD-SiO₂ sample (Figure 5.3).

To prepare the sample, the MPD-SiO₂ nanoparticles were dispersed in methanol. Fluorescent polymer beads (175 ± 5 nm, Invitrogen; Karlsruhe, Germany) were added as spatial markers as they are visible both in widefield and TEM microscopy and therefore enable the recognition of the same sample region by both techniques. The suspension was transferred onto an optical transparent 25 nm thick Si₃N₄ membrane (Plano) which is suitable as sample carrier for widefield fluorescence imaging and TEM imaging. After air drying, the membrane was mounted onto the widefield fluorescence microscope. Fluorescence images of the perylene species and the fluorescent polymer beads were taken by alternated excitation of the sample with 633 nm and 488 nm laser light respectively. The fluorescence was collected via a 60x Nikon Plan APO water immersion objective in epifluorescence mode. The consecutive illumination together with separation of fluorescence emission below and above 645 nm in separate detection channels allowed distinguishing the fluorescence signal of the MPD-SiO₂ nanoparticles and the fluorescent polymer beads. The images were captured with an electron multiplier charge coupled device camera (iXon DV884, Andor Technology, Belfast, UK). After fluorescence imaging, the membrane was air-dried and transferred to the TEM (JEM 2011). The region examined by fluorescence microscopy was localized via the polymer beads. As the resolution of TEM images is approximately four orders of magnitude better than the resolution of fluorescence widefield images, a region of interest within the whole fluorescence image was chosen (Figure 5.3 a) and multiple, partly overlapping TEM images were acquired within this region. The single TEM images were combined and a map of the region was generated (Figure 5.3 b) utilizing the CorelDraw software (Corel Cooperation). The superposition of the fluorescence images and the TEM map reveals the correlation between nanoparticles and fluorescent dye (Figure 5.3 c). Regions with nanoparticles clearly show fluorescence signals. The fluorescence intensity directly correlates with the amount of nanoparticles visible, whereas regions without nanoparticles show no fluorescence. Regions with very high fluorescence intensities were not mapped by TEM due to the high number of nanoparticles in these regions.

These measurements show that the MPD has attached to or incorporated into the silica nanoparticles.

5.4 Fluorescence emission spectra

Information about the fluorescence characteristics of the silica nanoparticles and the free dyes was obtained by looking at their fluorescence emission spectra. As shown in Figure 5.4, the emission spectra of the free dyes and the nanoparticles have the same characteristic shape whereas the fluorescence maxima are dependent on the solvent and/or the nanoparticle type. The solvents were chosen according to solubility. The reactive perylene dyes MPD and BPD are soluble in ethanol and methanol but not in pure water. Therefore the spectra of MPD and BPD were measured in methanol and a mixture of methanol:water = 2:1. As illustrated in Figure 5.4 a) (MPD) and 5.4 b)

5 Synthesis and characterization of SiO₂ nanoparticles

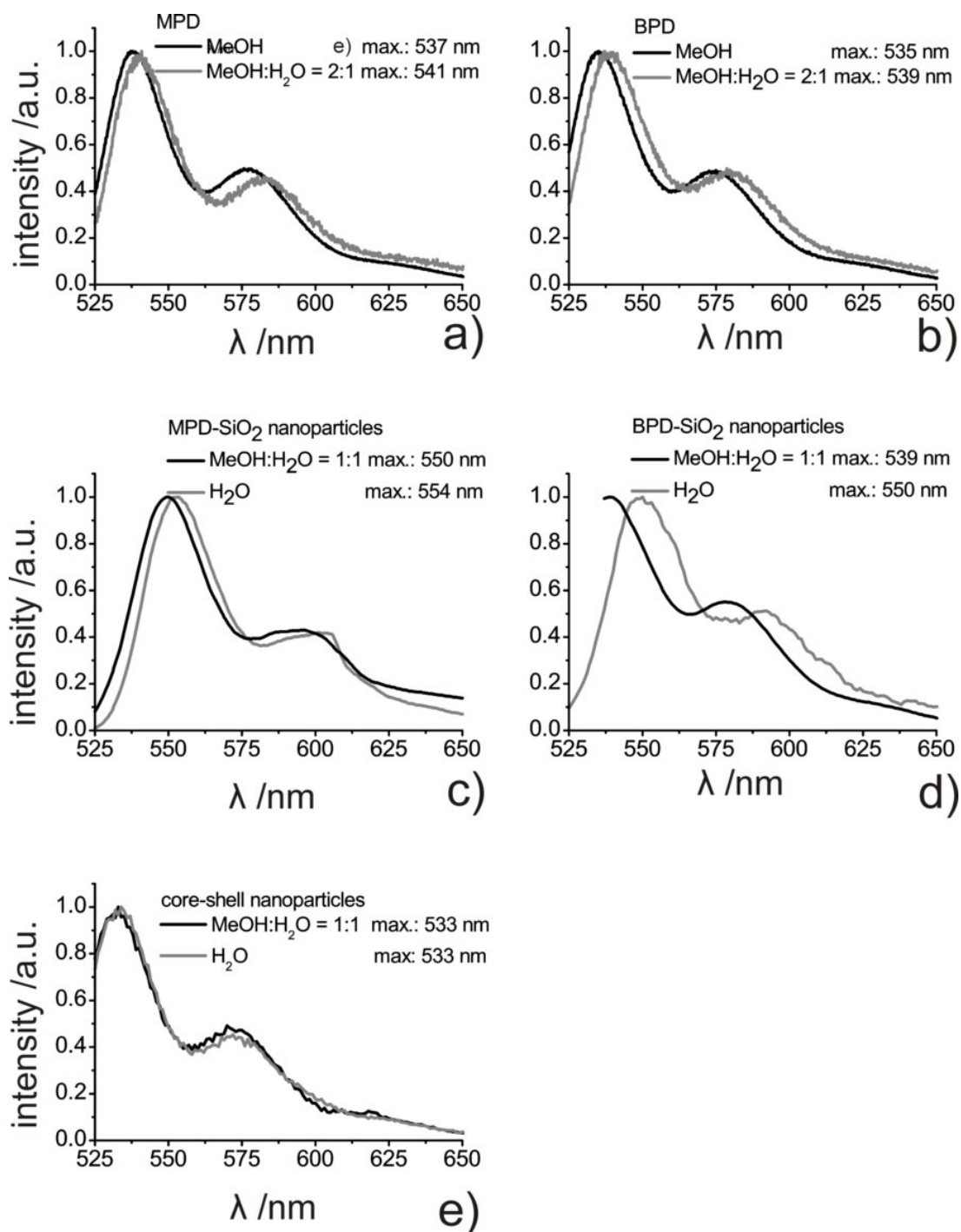


Figure 5.4: Normalized fluorescence spectra of the functionalized dyes a) MPD and b) BPD and of the synthesized nanoparticles c) MPD-SiO₂ and d) BPD-SiO₂, as well as e) core-shell nanoparticles, resulting from excitation with 488 nm. The spectra were measured in water, methanol, or mixtures of both, respectively.

(BPD) the fluorescence maximum responds to solvent polarity. With increasing solvent polarity from methanol to methanol:water = 2:1 the fluorescence maxima shift from 537 nm to 541 nm (MPD) and from 535 nm to 539 nm (BPD) respectively. This solvent polarity dependent shift to higher wavelengths is caused by the higher stabilization of the S1 excited state compared to the S0 ground state in polar solvents. It shows that perylene has a stronger dipolar moment in the excited state than in the ground state, resulting in the decrease in energy of S1.

Unlike the free dyes, the labeled nanoparticles can be dispersed in pure water leading to a fluorescent suspension. This is another proof that the dye molecules have attached to the nanoparticles. The solubility of nanoparticles in water or aqueous solutions like cell media is an important requirement for live-cell imaging as organic solvents and alcohol are toxic for cells. The fluorescence spectra of MPD-SiO₂ and BPD-SiO₂ were measured in methanol:water = 1:1 and water. The attachment of MPD or BPD to the nanoparticles does not change the shape of the fluorescence emission bands of the dyes (Figures 5.4 c and 5.4 d). Similar to the free dye in solution, the increase of solvent polarity leads to a fluorescence maximum shift to longer wavelengths. MPD-SiO₂ shifts from 550 nm to 554 nm and BPD-SiO₂ from 539 nm to 550 nm. This strongly indicates that the dye molecules of MPD-/BPD-SiO₂ are in contact with the solvent and therefore mainly located at the surface of the particles.

The core-shell nanoparticles behave differently. Compared to all spectra shown above, the fluorescence emission spectra of perylene-core nanoparticles is shifted approx. 20 nm to shorter wavelengths in water and methanol:water = 1:1. Note that no solvent dependent shift is present in the spectra of the core-shell nanoparticles (Figure 5.4 e). This leads to the conclusion that the dyes are located inside the core of the nanoparticle and therefore shielded from the solvent by the silica shell. Under these conditions the local environment of the perylene molecules consists mainly of silica and is therefore different from the aqueous environment of MPD-/BPD-SiO₂. This results in the 20 nm hypsochromic shift of the fluorescence maxima described above.

5.5 Fluorescence anisotropy

To confirm the localization of the dye inside or on the surface of the nanoparticle, we studied the ability of the dye to rotate in solution. Dye molecules that are incorporated into the structure of the nanoparticle are expected to be less flexible than dye molecules that are attached to the surface of the nanoparticle via a linker. The rotation of dye molecules is linked to an angular displacement of their absorption and emission dipole moments which lie along specific directions within their structure. This leads to a directional dependence of the polarization of the fluorescence, the fluorescence anisotropy. To probe the fluorescence anisotropy, the sample is excited with linearly polarized light. The fraction of molecules within the sample which happen to have their transition dipole moment aligned in parallel to the electric field vector of the light is excited preferentially resulting in a partially oriented excited state population. During the timeframe between excitation and subsequent emission of light, the dye molecules can rotate and the excited state population therefore partially loses its parallel alignment. The intensity of the emitted light is measured in

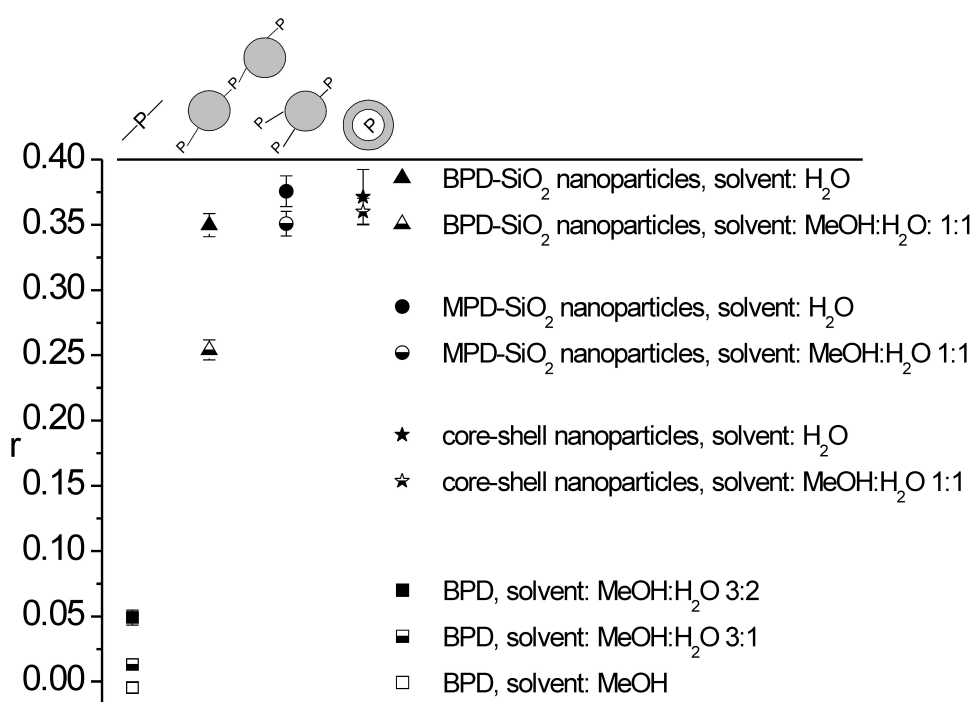


Figure 5.5: Fluorescence anisotropy data of BPD, as an example for a free dye, and of the various labeled nanoparticles depending on solvent polarity. The anisotropy values of the unbound perylene dye BPD (squares), BPD-SiO₂ (triangles), MPD-SiO₂ (circles), and core-shell nanoparticles (stars) in different solvents are shown (see legend).

parallel and in perpendicular orientation with respect to the polarization of the excitation light. The normalized difference between these intensities is called the anisotropy r (see equation 3.3.1) and mirrors the flexibility of the dye. For details please see Section 3.3.

The lowest anisotropy to be expected of the dyes was estimated by measuring the anisotropy of free BPD as an example for free perylene. According to solubility we determined the anisotropy in varying methanol:water mixtures with increasing polarity; ranging from pure methanol to methanol:water = 3:2. The resulting anisotropy values of BPD are below 0.05 (Figure 5.5, squares) in all applied solvents. These values are typical for the free motion of dye molecules in solution. Nevertheless the anisotropy of BPD fluorescence increases with increasing solvent polarity. The latter is accompanied by an increase in solvent viscosity, explaining the gradually diminished mobility of BPD.

The anisotropy values of BPD-SiO₂ nanoparticles (Figure 5.5, triangles), MPD-SiO₂ nanoparticles (Figure 5.5, circles) and the core-shell nanoparticles (Figure 5.5, stars) were determined in water and methanol:water = 1:1. All nanoparticles show anisotropy values above 0.36 when dissolved in water (filled symbols). This indicates that the dye molecules are rather immobile. As perylene is insoluble in water we think that the dye is sticking tightly to the surface of the nanoparticles leading to a comparably slow movement.

The anisotropy values change drastically when the nanoparticles are dissolved in a 1:1 mixture of methanol and water. The anisotropy of BPD-SiO₂ nanoparticle fluorescence decreases strongly to a value of 0.25 (Figure 5.5, half filled triangle) in response to the solvent polarity variation and the thereby increased solubility of perylene. We think this strong drop of anisotropy can only be explained if BPD is mainly located on the surface on the nanoparticles and has eventually formed dye chains by condensation of several BPD molecules. The movement of these chains is less restricted by the attachment to the surface of the nanoparticle than are single dye molecules. Thus the fluorescence anisotropy of the BPD-SiO₂ nanoparticles responds strongly to the improved perylene solubility.

In the case of MPD-SiO₂ nanoparticles (Figure 5.5, circles), the anisotropy values are less affected by the water to methanol:water = 1:1 solvent change than BPD-SiO₂. As MPD has only one reactive site the formation of dye chains is impossible. Therefore all MPD molecules are attached to the nanoparticles via a very short linker which inhibits strong movements of the dye molecules. The decrease of the fluorescence anisotropy is not very pronounced but it is still twice as much as the corresponding fluorescence anisotropy decrease of the core-shell nanoparticles (Figure 5.5, stars). Therefore we think that the MPD molecules are mainly located on the surface of the MPD-SiO₂ nanoparticles.

Concerning the core-shell nanoparticles (Figure 5.5, stars), the influence of the solvent change from water to methanol:water = 1:1 is even less than for MPD-SiO₂ nanoparticles. This supports the thesis that the dye molecules are located inside the nanoparticle.

5.6 Cellular uptake

To prove that the nanoparticles can be localized inside cells we incubated HeLa cells with 310 nm sized MPD-SiO₂ nanoparticles and visualized the nanoparticle uptake by confocal microscopy.

For these experiments, HeLa cells were grown in Dulbecco's modified Eagle's medium (DMEM; Gibco, Karlsruhe, Germany) supplemented with 10% fetal calf serum (FCS) at 37 °C in 5% CO₂ humidified atmosphere. The cells were seeded 48 or 24 h before imaging on collagen A or polylysine L-coated Lab Tek-chambered cover glass (Nunc, Rochester, NY, USA) in a density of $1.0 \cdot 10^4$ or $2.0 \cdot 10^4$ cells/well respectively. Before the imaging, the cells were transferred to CO₂-independent medium (Invitrogen; Karlsruhe, Germany) with 10% FCS. The cells were incubated with 108 µg/mL nanoparticles for 4.5 h. Afterwards, the membrane was stained with CellMaskTM Deep Red (Invitrogen; Karlsruhe, Germany). Imaging was performed on a spinning disk confocal fluorescence microscope (Nikon Eclipse TE 2000-E) which was equipped with a Nikon Apo TIRF 100x/1.49 oil immersion objective. Samples were illuminated with laser light alternating between 488 nm and 633 nm for 300 ms each, exciting perylene and the cell membrane stain respectively. Image sequences were captured with an electron multiplier charge coupled device camera (iXon DV887ECCS-BV, Andor Technology, Belfast, UK). Several planes of the cells were imaged with a spacing of 166 nm and a detection time of 300 ms per plane.

Figure 5.6 b shows one exemplary confocal cross section (xy) through a HeLa cell and the reconstructed xz and yz profiles along the white lines. The nanoparticles are depicted in green, magenta represents the cellular membrane. The images show that most nanoparticles are localized within the boundaries of the membrane and hence have been taken up.

In addition, a differential interference contrast (DIC) image (Figure 5.6 a) of the cell was recorded which shows the cellular boundaries and the nucleus of the cell, both highlighted as white lines. Figure 5.6 c represents the overlay of the DIC image and the confocal cross section. The outer cellular boundaries that are visible in the DIC image, represented by the outer white line, and in the confocal cross section, shown as magenta oval, are not identical. The DIC image shows the boundaries of the cell at the level of the coverslip, the confocal cross section the magenta stained cell membrane about 2.7 µm above the coverslip. As no fluorescence signal is present inside the circle representing the nucleus, we conclude that no silica nanoparticles have been taken up into the nucleus.

5.7 Number of dye molecules per nanoparticle

The MPD-SiO₂ nanoparticles and the core-shell nanoparticles will serve as fluorescent tracers for nanoparticle cytotoxicity studies. To ensure that the interaction between nanoparticle and cell and not the interaction between the dye and the cell are investigated, it is very important that the dye is invisible to the cell. Therefore the core-shell nanoparticles which have the dye enclosed by a silica layer provide optimal conditions. But also the MPD-SiO₂ nanoparticles are well suitable for live-cell imaging if the fraction of dye covered surface (ca. 24 \AA^2 per dye molecule; DFT calculations PBE0

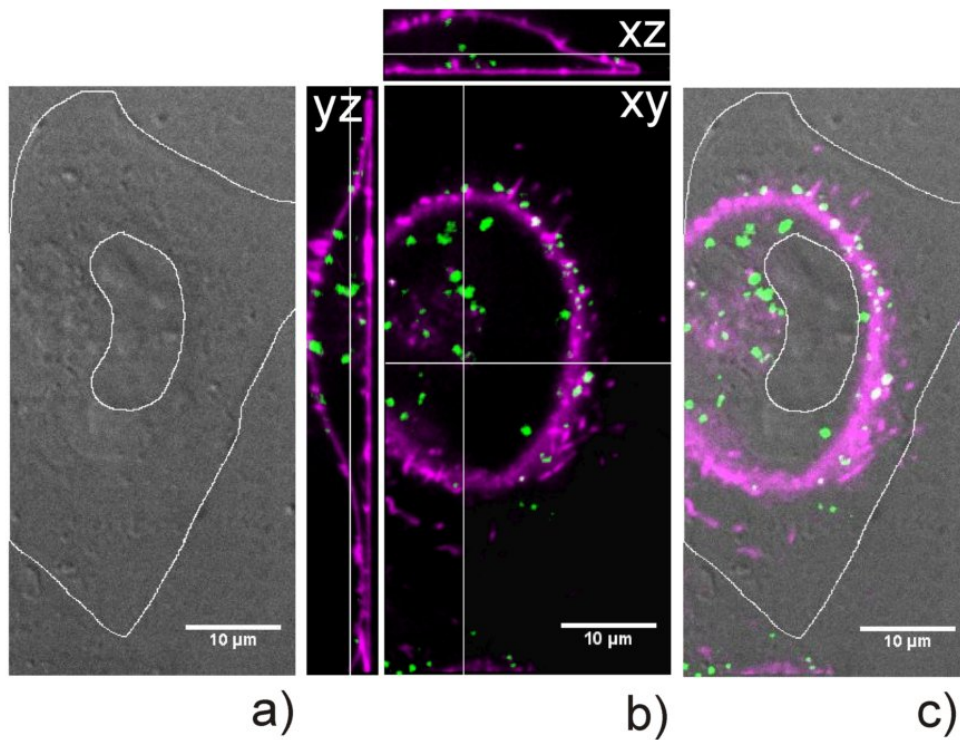


Figure 5.6: a) Differential interference contrast (DIC) image of a HeLa cell. The cellular boundaries and the nucleus are depicted as white lines. b) Fluorescent confocal cross section (xy) through the HeLa cell and the corresponding xz and yz profiles along the white lines in xy. The cellular membrane is shown in magenta and the nanoparticles are depicted in green. As the nanoparticles are localized within the cellular boundaries, they have been taken up by the cells. c) An overlay of the DIC image and the confocal cross section reveals that the nanoparticles are not localized within the nucleus.

5 Synthesis and characterization of SiO₂ nanoparticles

number of examined particles	diameter [nm]	σ (diameter) [nm]	average number of dye molecules/NP	σ (number of dyes/NP)
18	81	10	1.3	0.5
18	129	12	1.0	0.0
28	152	17	1.4	0.6

Table 5.1: Three sizes of MPD-SiO₂ nanoparticles (NPs) and the amount of dye molecules attached to each of the three MPD-SiO₂ nanoparticle types.

/6-31G**) is negligible in comparison to uncovered surface. This is true for nanoparticles with a diameter exceeding 90 nm which carry less than 1000 surface bound perylene molecules as these nanoparticles have less than 1% of their silica surface covered by perylene.

For low dye concentrations, the content of perylene dye molecules per nanoparticle can be determined by confocal microscopy and single molecule spectroscopy. In the following, the quantification of the amount of dye molecules per nanoparticles for three different types of MPD-SiO₂ nanoparticles with very low labeling density is described. In addition to the number of dyes this evaluation allows us to see whether the nanoparticles are homogeneously labeled. To prepare the sample, an aqueous suspension of MPD-SiO₂ nanoparticles is sonicated and spincoated onto a coverslip. The latter is placed on the confocal microscope and the position of the nanoparticles is determined by scanning a part of the sample very quickly (Figure 5.7 a). Afterwards single MPD-SiO₂ nanoparticles are excited continuously and the emitted photons are counted by an avalanche photo diode. The excited dye molecules bleach one after the other leading to a stepwise decrease of emitted photons. The number of steps is equal to the amount of dye molecules inside the confocal volume. If only one molecule is present the fluorescence bleaches in one step (Figure 5.7 b), two dye molecules lead to a two step decrease in fluorescence intensity (Figure 5.7 c). In addition, as indicated in Figure 5.7 b, the one-step bleaching curve shows two blinking events which is a typical behavior of single dye molecules. All three types of MPD-SiO₂ nanoparticles were homogeneously functionalized with one to two perylene molecules each (see table 5.1).

This technique is only applicable for very low dye concentrations, as for higher concentrations the stepwise bleaching converts into an exponential decay curve preventing manual counting of bleaching events. In order to estimate the number of dye molecules per nanoparticle for higher labeling density, we correlated the number of photons emitted by the particles within the first microseconds to the number of dye molecules counted during stepwise bleaching experiments. To obtain a correlation between the number of emitted photons and the amount of dye, we used data from 5 different nanoparticle species with low dye concentrations (see Figure 5.8 a). Following the stepwise bleaching curves, three particle species had an average number of 1.3 or 1.4 dye molecules attached to their surface, for the other two we counted an average number of 5.3 and 5.5 dye molecules per particle.

To test this method, three further nanoparticle species were synthesized. Based on the results for low dye concentrations, these particles were aimed on having 10 dye molecules per particle attached to their surface. The number of emitted photons was determined within the first microseconds

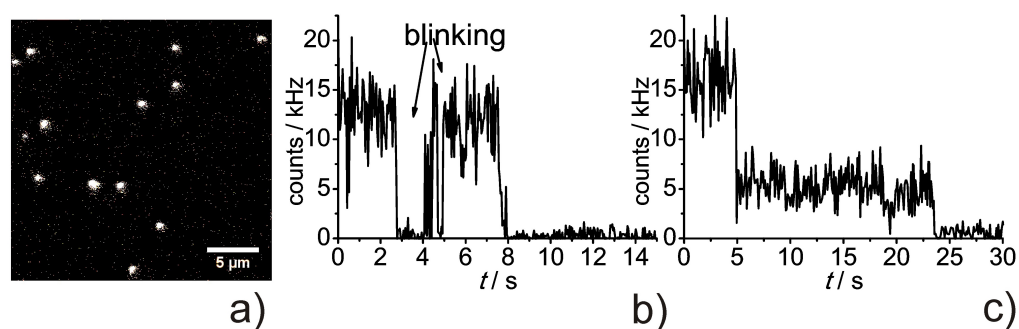


Figure 5.7: a) Confocal fluorescence image of SiO₂ nanoparticles labeled with monofunctionalized perylene and typical fluorescence intensity trajectories of nanoparticles that were labeled with b) one dye and c) two dyes.

of fluorescence emission for at least 58 nanoparticles of each type. The mean number of emitted photons was used to calculate the mean number of dye molecules per particle based on the previously obtained correlation. The mean values and the corresponding standard deviations are depicted in Table 5.2, the corresponding graph in Figure 5.8 b. The number of dye molecules attached to the three particle species increases with particle size. The two smaller nanoparticle types with diameters of 109 nm and 126 nm have 17.0 ± 9.3 and 23.7 ± 13.4 dye molecules attached to their surface each. Taking into account the broad standard deviation, these values are quite close to the 10 dye molecules per nanoparticle aimed for during synthesis. The biggest nanoparticle type seems to carry 72 ± 32.3 dye molecules per nanoparticle thereby clearly exceeding the aim of 10 molecules per particle. The increase in dye number with increasing size is very reasonable as the labeling density per nm² stays rather constant for all three particle types. At the used labeling conditions 0.46 - 0.48 dye molecules attached per 1000 nm² surface area to each nanoparticle.

Nevertheless this method for determining the dye number on the nanoparticle's surface has to be used with caution. Already the data used for calculating the regression line (Figure 5.8 a) contains several uncertainties. The determination of dye densities of around 1-3 dye per nanoparticle is quite reliable as the steps are clearly visible in most cases. If more dyes are attached to the nanoparticle's surface, the steps become more and more hidden and hard to count. Only a minority of bleaching curves allows to estimate the number of dyes on each particle. This bears the risk that the number of dye molecules is underestimated as lower numbers are counted with a higher probability than higher ones. Furthermore the intensity obtained for each particle which is correlated to the number of dyes per nanoparticle surface is broadly distributed as is reflected by the standard deviation. Reasons for this might be heterogeneities in the labeling efficiency but most likely they result from measurement conditions. During measurement, the focus and xy position of each particle is set manually. Therefore an equal excitation for all nanoparticles cannot be guaranteed. Furthermore the correlation calculated from data representing a labeling density of 1 to 5 dye molecules is used to extrapolate much higher numbers of dye molecules per nanoparticle. Such an extrapolation should

5 Synthesis and characterization of SiO₂ nanoparticles

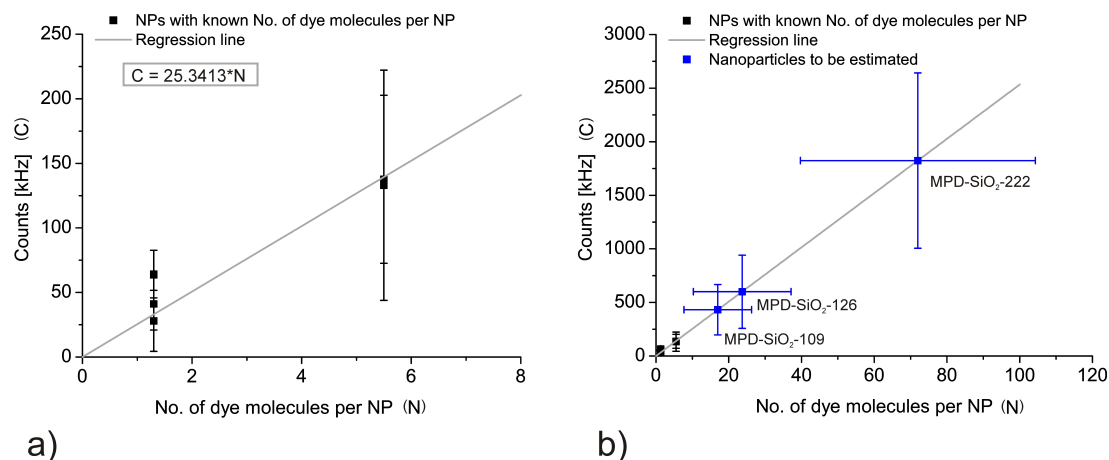


Figure 5.8: Linear regression used to determine the number of dye molecules attached to the surface of each nanoparticle for three different SiO₂ nanoparticle species with different sizes. a) The regression line was calculated by correlating the intensity of 5 nanoparticle types to the number of dye molecules on their surface. b) The number of dye molecules per nanoparticles for the three unknown particle types was then estimated using their fluorescence intensity and the parameters from the regression line.

in general be avoided. For the reasons mentioned, this technique to calculate the number of dye molecules per nanoparticle surface was not further applied throughout the work. Other methods to determine the nanoparticle-labeling densities are currently under development.

NP name	MDP-SiO ₂ -109	MDP-SiO ₂ -126	MDP-SiO ₂ -222
NP diameter [nm]	109	126	222
No. of NPs	64	58	67
Mean no. of emitted photons/NP [kHz]	431.5	599.7	1824.5
σ (no. of emitted photons/NP) [kHz]	235.0	340.8	817.9
No. of dye/NP	17.0	23.7	72.0
σ (number of dyes/NP)	9.3	13.4	32.3
No. of dye/ 1000nm ² surface area	0.46	0.48	0.47

Table 5.2: Data obtained from three types of MPD-SiO₂ nanoparticles (NPs) with different sizes which were aimed on having 10 dye molecules attached to each nanoparticle. Their labeling density was estimated by determination of their fluorescence intensity within the first microseconds after excitation showing that they carried approximately 17, 23.7 and 72 dye molecules on their surface.

Dye	Size [nm]	Name
-	304	SiO ₂ -304
monofunctionalized Perylene	310	MPD-SiO ₂ -310
bifunctionalized Perylene	18(*)	BPD-SiO ₂
Atto488	89	Atto488-SiO ₂ -89
Cy3	80	Cy3-SiO ₂ -80

Table 5.3: Nanoparticle species used in the experiments throughout this work.
(*) average diameter of particles within the network

5.8 Terminology of the particles used in this work

Besides the described MPD-SiO₂ nanoparticles, unlabeled amorphous silica particles, amorphous silica nanoparticles labeled with Atto488 and mesoporous silica nanoparticles labeled with Cy3 were investigated in the following experiments. The unlabeled and Atto488 labeled nanoparticles were synthesized similar to MPD-SiO₂. Details about the synthesis of the Cy3 labeled species can be found in Section 6.2. Throughout this work, the nanoparticles are termed applying the following scheme: Dye-SiO₂-size[nm]. An overview about the used particle species can be found in Table 5.3.

5.9 Summary and conclusions

We have demonstrated the syntheses of two different types of perylene labeled SiO₂ nanoparticles and of a fluorescent SiO₂ nanoparticle network. Silica nanoparticles with perylene dye linked to the surface (MPD-SiO₂) result from Stöber synthesis in presence of the monofunctionalized perylene derivative MPD. The addition of the bifunctionalized perylene derivative BPD during Stöber synthesis leads to the formation of a silica nanoparticle network (BPD-SiO₂). Nanoparticles with a perylene core and silica shell (core-shell nanoparticles) were obtained by performing the reaction in a micelle. The attachment of MPD to the nanoparticles was shown by transmission electron microscopy and an overlay of fluorescence and TEM images. As the nanoparticles will be used as tracers for live-cell imaging measurements it is crucial to know the location of the dye. We distinguish between dye molecules that are located on the surface of the nanoparticles and dye molecules that are located inside the core. The latter are invisible for the cell, and nanoparticles with dye cores are therefore optimally suited for nanoparticle toxicity essays. The dye molecules of the core-shell nanoparticles fulfill these requirements whereas the dye molecules of MPD-SiO₂ and BPD-SiO₂ are located on the surface of the nanoparticles as was shown by fluorescence spectroscopy and fluorescence anisotropy measurements. However, as the MPD-SiO₂ nanoparticles have only a low fraction of their surface covered by dye molecules, they are also suitable as tracers for live-cell imaging. In order to prove that the MPD-SiO₂ nanoparticles are homogeneously labeled we determined the amount of dye molecules per nanoparticle by confocal microscopy combined with single molecule spectroscopy. We proved for three types of MPD-SiO₂ nanoparticles with different sizes that they were homogeneously labeled with one to two dye molecules each. Since the nanoparticles

5 Synthesis and characterization of SiO₂ nanoparticles

are designed for live-cell imaging, we showed that MPD-SiO₂ nanoparticles are taken up by HeLa cells. After 4.5 h of incubation they were located inside the cellular boundaries but not inside the nucleus.

Having in hand the technique for preparing labeled silica nanoparticles and especially nanoparticles with a fluorescent core encapsulated in a shell of silica, we plan to extend this synthetic principle to other technically important nanoparticle materials, such as titanium dioxide, zinc oxide and cerium dioxide. An additional interesting option is the further improvement of the fluorescence behavior by the control of the internal structure and morphology of the core-shell nanoparticles [128].

6 Image analysis by Nano_In_Cell_3D

The quantification of nanoparticles inside the cytosol gives important information about the amount of nanoparticles that interacts with each individual cell. From the perspective of a concentration-dependent cytotoxicity assessment this information is very useful as nanoparticle number and the resulting cytotoxic effects can be directly correlated. A variety of methods are available to quantify nanoparticle uptake, which are designed for different requirements. These methods include fluorescence-based techniques like confocal microscopy, flow cytometry or quenching. But also electron microscopy, stereology, radioactive tracers, magnetic nanoparticles in combination with magnet resonance imaging, mass spectrometry or field flow fractionation can be used to quantify nanoparticle uptake [129]. The most common method is probably flow cytometry, where the total intensity of single cells or their light scattering behavior are correlated to particle uptake [130–132]. This method provides very good statistics as huge numbers of cells are evaluated in each experiment. However, this method has some limitation. Particle numbers are usually expressed in a relative and not in an absolute way. Moreover, the localization of the particles within the cell cannot be accessed directly. Another suitable fluorescence microscopy-based method to determine nanoparticle uptake are quenching experiments [133, 134]. They are carried out on a single-cell level and provide direct insight on cellular processes and nanoparticle localization. The nanoparticles are visible as individual spots and can be counted to get a rough estimation about their quantity provided that agglomeration is negligible. As quenching experiments are done on individual cells, they are very time consuming and are therefore not suitable for routine measurements. Both flow cytometry and quenching have their strengths and are very useful for specialized questions. It is of great interest to combine their advantages of giving direct insight into nanoparticle-cell interactions with the assessment of good statistics. This is a challenging task as a large number of single-cell images must be evaluated in detail allowing only a minor effort per image to gain statistically relevant results with a reasonable expenditure of time. Automated digital image routines are an excellent option to enable that. The application of digital methods to biological research, especially cellular imaging, has increased steeply in the recent years [135–138]. Advances in this field have made it easier to obtain reliable software and analytical tools for varying purposes. One example of an image processing and analysis program is the freely available and widely used ImageJ software [139]. A commercially available technique dealing with fluorescence microscopy of cells and computer vision techniques is known as high-content analysis. Largely used by pharmaceutical industry and research, the high-content analysis has become an essential tool in image-based cell assays intended for drug discovery [140, 141]. Nevertheless these methods have been developed for two-dimensional images and are usually not capable of processing three-dimensional representations of cells [142]. We developed a digital method to quantify the uptake of nanoparticles into cells, the Nano_In_Cell_3D ImageJ

macro. This macro is able to semi-automatically process stacks of confocal cross-sections of individual cells. It thereby quantifies the number of nanoparticles inside the cell and within the cell membrane region. In addition, *Nano_In_Cell_3D* provides an automatic segmentation of the cell, a routine to quantify nanoparticles in cell-free regions and a possibility to analyze the fluorescence intensity of individual nanoparticles. The macro was developed together with Adriano A. Torrano during his master thesis. It is presented in the following chapter which is adapted from and based on the publication “A fast analysis method to quantify nanoparticle uptake on a single cell level” [5] which was recently submitted to *Nanomedicine*.

6.1 The *Nano_In_Cell_3D* ImageJ macro

Nano_In_Cell_3D is designed to investigate the uptake of nanoparticles into cells by processing stacks of cellular cross-sections obtained by confocal fluorescence microscopy. In order to automatically detect the particles and the cellular boundaries, both structures have to be labeled with spectrally separable fluorescent dyes. After image acquisition, the image of the nanoparticles and the image of the cell have to be separated so that they can be processed by *Nano_In_Cell_3D*. Thus our image analysis routine executes series of ImageJ commands to process confocal images acquired in two separate fluorescent channels during single-cell uptake experiments (available for download at http://imagejdocu.tudor.lu/doku.php?id=macro:nano_in_cell_3d). This digital method works by using the image of the plasma membrane to segment the cell in order to define regions of interest (ROI) inside the cell and in an enlarged membrane region (e-membrane). The defined ROI are employed to delineate the regions in which nanoparticles will be classified and counted. Although devised for quantifying the incorporation of nanoparticles by cells, it should be noted that this method can in principle also be applied for studying the uptake of other fluorescent objects of interest (e.g. virus, molecules and proteins). In the following, the *Nano_In_Cell_3D* macro is described in detail. At the beginning of the digital evaluation, the user is guided through easy-to-follow dialog boxes and is required to select the image files, choose a directory for results and enter the parameters for analysis. After this initial step, semi-automatic segmentation and quantifying processes take place.

6.1.1 Three-dimensional reconstruction of the cellular ROI

The spatial position of the cell is determined by processing the confocal stacks representing the cellular membrane (Figure 6.1 a). The segmentation starts by smoothing the image with a Gaussian filter and is followed by an automatic threshold selection (IJ_ Isodata [139]). The thresholded image is then converted into a binary image - the mask of the cell membrane (Figure 6.1 b). After this, the user is requested to verify the image stack and enter the first and the last slices constraining the cell along the z-direction. Only the chosen substack will be evaluated. At this point, to allow the evaluation of a variety of cell shapes, two independent segmentation strategies (S1 and S2) are applied. The segmentation path S1 uses the cell membrane position within the top plane of the stack as a seed. This seed is used to track down the mask through the stack. Slice after slice,

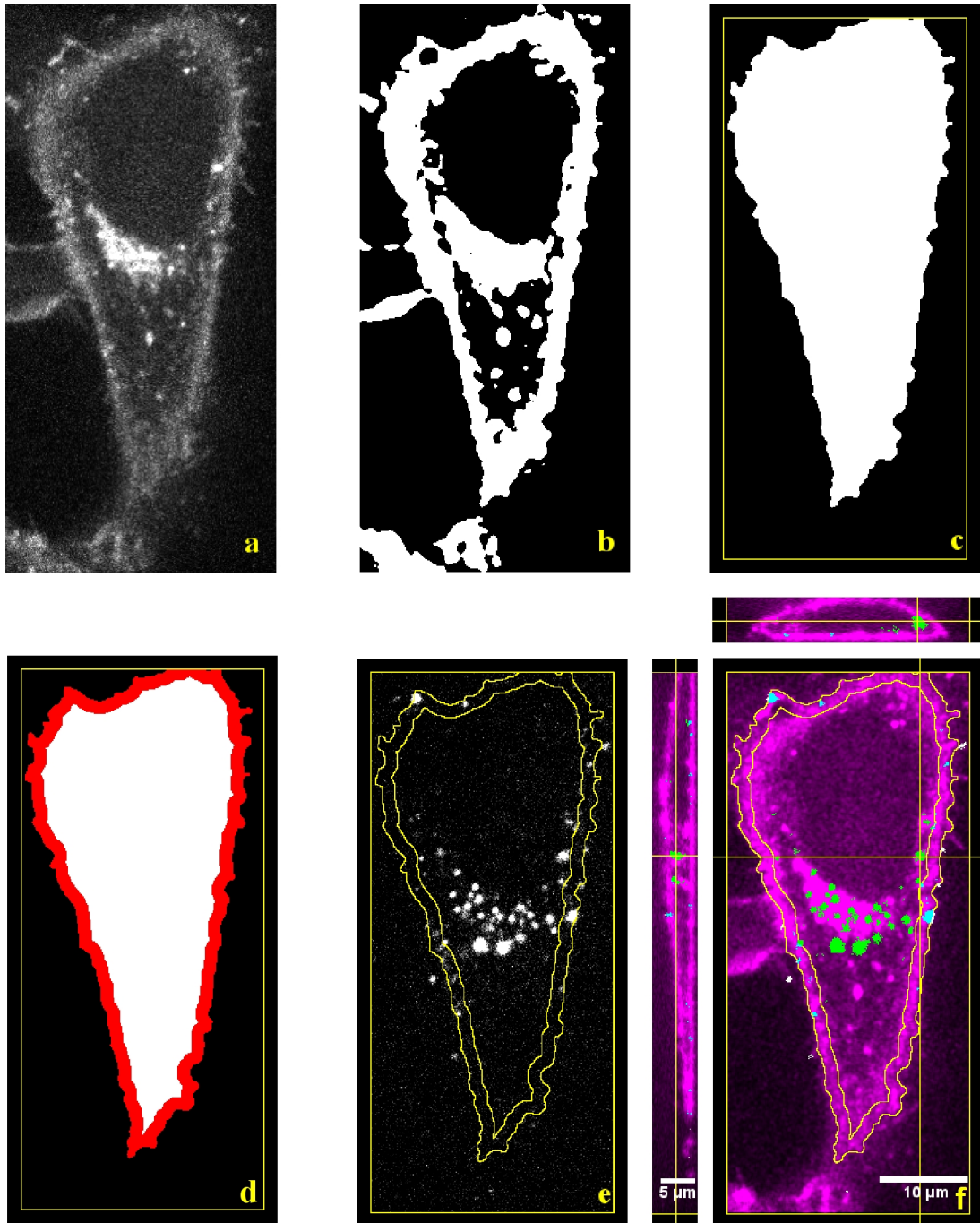


Figure 6.1: Nano_In_Cell_3D processing overview. a) Representative confocal cross-section image of a HeLa cell plasma membrane stained with CellMaskTM Deep Red. b) The image of panel a is transformed into a white mask. c) Further segmentation processes form the final mask of the cell. d) Afterwards its outer border is shrunk to define the enlarged membrane region (e-membrane, in red) and the region inside the cell (in white). The procedure occurs throughout the image stack, leading to a 3D reconstruction of the system. e) E-membrane outlines (in yellow) are employed to segment the image of the fluorescent nanoparticles. f) Merged image with orthogonal views along the yellow lines displaying the entire stack. The cell plasma membrane appears in magenta while the e-membrane outlines are shown in yellow. Nanoparticles are assigned to three different regions: inside the cell (in green), outside the cell (in gray) and within the e-membrane (in cyan).

the mask of the stained membrane is transformed into the mask of the whole cell by filling closed patterns with white pixels and clearing the outside of the patterns (Figure 6.1 c). The segmentation path S2 uses the same processes as S1, but before filling the closed patterns with white pixels, the image of every individual slice is copied and then pasted over the following slice. Now, the user has to choose which of the segmentation strategies represents the cellular boundaries in a better way. Therefore the outlines of the masks from S1 and S2 are each superimposed on the image stack of the cell and displayed. The outlines of the chosen mask form the outer cellular ROI (Outer-ROI). In a subsequent step, the Outer-ROI is shrunk by a given distance (see Section 6.1.2), generating the Inner-ROI. The e-membrane is defined as the region between Inner- and Outer-ROI. The criteria to choose the thickness of the e-membrane correctly are given in Section 6.2. As shown in Figure 6.1 d, three distinct regions are achieved: inside the cell (in white), outside the cell (in black) and the e-membrane (in red). The classification of the nanoparticles within the cell can be visualized by color coding the confocal images (see Figure 6.1 f).

6.1.2 Input of analysis parameters

The possibility of adapting the analysis parameters according to experimental conditions increases the flexibility of this method. The following parameters have to be set by the user and are saved in a final report:

Background to be subtracted: This parameter is used to correct for the background present in each image. The intensity value of each pixel in the stack representing the nanoparticles is subtracted by the entered value. If no subtraction is needed (e.g. background was removed by another method), this parameter should be set to zero.

Integrated density per nanoparticle (*IntDens_NP*): The *IntDens* per nanoparticle (*IntDens_NP*) represents the mean fluorescence intensity of individual nanoparticles. It can be obtained by running the auxiliary routine Individual_NPs, described below. The *IntDens_NP* is needed to calculate the absolute number of nanoparticles. For that, the total integrated density (*Total_IntDens*) which was assigned to specific regions during evaluation is compared to the *IntDens_NP* giving an estimation of the local population of nanoparticles. More details on the calculation are given in the next section.

Threshold for nanoparticles: Only pixels with intensity values exceeding this threshold will be assigned as nanoparticles and thus analyzed. When correctly thresholded, the bright spots associated with the fluorescent objects form clusters of adjacent pixels and only these pixels are evaluated. This choice is fundamental for the whole analysis process as it has major influence on the results. If the threshold is set too low, artifacts like the background noise and cellular autofluorescence might be counted as nanoparticles. On the other hand, if it is set too high, dimmer particles will not be considered.

Enlarged cell membrane width: This parameter defines the distance w between the Inner- and the Outer-ROI. It is thereby equal to the width of the region between the intra- and the extracellular environments, the e-membrane.

xy-scale: Digital image lateral scale in nm per pixel.

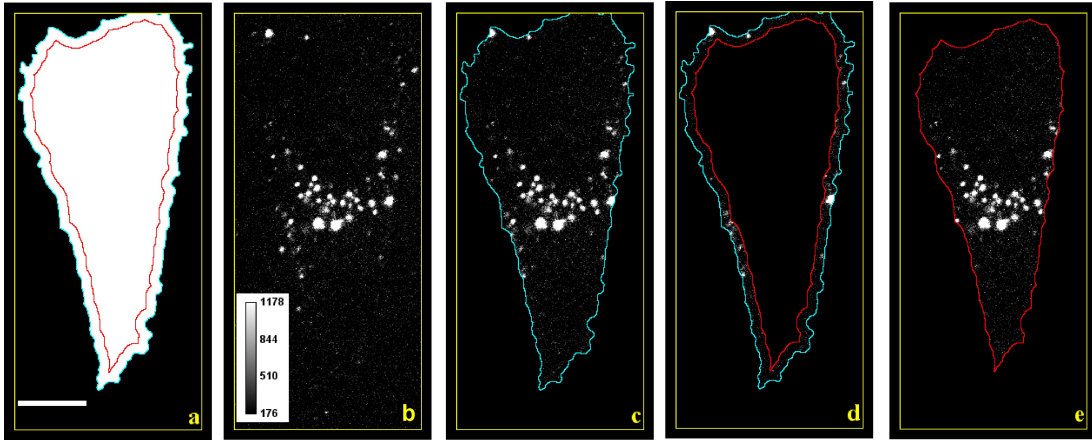


Figure 6.2: The cellular ROI are applied to segment the image of the nanoparticles. a) Segmentation mask of the cell (white) with Outer- and Inner-ROI in cyan and red, respectively. b) Background-corrected image of the nanoparticles with pixel intensities calibration bar. c) NPs-whole (cell) image is obtained by applying Outer-ROI to the image of the nanoparticles, of panel b. All pixels outside that region are cleared. d) NPs-e-membrane is obtained from NPs-whole with subsequent use of the Inner-ROI. e) NPs-inside, conversely, applies the Inner-ROI to erase the pixels lying outside of it. Scale bar = 10 μm

z-scale or Interslice distance: Vertical scale of the digital images in nm per pixel. This value is given by the distance between two adjacent confocal optical sections; every cross-section builds up one slice with one pixel in height forming volumetric pixels or voxels. To ensure that the whole cell is sampled, images should be acquired following the Nyquist criterium [83].

With all parameters entered, the next steps are completely automatic.

6.1.3 Nanoparticles assignment to different regions according to cell position

The above defined Outer- and Inner-ROI (Figure 6.2 a) are used to segment the image of the nanoparticles (Figure 6.2 b) and create three new images: NPs-whole (cell), NPs-e-membrane and NPs-inside. The image NPs-whole (Figure 6.2 c) is obtained by applying the Outer-ROI to the original image of the nanoparticles (Figure 6.2 b); the intensity values of the pixels outside that region are turned into zero. NPs-e-membrane (Figure 6.2 d) is obtained with subsequent application of the Inner-ROI. This time the pixels inside the selection are cleared and only the e-membrane is preserved. To achieve the image NPs-inside (Figure 6.2 e), the Inner-ROI is employed to erase the pixels that are outside of it.

6.1.4 Analysis of nanoparticles and results

During this processing step, NPs-whole, NPs-e-membrane and NPs-inside images are analyzed according to the pre-set conditions. We thereby use the fact that during the image acquisition, the photons that are collected at each pixel (e.g. by a charged-coupled device) are converted into pixel intensities (PI). Each 16-bit pixel carries an intensity value that ranges from 0 to 65535 and these

6 Image analysis by Nano_In_Cell_3D

values are correlated to the number of fluorophores present at the scanned volume [143]. Thus we assume that the sum of all PI (integrated density or $IntDens$) in a region is proportional to the amount of nanoparticles in that region. Nano_In_Cell_3D thereby does not count individual nanoparticles by simple counting of bright spots, but accesses the number of particles indirectly by integrating their fluorescence intensities. During processing, pertinent data as $Area$ (in pixels), PI and $IntDens$ are systematically extracted from the images. The $IntDens$ of a group of m thresholded pixels is calculated as follows,

$$IntDens_i = \sum_{k=1}^m (PI)_k \quad (6.1.1)$$

where each pixel is indexed by the letter k . This therefore corresponds to the $IntDens$ of one spot in one image slice. The $Total_IntDens$ of a region R (WHOLE CELL, E-MEMBRANE, INSIDE) is defined as the sum over all spots, in all stacks, of all $IntDens$ values belonging to that region:

$$(Total_IntDens)_R = \sum_{i=1}^n (IntDens_i)_R \quad (6.1.2)$$

where i indexes all measurements arising from nanoparticles appearing in the entire image stack and n is the total number of measurements. From these results, the number of nanoparticles ($\#NPs$) in each region R is achieved by simple arithmetic division:

$$(\#NPs)_R = \frac{(Total_IntDens)_R}{IntDens_NP} \quad (6.1.3)$$

where $IntDens_NP$ stands for the $IntDens$ attributed to one nanoparticle (see Section 6.1.2). As Nano_In_Cell_3D does not count the number of individual spots, but integrates over the intensity assigned to the particles, it is able to correctly assess the quantity of nanoparticles, even if they are lying directly above each other or if they are agglomerated. We thereby assume that the self-quenching in particle agglomerates is negligible. The sampled volume of each cellular region R is calculated in volumetric pixels (voxels) and then converted to μm^3 according to the pre-set xy- and z-scales. The concentration of nanoparticles ($Concentration$) within each region is obtained by dividing the number of nanoparticles by the respective sampled volume,

$$(Concentration)_R = \frac{(\#NPs)_R}{(Volume)_R} \quad (6.1.4)$$

The total number of nanoparticles interacting with each cell is equal to the sum of nanoparticles in the e-membrane and inside the cell. This total number is then compared to the number of internalized particles to deliver the fraction of nanoparticle uptake, calculated by

$$Fraction_of_NP_Uptake(\%) = \left(\frac{(\#NPs)_{INSIDE}}{(\#NPs)_{INSIDE} + (\#NPs)_{E-MEMBRANE}} \right) \cdot 100 \quad (6.1.5)$$

After the calculation, four-color images of the entire stack are created by color coding the nanopar-

ticles according to their assigned cellular location (see Figure 6.1 f), allowing the direct 3D visualization of the analyzed system (Figure 6.6). Finally, a text file is created containing a report documenting the input parameters and the results. In addition, the main processed images and results tables are saved.

6.1.5 Auxiliary routines

Additionally to the main routine, the algorithm is structured to run three other auxiliary routines: Outside_Region, Individual_NPs and Segmentation. The selection is done at the very first processing step via a check box window. The auxiliary routines are briefly described below.

Outside_Region routine: This routine was designed to investigate the concentration of nanoparticles in cell-free regions. This information is relevant for uptake kinetics studies because the amount of particles available for the cells may vary with time due to sedimentation and diffusion of particles in the cell medium. Valuable information, as e.g. the nanoparticles deposition rate, can be assessed by employing this method.

Individual_NPs routine: This routine was devised to obtain the *IntDens_NP*. This key parameter is used to quantify the number of particles in an image by simply dividing the *Total_IntDens* in that region by *IntDens_NP* (see Equation 6.1.1). The user is asked to select the objects of interest in the image of the nanoparticles and add them to ImageJ ROI Manager. One after the other, the selected nanoparticles are measured and saved in a result table. In the end, a report of results shows the *IntDens_NP* of all evaluated objects in a row. This data can be easily transferred to another program of choice in order to e.g. perform a statistical treatment. An example of how to calculate the mean *IntDens_NP* correctly can be found in the Section 6.2.

Segmentation routine: This routine is intended to be used when only the segmentation of images, without analyzing the nanoparticles, is desired.

6.2 Setting of parameters and validation of Nano_In_Cell_3D

With the aim of validating the new procedure, Nano_In_Cell_3D was used to determine the number of 80nm (DLS) quenchable colloidal mesoporous silica nanoparticles labeled with Cy3 (Cy3-SiO₂-80) [144] interacting with HeLa cells in two-channel spinning disk confocal images. Initially, control experiments were employed to set the threshold for nanoparticles, the *IntDens_NP* and the e-membrane width. Subsequently, the nanoparticles taken up by individual cells were quantified within different incubation times. These results were then used to assess the fraction of internalized Cy3-SiO₂-80. Finally, the outcomes were compared with those obtained via quenching experiments conducted in parallel. The quenchable mesoporous nanoparticles used for these experiments were synthesized by Christian Argyo (AK, Prof. T. Bein, LMU München). First, the nanoparticles were prepared as described in [144]. Afterwards, the mesoporous nanoparticles were functionalized at their periphery with aminopropyl- and PEG-groups through co-condensation, followed by grafting the dye Cy3 NHS ester. The dye labeling was carried out with an ethanolic suspension of the particles having a concentration of 1 mg/mL by adding 14.2 μ L of dye Cy3 NHS ester solution (2 mg/mL

in DMF). The reaction solution was stirred for 1 h at room temperature in the dark, then the Cy3-SiO₂-80 particles were collected by centrifugation (14000 rpm for 5 min), washed three times with ethanol, and finally redispersed in water to a final concentration of 0.5 mg/mL.

6.2.1 Threshold and intensity of individual nanoparticles

The *IntDens_NP* and the threshold were acquired by evaluating nanoparticles that were lying in cell-free regions on the coverslide applying the auxiliary routine *Individual_NPs*. During this routine, the regions of interests are drawn around the individual nanoparticles by hand and are added to the ROI-Manager of ImageJ. In a subsequent step, the slices where the particles are visible are selected. After setting the background value and the range of thresholds to be evaluated, each individual nanoparticle is analyzed. To gain the mean value of nanoparticle intensity, the values of the individual nanoparticles were assigned to an intensity region and counted. The number of nanoparticle intensities in each intensity region were plotted, giving a histogram of intensity distributions. The distribution of *IntDens* was fitted to a log-normal function [145]. These steps were done for each threshold. We analyzed 322 individual nanoparticles for a threshold range of 100 - 1400 *PI*. Figure 6.3 shows the intensity distributions for the nanoparticles at a threshold of 400, 700 and 1000 *PI*.

The relation between the *IntDens_NP* and the threshold is well represented by an exponential decay curve (Figure 6.4 a, black curve). In order to prove that the proper number of nanoparticles is counted by using the calculated *IntDens_NP* values, we analyzed a cell-free region with nanoparticles by the auxiliary routine *Outside Region*. This routine calculates the *Total_IntDens* within a given region of interest. To obtain the number of nanoparticles, this *Total_IntDens* is divided by the *IntDens_NP*. The *Total_IntDens* is also threshold dependent and follows a similar exponential decay curve as the *IntDens_NP*. Both, the threshold dependency of the *IntDens_NP* and of the *Total_IntDens* are shown in Figure 6.4 a. This has the effect that even though the *IntDens_NP*, is strongly influenced by the threshold, the number of nanoparticles counted within a proper threshold range is constant. In Figure 6.4 b, the threshold dependency of the calculated nanoparticle number is shown. The number of nanoparticles decreases for increasing thresholds (100 - 400 *PI*) before reaching a constant value. The strong threshold dependency is due to background noise that is considered as particles when the threshold is too low. This is clearly visible from the left inset in Figure 6.4 b. The counted particle number therefore exceeds the real number. For thresholds from 400 to 1200 *PI* the nanoparticle number stays constant and nanoparticles are counted correctly. For higher thresholds, some particles are not considered any more (see Figure 6.4 b, white arrow at right inset). For this reason a threshold between 400 and 1200 *PI* should be chosen for further evaluation. Another aspect to be considered for threshold selection is the autofluorescence of the cells. The cellular autofluorescence could increase the number of particles counted if the autofluorescence is wrongly considered as nanoparticle signal. Therefore we imaged and evaluated stained cells which were not incubated with nanoparticles as control experiment. The threshold dependent results of 7 individual HeLa cells are shown in Figure 6.5.

The number of nanoparticles that was wrongly counted in the empty cells was considerable high

6.2 Setting of parameters and validation of Nano_In_Cell_3D

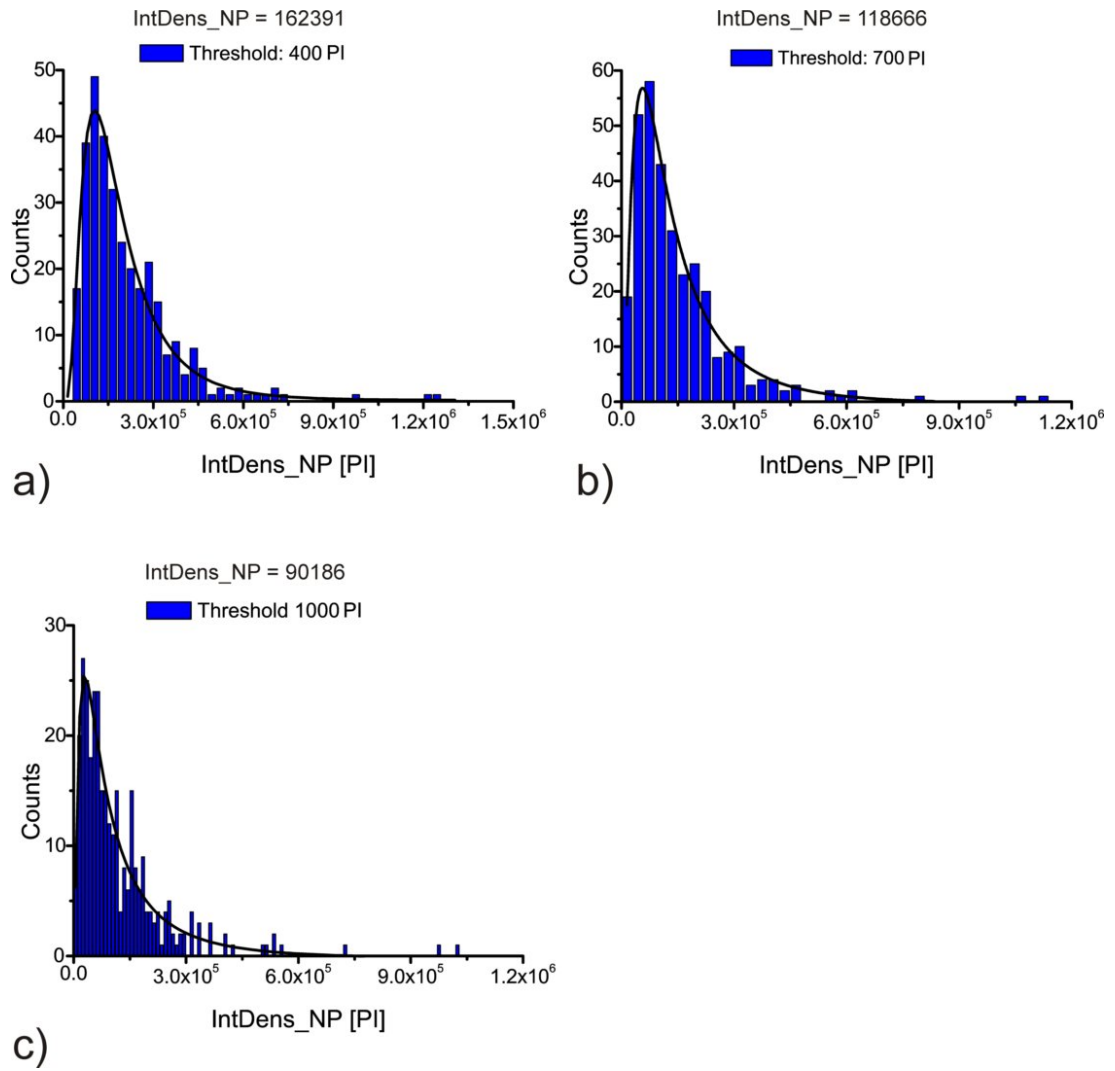
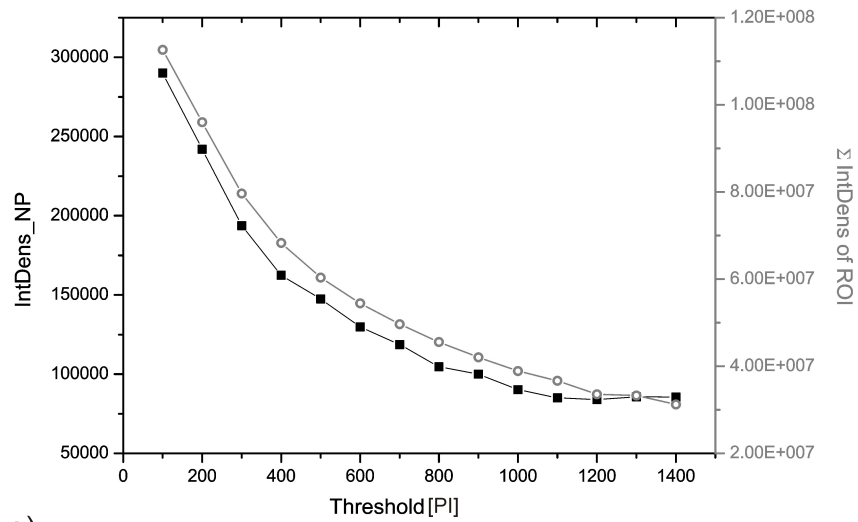
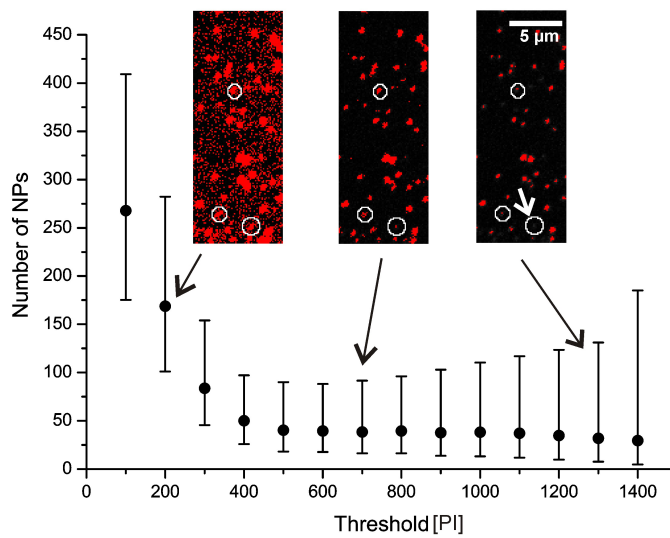


Figure 6.3: *IntDens* distribution of more than 300 individual particles thresholded at a) 400 *PI*, b) 700 *PI* and c) 1000 *PI*. The data was fitted to a log-normal function so as to obtain the *IntDens_NP*.

6 Image analysis by Nano_In_Cell_3D



a)



b)

Figure 6.4: a) *IntDens_NP* (black) and *Total_IntDens* within a given ROI (gray) as a function of the threshold. The *IntDens_NP* is strongly influenced by the threshold, even though the number of nanoparticles counted within a proper threshold range is constant as both curves have a similar threshold dependency. b) Threshold-dependent number of Cy3-SiO₂-80 nanoparticles (NPs) in a representative cell-free region. All insets show the same NPs image but at different thresholds. Some nanoparticles are marked with ellipses in cyan to help visualize the threshold influence. The number of nanoparticles was found to be approximately constant within the range of thresholds between 500 and 1100 *PI* (central inset), but dropped for values above 1200 *PI* because of vanishing nanoparticles (e.g. right inset, white arrow) and strongly increased for thresholds below 400 *PI* because of background noise intrusion (left inset).

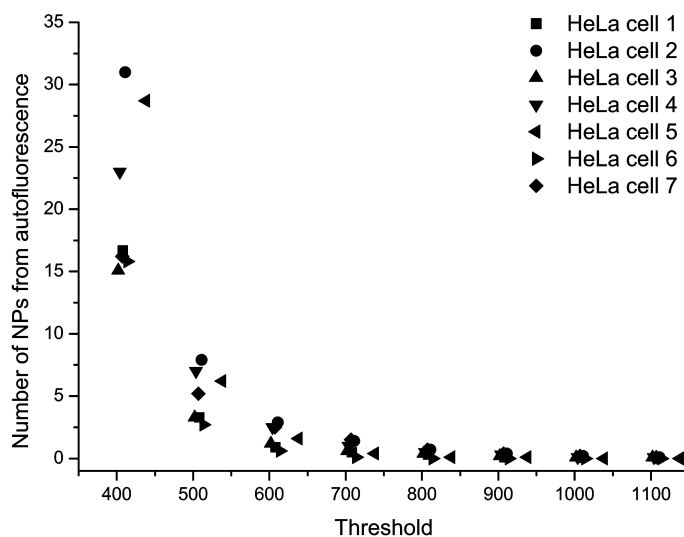


Figure 6.5: a) Single-cell experiments without Cy3-SiO₂-80 nanoparticles were used as blank assays to evaluate the cellular autofluorescence (AF). When the threshold was set at low values, the results show that HeLa cells' AF was mistaken by nanoparticles.

for thresholds below 500 *PI* whereas above 600 *PI* less than 5 nanoparticles were counted. Finally, combining the results of both experiments, a threshold of 700 *PI* and a *IntDens_NP* of 118766 *PI* were selected for the following experiments.

In order to show that this procedure can also be applied to other types of nanoparticles with different sizes and labels, we evaluated two additional particle species. We chose amorphous silica nanoparticles with sizes of 310 nm (MPD-SiO₂-310) and 89 nm (Atto488-SiO₂-89) (TEM), labeled with perylene or Atto488, respectively. MPD-SiO₂-310 were synthesized as described before (see Chapter 5.1, [4]). For the synthesis of the Atto488-SiO₂-89 nanoparticles, the same instructions were used and adapted.

Figure 6.6 a shows the threshold dependency of the *IntDens_NP* for both particle types. Similar to the results for the Cy3-SiO₂-80 nanoparticles, the *IntDens_NP* decays exponentially with increasing thresholds. First nanoparticles started being lost during evaluation for thresholds exceeding 700 *PI* (MPD-SiO₂-310) and 1100 *PI* (Atto488-SiO₂-89), providing an upper limit for the threshold range to be investigated. In a subsequent step we calculated the absolute nanoparticle number lying in a given region on the cover slide and assessed its threshold dependency (see Figure 6.6 b). As for the Cy3-SiO₂-80, the number calculated for the Atto488-SiO₂-89 particles decreased for lower thresholds from 100 to 400 *PI* and was followed by a constant nanoparticle number for thresholds between 400 and 1100 *PI*. Interestingly, the number of nanoparticles obtained from evaluating the MPD-SiO₂-310 particles was rather constant throughout the whole threshold range. The observed differences probably originate from different noise levels present in the images (see insets). The higher the fluctuations in the background, the more noise is falsely counted as nanoparticles. The

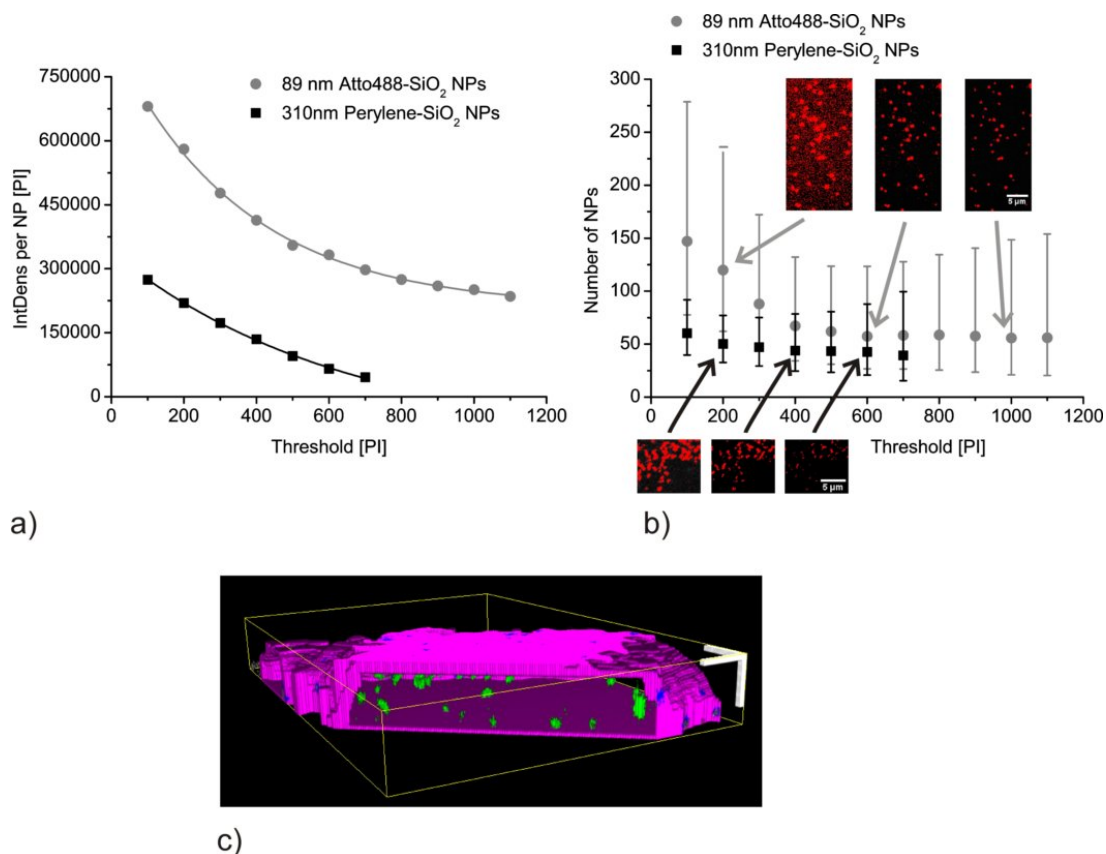


Figure 6.6: Threshold and *IntDens*_{NP} for 310 nm (MPD-SiO₂-310) and 89 nm (Atto488-SiO₂-89) amorphous SiO₂ nanoparticles. a) Threshold dependency of the *IntDens*_{NP} fitted to an exponential decay curve. b) Threshold-dependent number of nanoparticles in a representative cell-free region. The insets show images of both nanoparticle types at different thresholds. For the Atto488-SiO₂-89 particles, the number of nanoparticles was found to be approximately constant within the range of thresholds between 500 and 1100 *PI* (middle and right upper inset) and strongly increased for thresholds below 400 *PI* because of background noise intrusion (left upper inset). The number of MPD-SiO₂-310 nanoparticles remained roughly constant for the whole threshold range. c) 3D representation of a HeLa cell incubated with MPD-SiO₂-310 nanoparticles for 1 h after evaluation with Nano_In_Cell_3D. Cellular boundaries were reconstructed by the enlarged membrane region (e-membrane) and are shown in magenta. The analyzed nanoparticles are color-coded in green if located inside the cell and in cyan if assigned to the e-membrane; nanoparticles lying outside the cell volume are displayed in gray. Scale bars = 4 μm

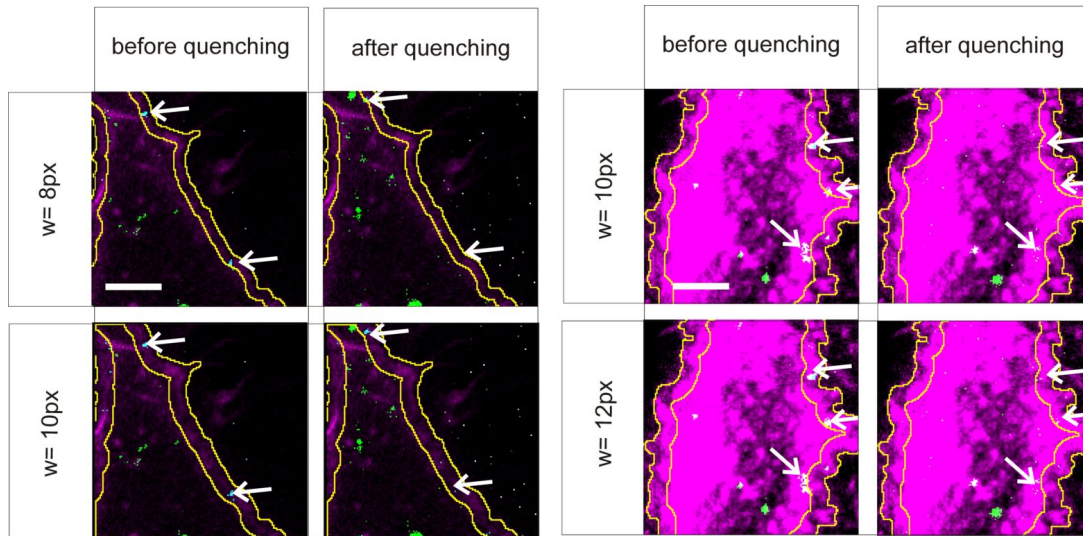


Figure 6.7: a) Confocal cross-section of two HeLa cells before and after quenching. The images were evaluated with Nano_In_Cell_3D applying different e-membrane widths. **left:** Cell evaluated with a e-membrane thickness of 8 px (1 μm) and 10 px (1.26 μm). The nanoparticle indicated by the lower white arrow is present in the plasma membrane or in the extracellular space and therefore quenched. It is correctly assigned to the e-membrane region by the macro applying both e-membrane widths. The upper white arrow shows a nanoparticle which remains fluorescent after quenching and is thus localized within the cytoplasm or in the e-membrane region. It is assigned to the cell membrane region in both cases. **right:** Cell evaluated with e-membrane thicknesses of 10 px (1.26 μm) and 12 px (1.51 μm). All arrows indicate nanoparticles that are quenched and have therefore not been taken up into the cell. The upper most particle is correctly assigned to the membrane region for both e-membrane thicknesses whereas the middle particle is only correctly assigned applying a e-membrane thickness of 12 px. For the lowest particle, the optimal e-membrane thickness would be even broader as it is assigned to the cytoplasm in both cases. This show that already within one individual cell an optimal e-membrane width doesn't exist and thus the best possible thickness has to be determined.

background and noise mainly result from nanoparticles diffusing in the cell medium that are not attached to the cover slide. As the 310 nm MPD-SiO₂-310 particles are sedimenting faster than the 89 nm Atto488-SiO₂-89 particles or the 80 nm Cy3-SiO₂-80 particles, the 310 nm particles have probably mainly settled on the cover slide whereas the smaller particles are still diffusing in solution. This clearly shows that each nanoparticle type may behave differently and therefore the threshold has to be determined for each nanoparticle type individually. For the two particles species shown, we propose a threshold between 400 - 1100 *PI* (Atto488-SiO₂-89 nanoparticles) and 200 - 600 *PI* (MPD-SiO₂-310 nanoparticles), depending on the autofluorescence of the cells. In additional experiments we were able to show that both particle types were internalized by HeLa cells. The 3D representation of a HeLa cell incubated for 1 h with the MPD-SiO₂-310 nanoparticles is shown in Figure 6.6 c.

6.2.2 E-membrane width

In a next step, the e-membrane width (w) has to be determined. The e-membrane width defines the thickness of the transition region between the extracellular and the intracellular spaces. As the Outer-ROI is defined by the fluorescence signal of the membrane staining, only the Inner-ROI can be changed. To determine the best value for w , we incubated HeLa cells with the quenchable Cy3-SiO₂-80 nanoparticles. We then stained the cell membrane and acquired stacks of confocal cross-sections of a single cell. Immediately after stacking, the nanoparticle fluorescence was quenched by the addition of trypan blue and another stack of the same cell was acquired. The images before and after quenching were processed by Nano_In_Cell_3D applying a variety of different e-membrane thicknesses and compared. The e-membrane thickness was chosen in a way that nanoparticles in the intracellular space were never quenched, nanoparticles assigned to the extracellular space were always quenched and particles in the e-membrane region, the transition region, were quenched or not. Figure 6.7 shows two cells before and after quenching for two e-membrane thicknesses each. The left cell was evaluated with an e-membrane thickness of 8 px (1 μm) and 10 px (1.26 μm). The lower white arrow indicates a nanoparticle which is quenched and therefore present in the plasma membrane or in the extracellular space. Using an e-membrane width of 10 px, the nanoparticle is clearly assigned to the e-membrane region by the macro. This is also true for 8 px but the nanoparticle touches the border of the Inner-ROI. The upper white arrow indicates a nanoparticle which is not quenched and therefore is located within the cytoplasm or in the e-membrane region. For both e-membrane thicknesses, it is assigned to the e-membrane region. The second cell on the right hand side is shown with e-membrane regions of 10 px (1.26 μm) and 12 px (1.51 μm) thickness. All arrows indicate nanoparticles that are quenched and have therefore not been taken up into the cell. The upper most particle was well assigned to the e-membrane region for both 10 px and 12 px e-membrane thicknesses. The middle particle is only correctly assigned using a 12 px e-membrane. For the lowest particle, even a higher e-membrane width value has to be considered. This shows that even for one individual cell an optimal e-membrane value does not exist. Therefore the best possible thickness has to be determined. By comparing several cells, we found that the optimal e-membrane thicknesses varied from 9 to 12 px in most cases. We therefore decided to use 11 px as this allowed us to describe most cells in a reasonable way.

6.2.3 Absolute number of nanoparticles

Having determined the threshold for nanoparticles, the *IntDens_{NP}* and the e-membrane width, the uptake of Cy3-SiO₂-80 nanoparticles into HeLa cells was investigated. HeLa cells were grown in Dulbecco's modified Eagle's medium (DMEM; Gibco, Karlsruhe, Germany) supplemented with 10% fetal calf serum (FCS), in 5% CO₂ humidified atmosphere at 37 °C. They were seeded 48 or 24 h before imaging on collagen A Lab-Tek-chambered cover glass (Nunc, Rochester, NY, USA) in a density of $1.0 \cdot 10^4$ or $2.0 \cdot 10^4$ cells/well, respectively.

HeLa cells were incubated within the time range of 1 to 6 hours with the Cy3-SiO₂-80 nanoparticles at a final concentration of 0.12-0.18 mg/mL in CO₂-independent medium (Invitrogen; Karlsruhe,

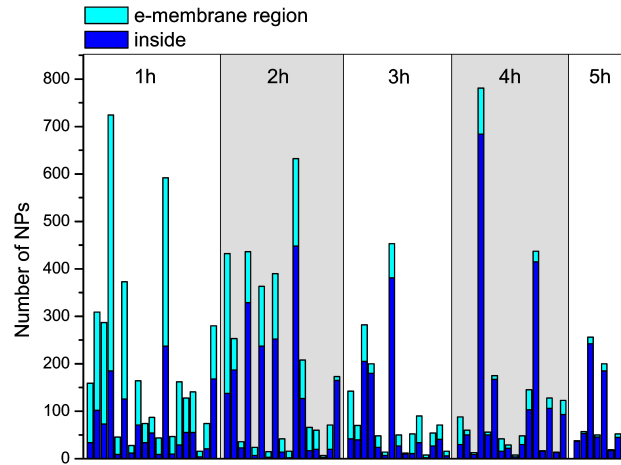


Figure 6.8: Number of Cy3-SiO₂-80 nanoparticles counted inside the cell (dark blue) and in the e-membrane region (light blue) for individual HeLa cells sorted by incubation time. The total height of the bar is equal to the number of particles in contact with each individual cell. With longer incubation times, the fraction of particles in the e-membrane region decreases in comparison to the number of particles which have been taken up into the cells.

Integrated Density per nanoparticle	118666 */ 1.8 <i>PI</i>
Threshold for nanoparticles	700 <i>PI</i>
Enlarged Membrane Region Width	11 pixels
XY-scale	126.1 nm/pixel
Z-scale or Interslice distance	166.0 nm/pixel

Table 6.1: Applied parameters for the measurement and evaluation of Cy3-SiO₂-80 uptake by the Nano_In_Cell_3D ImageJ macro.

Germany) with 10% FCS and placed on a heated plate (37 °C). After nanoparticle incubation, the cell membrane was stained with CellMaskTM (Invitrogen; Karlsruhe, Germany) and the medium was renewed. Imaging was performed on a spinning disk confocal fluorescence microscope based on Nikon Eclipse TE 2000-E equipped with a Nikon Apo TIRF 100x/1.49 oil immersion objective. Specimens were illuminated with laser light alternating between 488 nm and 633 nm for 300 ms each, exciting Cy3 and the cell membrane stain, respectively. Image sequences were captured with an electron multiplier charge-coupled device camera (iXon DV887ECCS-BV, Andor Technology, Belfast, UK). Single cells were imaged throughout z-direction with an interslice distance of 166 nm. The spinning disk microscopy images were evaluated by Nano_In_Cell_3D applying the parameters obtained following the description above. The parameters are summarized in Table 6.1.

More than 70 cells were imaged and then analyzed by the novel digital method Nano_In_Cell_3D. The absolute number of Cy3-SiO₂-80 nanoparticles interacting with the individual cells was calculated and is shown as a histogram in Figure 6.8. Each individual bar represents a single cell. The

6 Image analysis by Nano_In_Cell_3D

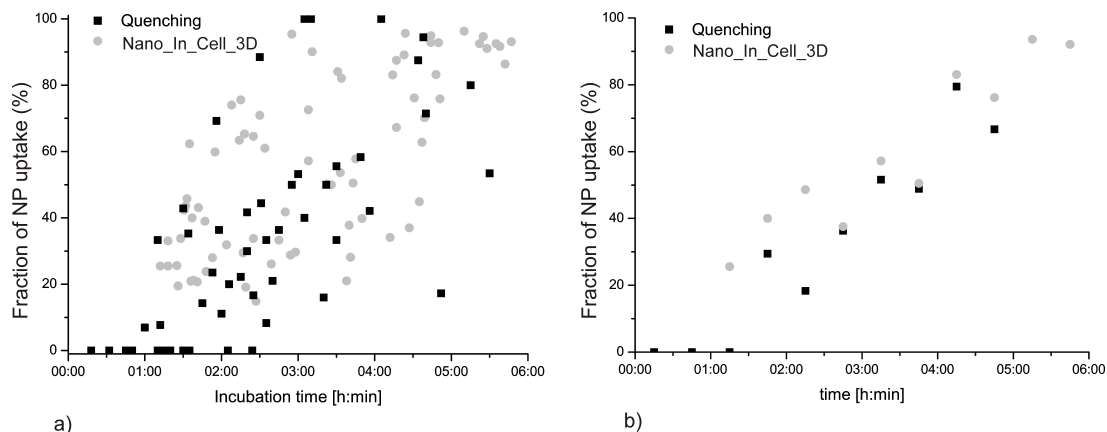


Figure 6.9: Fraction of internalized $\text{Cy3-SiO}_2\text{-80}$ particles in HeLa cells analyzed by Nano_In_Cell_3D and by quenching experiments. a) The fraction of particles internalized by individual cells is plotted with respect to their incubation time. The heterogeneity is typical for single-cell experiments. For a better overview, the median values are presented in panel b).

number of nanoparticles in contact with each cell is equal to the height of the bar. The light blue part of the bars corresponds to the number of particles in the e-membrane whereas the dark blue portion represents the counting of internalized ones. The data reveals that in average, taken from median values, 71 $\text{Cy3-SiO}_2\text{-80}$ nanoparticless were in contact which each cell. We use the median and not the mean value as our dataset is very heterogeneous. In such cases the median value gives a better representation of the sample than the mean value. The big heterogeneity is typical for single-cell measurements and represents the diversity within the sample. Despite the diversity, it is apparent that the fraction of nanoparticles within the e-membrane region (light blue) decreases with time in comparison to the number of nanoparticles found inside the cell (dark blue). To gain a closer insight into these differences, we plotted the fraction of internalized particles (see Equation 6.1.5), which was automatically calculated by Nano_In_Cell_3D, against time (6.9 a).

The fraction of nanoparticles that are taken up by the cells at given time points after incubation are shown as gray circles. We found that after 1:15 h:min about 26% and after 2:45 h:min 50% of particles were taken up. This number increases constantly, reaching 92% after 5:45h (see median values, Figure 6.9 b, gray circles).

6.2.4 Validation of Nano_In_Cell_3D by comparison to quenching experiments

In order to validate these results, we compared them to the outcomes of independent quenching experiments designed to determine the uptake of $\text{Cy3-SiO}_2\text{-80}$ into HeLa cells. We thereby analyzed the uptake of the $\text{Cy3-SiO}_2\text{-80}$ nanoparticles by the well-established quenching method [133, 134]. Briefly, the procedure is commonly applied to characterize the uptake of nanoparticles functionalized with a quenchable dye (e.g. Cy3). After the intended incubation time, a cell membrane-impermeable

dye (e.g. trypan blue) is added to the cell culture while monitoring the nanoparticles' fluorescence on a widefield fluorescence microscope. The dye quenches the fluorescence of the nanoparticles that are outside the cell whereas nanoparticles that have been taken up by the cell stay fluorescent. By comparing images prior to and after quenching, the percentage of internalized nanoparticles is accessible.

For the experiments, HeLa cells were grown in Dulbecco's modified Eagle's medium (DMEM; Gibco, Karlsruhe, Germany) supplemented with 10% fetal calf serum (FCS), in 5% CO₂ humidified atmosphere at 37 °C. They were seeded 48 or 24 h before imaging on collagen A Lab-Tek-chambered cover glass (Nunc, Rochester, NY, USA) in a density of $1.0 \cdot 10^4$ or $2.0 \cdot 10^4$ cells/well, respectively. We incubated the cells for 0 to 6 h with the Cy3-SiO₂-80 nanoparticles at a final concentration of 0.12-0.18 mg/mL in CO₂-independent medium (Invitrogen; Karlsruhe, Germany) with 10% FCS and placed on a heated plate (37 °C). The quenching experiments were carried out on a custom-built widefield microscope based on the Nikon Eclipse Ti microscope. Samples were Köhler illuminated through a Nikon Plan APO TIRF 60x/1.45 oil immersion objective with 532 nm laser light with an integration time of 300 ms, exciting Cy3. The fluorescence was separated from the excitation light and image sequences were captured with an electron multiplier charge-coupled device camera (iXon+, Andor Technology, Belfast, UK). Cy3 fluorescence was quenched by adding 10 µl of a 0.4% trypan blue solution into 400 µL medium in the observed chamber during image acquisition.

We determined the fraction of taken up Cy3-SiO₂-80 by this method by analyzing more than 50 individual HeLa cells within a period of 6 hours. Figure 6.9 a (black squares) shows the fraction of taken up nanoparticles at different time points after incubation. Each data point represents an individual cell. For a clearer insight into nanoparticle uptakes, the corresponding median values are shown in Figure 6.9 b as black squares. After approximately 3:00 h:min, 50% of the nanoparticles were taken up by the cells. The wide spread within the data of both experiments is typical for single-cell measurements and represents the heterogeneity from cell to cell. Taking this heterogeneity into account, the datasets obtained by quenching and by spinning disk microscopy in combination with our new analysis method correspond very well and thereby prove that Nano_In_Cell_3D can be successfully used to quantify the uptake of nanoparticles into cells.

6.3 Summary and conclusions

Our newly developed digital method Nano_In_Cell_3D allows analyzing stacks of confocal fluorescence microscopy images of two-color single-cell experiments in a semi-automatic way. It permits a rapid counting of large numbers of nanoparticles that are quantified even when agglomerated. Furthermore, counted nanoparticles can be visualized in great detail, as they are color-coded according to their position with respect to the cell. The processed images, input parameters and results are all saved and can be accessed at any time. As showed by comparative investigation of internalization kinetics of Cy3-SiO₂-80 nanoparticles, the fraction of taken up nanoparticles obtained by employing Nano_In_Cell_3D are in a very good agreement with those assessed by quenching experiments. One major advantage of the proposed method is that no quenchable dye is needed. This leads to an

6 Image analysis by Nano_In_Cell_3D

increased flexibility in the choice of the fluorescent marker. Other advantages when faced to quenching experiments are the reduced need of material and the velocity of analysis. To obtain the fraction of internalized particles by quenching methods, typically one uptake experiment (i.e. one entire cell culture well to analyze only a single cell) has to be carried out per data point. The evaluation by the macro provides the possibility to measure several cells per experiment, resulting in an enhanced collection of data and a reduced consumption of material and time. Nano_In_Cell_3D is therefore optimally suited to study the cellular uptake of fluorescent nano-objects. It overcomes some drawbacks faced by commonly applied methods like flow cytometry and single-cell quenching experiments, offering new possibilities to characterize nanoparticle-cell interactions.

7 SiO₂ nanoparticles and cells

The main goal of this work is to analyze nanoparticle cytotoxicity on a cellular level. We therefore address several aspects of nanoparticle-cell interactions and correlate the findings with observed cytotoxic effects. During our studies, we investigated 310 nm SiO₂ (MPD-SiO₂-310) nanoparticles and their interaction with HUVEC and HeLa cells concerning cellular nanoparticle uptake behavior. Key aspects were the quantification of nanoparticle uptake into individual cells and the uptake pathways. In addition, Dr. Alexander Bauer (AK Prof. S. Schneider, University of Mannheim) investigated the cytotoxic impact of the used nanoparticles onto the cellular systems. Furthermore he compared the outcomes with the cytotoxicity of unlabeled 304 nm SiO₂ (SiO₂-304) nanoparticles in order to probe the influence of the labeling. In the following sections, all datasets are discussed and then correlated to obtain a general picture about the principles governing nano-cytotoxicity. The following chapter is based on the publication “Silica nanoparticles: Nanotoxicity is dependent on the uptake behavior of the cell and therefore cell type dependent”, that was previously submitted to Small [6]. Referring to these data, the deposition behavior of nanoparticles in the given experimental environment was investigated. It was aimed on correlating the uptake of nanoparticles into cells to the number of particles reaching the cells by sedimentation and diffusion. Due to local convection in small parts of the fluid, which could not be avoided due to the experimental conditions, and the therefore very complex interplay between sedimentation, diffusion and convection driven movement of nanoparticles, the analysis of the data exceeds the scope of this work. Nevertheless the data can be found in the Appendix as future experiments aiming in this direction can be compared.

7.1 Nanoparticle characterization

We investigated the nanoparticle-cell interactions applying perylene-labeled (MPD-SiO₂-310) and unlabeled (SiO₂-304) silica nanoparticle species. By comparing labeled SiO₂ nanoparticles to unlabeled ones we were able to unravel the mechanism of nanoparticle uptake applying fluorescence-based techniques while ensuring that the label did not influence the nanoparticle-cell interactions. Nanoparticle sizes were determined by transmission electron microscopy (TEM) and dynamic light scattering (DLS) showing that the particles had average sizes of 310 ± 37 nm (TEM) / 411 ± 12 nm (DLS) (MPD-SiO₂-310) and 304 ± 16 nm / 350 ± 5 nm (DLS) (SiO₂-304). The size measured by DLS exceeds the size obtained by TEM, as by DLS the hydrodynamic radius of the sample is accessed whereas TEM measures the real size. The strong discrepancy in size observable for the labeled nanoparticle species (MPD-SiO₂-310) could be due to the dye interfering with the DLS measurement and thereby leading to false values. We therefore only used the size obtained by TEM. In addition, we determined the zeta potential of both nanoparticle types in cell medium,

7 SiO₂ nanoparticles and cells

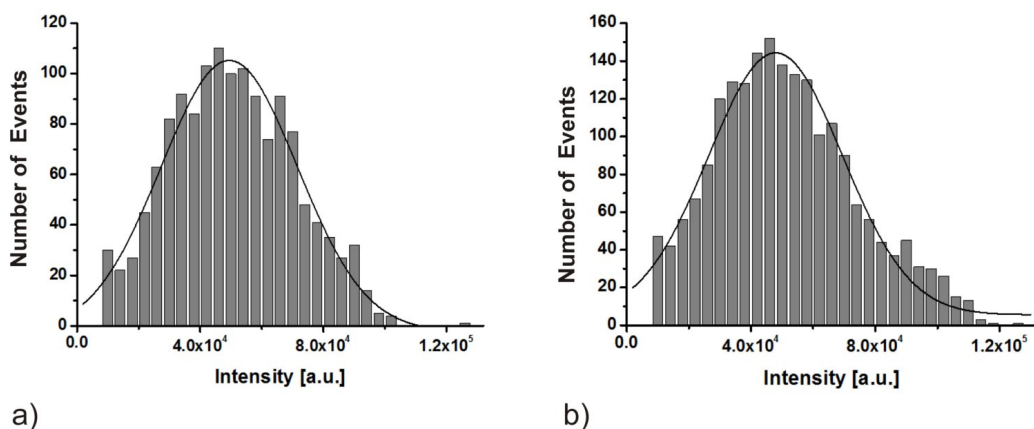


Figure 7.1: Fluorescence intensity distribution of individual MPD-SiO₂-310 showing a gaussian distribution with a mean value of a) 49430 (HUVEC) and b) 48090 (HeLa) counts per nanoparticle.

with values of -14.1 ± 1.5 mV (MPD-SiO₂-310) and -17.1 ± 1.3 mV (SiO₂-304). We determined the mean fluorescence intensity of a single nanoparticle by spinning disk microscopy in combination with the custom-made digital analysis method Nano_In_Cell_3D. To mount the silica nanoparticles on a cover slip we used SecureSealTM Imaging Spacers (Grace Bio-Labs; USA). Thin chambers of 120 μ m were assembled and 50 μ L of Poly-L-Lysine 0.1% solution (Sigma-Aldrich; Germany) were applied to each of them. After 5 minutes the solution was removed with a pipette and left to dry. A MPD-SiO₂-310 solution of 80 μ g/mL in ethanol was prepared and sonicated for 10 minutes. 5 μ L of this solution were applied onto the chambered and treated cover slips. After solvent evaporation samples were mounted with cell culture medium and sealed on a microscope slide by using the adhesive surface of the spacers.

As shown in figure 7.1, the intensities of MPD-SiO₂-310 showed a gaussian distribution with a mean value of 48090 counts per nanoparticle for HeLa cells and 49430 counts per nanoparticle for HUVEC. The differences in intensity probably arise from the different cell media used for HUVEC and HeLa cells.

7.2 Quantification of cellular nanoparticle uptake

One major factor governing nanoparticle cytotoxicity is the uptake of nanoparticles into cells. Once inside the cytoplasm, a variety of interactions between particles and cellular components, including denaturation of proteins or oxidative stress, are possible. For details see Section 2.2.2. For the quantification of nanoparticle uptake, cells were seeded 24 or 48 h prior to the experiments into μ -slides (8 well, Ibidi, Germany) in a density of $1.0 \cdot 10^4$ or $2.0 \cdot 10^4$ (HeLa) and $0.5 \cdot 10^4$ or $1.0 \cdot 10^4$ (HUVEC) cells per well in Dulbecco's modified Eagle's medium (DMEM; Gibco, Karlsruhe, Germany) supplemented with 10% fetal calf serum (FCS) (HeLa) or in Endothelial Cell Growth

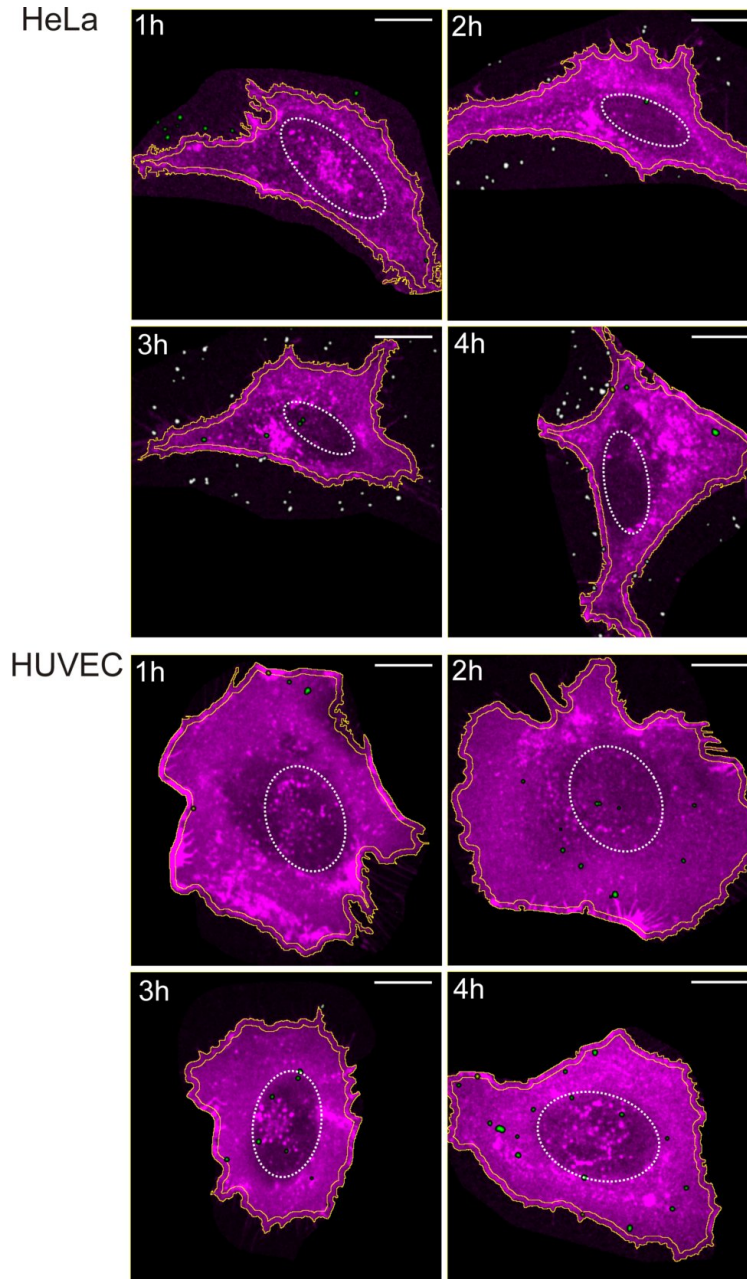


Figure 7.2: Fluorescent confocal cross sections of HeLa cells (top) and HUVEC (below) after 1 - 4 h incubation time with MPD-SiO₂-310. The magenta region corresponds to the cell, the cell membrane region as considered during the evaluation process is enclosed between the two yellow lines. Nanoparticles within the cytoplasm are color coded in green, yellow nanoparticles are localized within the cell membrane region. White particles are outside the cell and not considered during evaluation. The position of the nuclei are depicted as dotted white ellipses. As confocal cross sections are shown, a staining or nanoparticle within the dotted circle does not mean that nanoparticles or cell membrane stain have been taken up into the nucleus but that a confocal plane below the nucleus was selected. Only nanoparticles present in the depicted confocal cross section are highlighted, therefore nanoparticle numbers visible are less than counted within the whole volume of the cells. But still, the increasing number of nanoparticles per cell with increasing time and the higher nanoparticle uptake of HUVEC compared to HeLa cells is clearly visible. For the evaluation process, the region around the target cells were selected by hand, resulting in black backgrounds in the images. The scale bar is 20 μm .

7 SiO₂ nanoparticles and cells

Medium with Supplement Mix (PromoCell, Heidelberg, Germany).

For nanoparticle preparation, the required amount of nanoparticles was added to the cell medium. The dispersion was vortexed for 10 seconds and then treated with ultrasound for 10 minutes. It was again vortexed for 10 seconds and added to the cells. The cells were incubated with the nanoparticles at 37 °C at a concentration corresponding to the second highest concentration used for the assessment of cytotoxicity, namely $3.0 \cdot 10^4$ nanoparticles/cell. After the incubation, the cell membrane was stained with Cell Mask Deep Red (Invitrogen; Karlsruhe, Germany) and cells were transferred into CO₂-independent medium (Invitrogen; Karlsruhe, Germany) with 10% FCS. Restaining was performed during the experiment when necessary. During the imaging, physiological temperature was achieved by a heated microscopy stage (37 °C). Stacks of confocal cross-sections with an interslice distance of 190 nm of individual cells were obtained by spinning disk microscopy with alternating excitation (488 nm and 639 nm, 100 ms each), exciting perylene and the cell membrane stain, respectively. To reduce self fluorescence, each cell was treated with intense 488 nm laser light prior to imaging. However, we took care that the bleaching did not affect cellular viability for the time of the experiment.

Representative examples of the obtained confocal images are shown in Figure 7.2 for both cell types. The images depict one confocal cross-section taken from one cell each. The magenta staining originates from the cell membrane stain which has been taken up into the cells during the experiment. The cell membrane region, as considered during the evaluation process is equal to the section between the two yellow lines. Nanoparticles (green) are clearly localized within the cellular boundaries showing their uptake into the cytoplasm. Additional nanoparticles (yellow) are present in the cell membrane region. White particles are localized outside the cell and therefore not considered. The position of the nucleus is shown as a dotted white ellipse. As confocal cross sections are shown, a staining within the dotted white ellipses does not mean that dye or nanoparticles were taken up into the nucleus, but that a cross section below the nucleus was selected. The nanoparticles were distributed more or less regularly throughout the cell for both cell types. A previous study on the same particle type showed that the particles are mainly localized in the perinuclear region after 24h [68]. This is in good agreement with another study pointing out that 50-200 nm latex beads get accumulated in the perinuclear region whereas 500 nm beads were localized at the periphery of the cell [146].

The number of nanoparticles present in the cytoplasm varies from cell to cell. We quantified the nanoparticles inside the cytoplasm and in the enlarged membrane region by the ImageJ plugin `Nano_In_Cell_3D` (for details see Chapter 6).

The absolute numbers of time dependent nanoparticle distribution in the individual HUVEC and HeLa cells is shown as a Histogram in Figure 7.3. In total, more than 120 cells of each cell type were analyzed for incubation times of 1 to 4 hours. Each histogram represents one cell type. The inset in the left graph shows a rescale of the HeLa dataset. The total height of each bar corresponds to the mean number of nanoparticles that is in contact with each cell. It is equal to the sum of nanoparticles that have been taken up into the cytoplasm (dark gray bar) and the number of particles in the membrane region (light gray bar). Both cell types show a time-dependent increase of

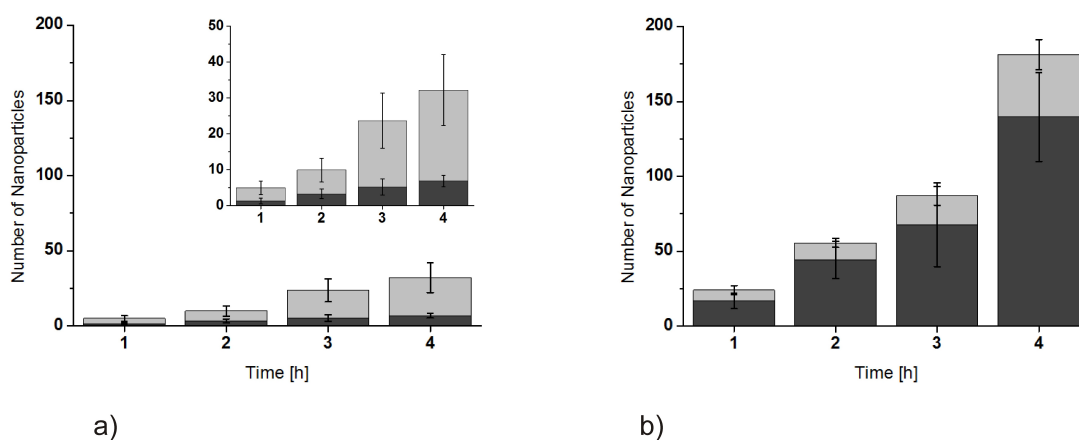


Figure 7.3: Uptake behavior of MPD-SiO₂-310 in a) HeLa cells and b) HUVEC. The histograms depict the mean number of MPD-SiO₂-310 in contact with single cells as the full height of the bars. The inset in a) shows a rescale of the first graph. The dark gray region represents the number of nanoparticles present inside the cytoplasm whereas the light gray fraction corresponds to particles that are present in the cell membrane region. The cells are sorted according to their incubation time. For both cell types, the absolute number of nanoparticles taken up into the cells and the number of particles in the cell membrane region increases with time. After 4 h a mean value of 7 nanoparticles have been taken up by HeLa cells whereas HUVEC incorporated an average number of 140 nanoparticles in the same time period. The error bar represents the standard error of the mean.

nanoparticle numbers incorporated into the cell and into the cell membrane region. It is remarkable that HUVEC take up much more of the provided nanoparticles than HeLa cells. After 4 h only 7 nanoparticles, in average, have been taken up into the cellular boundaries of HeLa cells whereas HUVEC incorporated an average number of 140 nanoparticles in the same period. In addition, the mean number of particles present in the membrane region of HUVEC strongly exceeds the amount of nanoparticles in the cell membrane region of HeLa cells.

Most likely, these differences originate from varieties in the cellular characteristics. Each cell type has an individual surface property and cellular morphology [147, 148]. These parameters strongly influence nanoparticle-cell interactions and therefore the nanoparticle uptake behavior. Possibly, the nanoparticles attach stronger to HUVEC than HeLa cells leading to an increased nanoparticle number interacting with the cells as nanoparticles have a higher probability to get stuck on the surface.

7.3 Uptake pathways

In the previous section, we proved that HUVEC are more active in nanoparticle uptake than HeLa cells. This could either be due to differences in the cellular metabolism or be caused by different uptake pathways [146]. The uptake pathways applied by nanoparticles have major influence on their intracellular distribution. Depending on the uptake pathway, nanoparticles are exposed to different

7 SiO₂ nanoparticles and cells

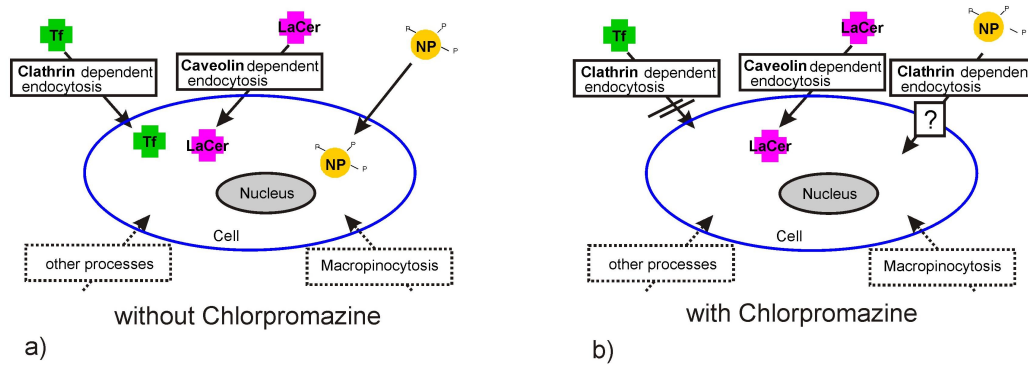


Figure 7.4: Scheme of the inhibitor experiments applied to probe the dependency of nanoparticle uptake on the clathrin mediated endocytosis. a) In absence of the inhibitor all uptake pathways are functional as can be probed by cellular markers like transferrin (Tf, clathrin-dependent pathway) or lactosylceramid (LaCer, caveolin dependent pathway). In addition, nanoparticles (yellow) are taken up into the cellular boundaries (blue). b) The inhibitor chlorpromazine blocks the clathrin mediated pathway, leading to an inhibition of transferrin uptake. Other pathways stay active, as indicated by the uptake of lactosylceramide. The behavior of the nanoparticles in presence of the inhibitor allows conclusions about their uptake pathway.

sets of proteins or enzymes which can attach to their surface. This protein corona influences the further fate of the particles [35]. Furthermore, depending on the uptake pathways, the nanoparticles are exposed to changing pH values which might lead to ion release or particle decomposition [49]. We identified the uptake route used by the SiO₂ nanoparticles by inhibitor experiments. Endocytic inhibitors are drugs which specifically block individual cellular uptake pathways [100, 149–151]. During our studies we used three different inhibitors: chlorpromazine, cytochalasin D and nocodazole. Chlorpromazine is a cationic amphiphilic drug which is known to block the clathrin mediated pathway. It reversibly translocates clathrin and its adapter proteins from the cell surface to intracellular vesicles [149, 152] and thereby prevents the formation of clathrin coated pits. Both cytochalasin D and nocodazole are inhibitors that depolymerize parts of the cytoskeleton. Cytochalasin D disrupts actin filaments by inducing ATP hydrolysis in actin subunits. Thereby the concentration of actin containing ADP is increased with respect to ATP containing subunits, leading to an accumulation of ADP containing actin monomers. As ADP-actin has a higher critical concentration for polymerization as ATP-actin, less actin filament polymerization takes place leading to the disruption of existing filaments [153]. The drug nocodazole depolymerizes the microtubule network by stimulating the hydrolysis of GTP in tubulin monomers and thereby leading to incorporation of GDP-tubulin into the filaments. As GDP-tubulin has a lower affinity to polymerize as GTP-tubulin, the polymerization of the filament is slowed down [154].

7.3.1 Clathrin mediated endocytosis

The basic principle of the experiments carried out to probe the nanoparticle uptake in dependency on the clathrin mediated pathway by applying the drug chlorpromazine is visualized in Figure 7.4.

In absence of the inhibiting drug (Figure 7.4a), all uptake processes of the cell are functional. E.g. the glycoprotein transferrin (Tf), shown in green, is specifically taken up via the clathrin-dependent pathway whereas the sphingolipid lactosylceramide (LaCer), shown in magenta, can be used as marker for caveolin-mediated endocytosis [87, 149]. In presence of the drug (Figure 7.4b), the uptake of Tf is inhibited, as indicated by the crossed out arrow, whereas LaCer can still enter the cell. This indicates that the clathrin-mediated pathway is successfully inhibited whereas other processes are still functional. The uptake behavior of the SiO₂ nanoparticles (yellow) gives information about their uptake pathway. The functionality of the single pathways can be verified via fluorescence microscopy by using dye-labeled substrates showing a high affinity towards the individual processes.

For these experiments, cells were seeded on collagen A or polylysine L-coated Lab-Tek-chambered cover slides (NUC, Rochester, NY, USA) in a density of $1.0 \cdot 10^4$ or $2.0 \cdot 10^4$ (HeLa) and $2.0 \cdot 10^4$ (HUVEC) cells per well 24 h or 48 h prior to imaging in Dulbecco's modified Eagle's medium (DMEM; Gibco, Karlsruhe, Germany) supplemented with 10% fetal calf serum (FCS) (HeLa) or in Endothelial Cell Growth Medium with Supplement Mix (PromoCell, Heidelberg, Germany) (HUVEC). For inhibition experiments, the cells were preincubated with the inhibitors for 30 min at 37 °C in 5% CO₂ humidified atmosphere before addition of further substrates. We used labeled transferrin or lactosylceramide to probe the functionality of the individual pathways. Before the imaging, the cell membranes were stained, if required, and the HeLa cells were transferred to CO₂ independent medium (Invitrogen; Karlsruhe, Germany) with 10% FCS and the appropriate inhibitor concentration. The uptake of transferrin, lactosylceramide and nanoparticles was monitored by confocal spinning disk microscopy.

Figure 7.5 shows representative images acquired during the individual experiments. At first, we verified that clathrin- as well as caveolin-mediated endocytosis are active in HUVEC and HeLa cells. We therefore incubated both cell lines with the corresponding markers. Both lactosylceramide and transferrin are clearly visible within the cellular boundaries of HUVEC and HeLa cells after 30 minutes of incubation (see Figure 7.5 a, b, g, h) proving the uptake of both substrates and therefore the activity of both pathways. In the following experiments, we investigated the cellular uptake in presence of the inhibitor chlorpromazine which blocks the clathrin dependent pathway. For reliable inhibitor experiment, we needed to adjust the inhibitor concentrations from literature values [150, 151] in order to ensure that only this specific pathway is blocked whereas other pathways retain their functionality. This means that in the presence of the inhibitor, the uptake of transferrin is stopped (Figure 7.5 d, j) whereas lactosylceramid, the marker for caveolin-dependent endocytosis can still be found inside the cytoplasm (Figure 7.5 e, k). We ensured cell viability at the chosen concentration by dead cell staining assays for both cell types. We found that the cells are viable at the given concentration. The distinct round shape of inhibitor treated HUVEC is probably due to cell-inhibitor interactions, as is also indicated in literature [149] which lead to a loss in cell-substrate linkage. Finally we chose 15 µg/mL CP for HeLa cells and 7.5 µg/mL CP for HUVEC as for these concentrations the previously mentioned requirements were fulfilled. In the next set of experiments we probed the dependency of nanoparticle uptake on the clathrin-mediated pathway. From previous experiments (see Section 7.2) we know, that the particles are taken up in absence of the inhibitor.

7 SiO₂ nanoparticles and cells

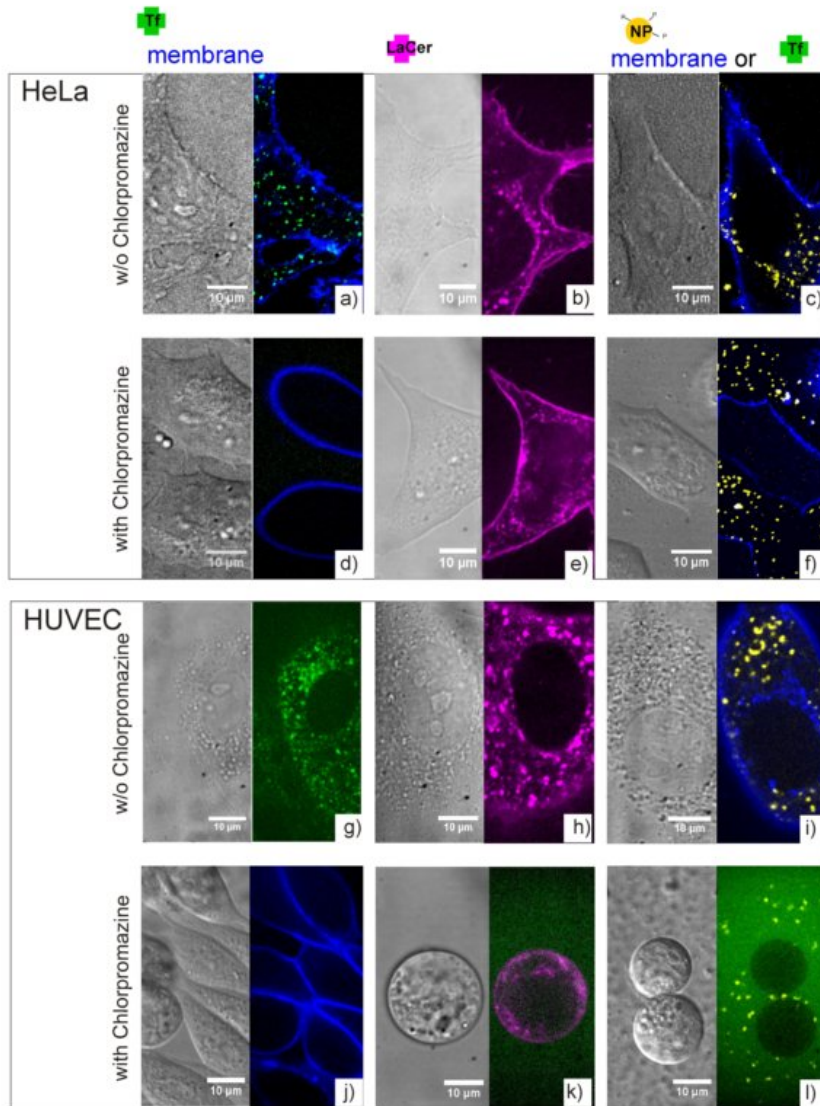


Figure 7.5: Uptake of Transferrin (Tf, green), Lactosylceramide (LaCer, magenta) and SiO₂ nanoparticles (yellow) in absence (a-c) and presence (d-f) of the inhibitor Chlorpromazine (CP) into HeLa cells as well as in absence of CP (g-i) and in presence (j-l) of the inhibitor CP into HUVEC. The cellular membrane is shown in blue. The images reveal that in absence of Chlorpromazine Tf (a,g), LaCer (b,h) and nanoparticles (c,i) are taken up by the cells. The inhibition of the clathrin-mediated endocytosis by Chlorpromazine does not affect the LaCer uptake (e, k) whereas the uptake of Tf (d, j) and nanoparticles (f, l) is suppressed in HUVEC and HeLa cells, indicating their dependence on the clathrin-mediated pathway.

As can be seen in Figure 7.5 c, i, the nanoparticles (yellow) are clearly detectable within the cellular borders (blue) after 1h (HUVEC) and 4h (HeLa) incubation time. We then repeated the experiments in presence of the inhibitor chlorpromazine. For the HeLa cells, the cellular membrane was stained prior to confocal imaging. Figure 7.5 f, shows that no nanoparticles (yellow) are visible within the region enclosed by the cell membrane (blue) indicating that the nanoparticle's uptake is blocked and the nanoparticles are thus mainly taken up via the clathrin mediated pathway in HeLa cells. As HUVEC cells loose their substrate connection due to the inhibition, and are washed away during membrane staining, we decided to use transferrin to mark the extracellular space (see Figure 7.5 l). The marker transferrin (green) was not taken up into the cell, indicating an effective inhibition of the clathrin-mediated pathway and leading to a staining of the extracellular space. Nanoparticles (yellow) are only present in the extracellular space and are not taken up into the HUVEC cells. We therefore conclude that the MPD-SiO₂-310 nanoparticles are probably predominantly taken up via the clathrin-dependent pathway in both cell types.

These findings are consistent with recent studies showing nanoparticle uptake via clathrin mediated endocytosis for several cell types and thus supporting our results. For example, 500 nm sized silica particles are taken up via clathrin-dependent endocytosis and macropinocytosis in dermal fibroblasts [155], 200 nm fluorescent microspheres are taken up via clathrin dependent endocytosis by B16-F10 cells [146], and monodisperse hydrogel particles with a size of 150 nm and 200 nm are taken up via the clathrin mediated pathway in HeLa cells [156]. Nevertheless, the results can not be generalized for all particles as in this size range and each nanoparticle-cell combination as to be investigated individually, as e.g. 500 nm fluorescent microspheres were taken up by clathrin-independent processes in B16-F10 cells [146].

7.3.2 Dependency of nanoparticle uptake on the actin and tubulin networks

Moreover, we were interested if actin filaments or microtubules play a role in the uptake of SiO₂ nanoparticles into HeLa cells. One main function of actin filaments is to provide a framework supporting the plasma membrane. Actin filaments therefore determine the shape of the cell [157]. Its role in endocytic pathways is still discussed. In addition to other functions the actin cytoskeleton might have an influence on phagocytosis, macropinocytosis as well as clathrin- dependent and independent processes (for details see Section 4). The microtubule network spans the cell from the nucleus to the cell membrane. Beside other functions, it serves as track for the motor protein mediated transport of membrane vesicles [157] and is therefore responsible for the active transport of endosomes.

We disrupted both actin filaments or microtubules by preincubating the cells with cytochalasin D (5 µg/mL [150]) or nocodazole (10 µg/mL [146, 150]) for 30 minutes in subsequent experiments. Following the initial inhibition, nanoparticles were added and coincubated with the cells in presence of the inhibitor for further 4 h. After the incubation, the cell membrane was stained and the cells were monitored by confocal spinning disk microscopy. The disruption of microtubules by nocodazole does not influence the cellular uptake of nanoparticles as is indicated by confocal images (see Figure 7.6 b) where nanoparticles (yellow) are clearly present within the cellular borders (blue). The

images are very similar to images obtained from not-inhibited cells (see Figure 7.6 a). In contrary, the disruption of the actin network inhibits the nanoparticle uptake (see Figure 7.6 c). This is in good agreement with recent publications showing that the internalization of silicon nanoparticles (1600 nm and 3200 nm) and negatively charged polystyrene particles (113 nm) is actin-dependent in HeLa cells [150]. In contrary, the disruption of microtubules did not affect the uptake of negatively charged polystyrene particles [150]. Another report showed that microtubule disruption affects latex bead internalization and processing in a size-dependent manner. Small particles, in a size range of 50-200 nm were accumulated near the plasma membrane while the intracellular distribution of 500 nm particles remained unchanged. In addition, microtubule disruption reduced the uptake of 50 and 100 nm particles by more than 50% whereas 200 nm particles uptake was only reduced by 25% [146]. Our results indicate that the actin cytoskeleton is actively involved in nanoparticle uptake whereas microtubules contribute to the further distribution of cargo inside the cell. Furthermore, actin is probably involved in clathrin dependent endocytosis [101] thus supporting our result that the nanoparticles are mainly taken up by the clathrin dependent pathway.

7.4 Correlation of nanoparticle uptake to cytotoxicity

The data presented in the following section was acquired by Dr. Alexander Bauer, (AK Prof. S. W. Schneider, University of Mannheim). In order to complete the comparison of nanoparticle-cell interactions on HUVEC and HeLa cells, it is included into this work.

We analyzed the cytotoxic response of both HUVEC and HeLa cells to silica nanoparticles by investigating the mitochondrial activity (MTT assay), the membrane leakage (LDH assay) and cell death. To ensure that the perylene molecules labeling MPD-SiO₂-310 do not influence the result, we additionally investigated the cytotoxic response to similar unlabeled particles SiO₂-304.

7.4.1 Dose-dependent cytotoxicity of silica nanoparticles

HeLa cells were grown in Dulbecco's modified Eagle's medium (DMEM; Gibco, Karlsruhe, Germany) supplemented with 10% fetal calf serum (FCS), at 37 °C in 5% CO₂-humidified atmosphere. HUVEC were isolated using collagenase and were grown in Endothelial Cell Growth Medium (PromoCell, Heidelberg, Germany) supplemented with 10% heat inactivated fetal calf serum (FCS), 5 U/mL heparin (Biochrom, Berlin, Germany), 1% penicillin and streptomycin, and 1% growth supplement derived from bovine retina. Cells were maintained with 5% CO₂ at 37 °C and cultivated maximally up to the third passage. HUVEC and HeLa cells were exposed to different concentrations (1000 nanoparticles/cell; 15000 nanoparticles/cell; 30000 nanoparticles/cell, 60000 nanoparticles/cell) of MPD-SiO₂-310 and SiO₂-304 particles for 24 h. After exposure to the SiO₂ nanoparticles, 100 μ L of the medium was removed and mitochondrial activity of the cells was measured by the 3-(4,5-dimethylthiazol-2-yl)-2,5-diphenyltetrazolium bromide (MTT) reduction assay [158]. Cytotoxicity was calculated from the absorbances at 570 nm and expressed as relative values compared with untreated negative controls. Membrane damage was quantified by the cellular level of lactate dehydrogenase in the removed supernatant [159] using LDH assay kit (Roche, Mannheim, Germany). The

7.4 Correlation of nanoparticle uptake to cytotoxicity

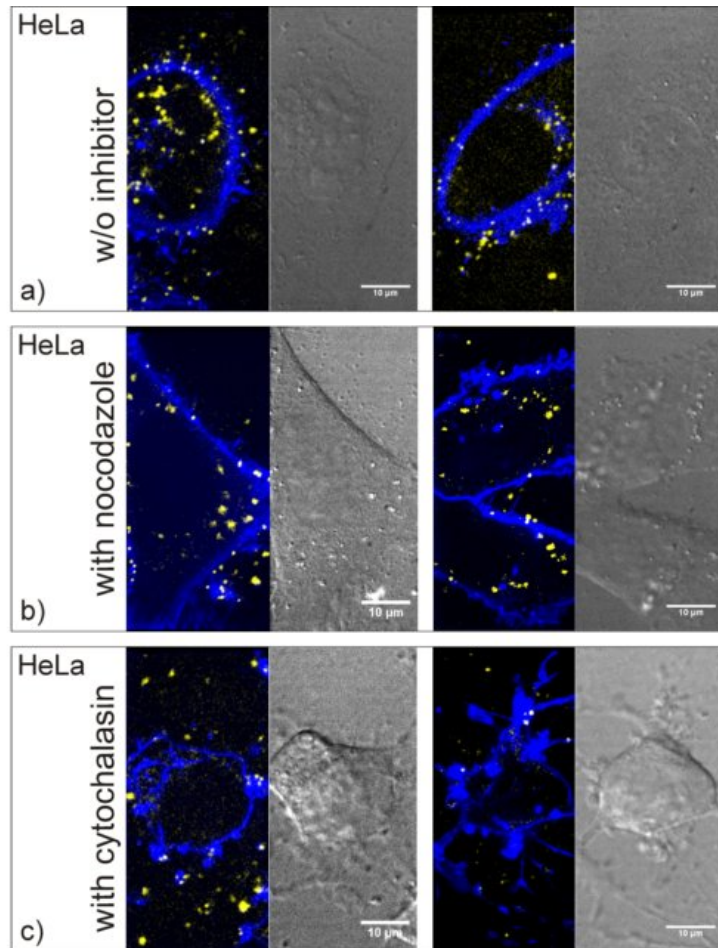


Figure 7.6: Cellular confocal cross-sections (colored) and DIC images (gray) which showing the uptake of nanoparticles (yellow) in absence and presence of the inhibitors Cytochalasin D and Nocodazole. a) Nanoparticles are taken up by HeLa cells in absence of the inhibitor as they can be localized within the cellular borders (blue). b) The depolymerization of microtubules via nocodazole has no influence the cellular uptake behavior whereas c) the depolymerization of actin filaments inhibits nanoparticle uptake. We therefore conclude that the uptake of MPD-SiO₂-310 nanoparticles is dependent on actin filaments but not microtubules.

7 SiO₂ nanoparticles and cells

absorbances of the supernatant were measured at 490 nm by using Synergy 2 multi-mode microplate Reader (BioTek, Winooski, USA) and results are presented as relative values compared to control. As shown in Figure 7.7, mitochondrial activity decreased significantly as a function of dosage levels in HUVEC (Figure 7.7 a). When compared to the control (dashed line), the metabolic activity was not significantly changed after exposure to 1000 nanoparticles/cell for 24 h. In contrast, mitochondrial activity was reduced by more than 35% upon incubation with nanoparticles at concentrations of 15000 nanoparticles/cell and further decreased gradually at doses of 30000 nanoparticles/cell and 60000 nanoparticles/cell after exposure of 24 h. Interestingly this effect strongly correlated with an elevated LDH release due to membrane leakage and is, therefore, indicative for a reduced cell viability (Figure 7.7 b). Based on the dose-dependent studies, a concentration of 1000 nanoparticles/cell showed a significant reduction of the MTT value in HeLa cells (Figure 7.7 c). Furthermore, a dosage of 15000 nanoparticles/cell resulted in a reduced mitochondrial activity by more than 30%, comparable to the observation in HUVEC, whereas a higher concentration of SiO₂ particles induced no enhanced effects on metabolic activity. However, the cells showed no signs of membrane damage in all particle concentrations if compared to the control group (Figure 7.7 d). Therefore, MTT and LDH assays revealed a different extent of nanoparticle-induced cytotoxicity in HUVEC versus HeLa cells. The differences in cytotoxicity caused by the nanoparticles may arise from deviations in metabolism and cell proliferation in both cell types [67]. In this context it has been shown that ultrafine silica influence cell viability of human endothelial cells [58]. It is interesting to see that as HUVEC take up the MPD-SiO₂-310 particles more efficiently than HeLa cells (Figure 7.3) the amount of intracellular particles correlates with the observed cytotoxicity [160].

7.4.2 Influence of the perylene-surface functionalization on the toxicity of silica nanoparticles

To analyze cellular uptake and subcellular localization in different cell types, fluorochrome (perylene)-labeled silica nanoparticles were used. As the toxicity of nanomaterials may depend on factors such as chemical composition and surface [67, 161] we compared cytotoxic effects of unlabeled (SiO₂-304) and fluorescent-labeled (MPD-SiO₂-310) nanoparticles. In our case, the MTT (Figure 7.7 a, c) and LDH data (Figure 7.7 b, d) were not significantly different. Therefore we concluded that the surface functionalized with perylene does not affect cytotoxicity of the used nanoparticles neither in HUVEC nor in HeLa cells.

7.4.3 Silica nanoparticle-induced cell death

To get further insights into cytotoxicity caused by SiO₂ nanoparticles, cell death was quantified by flow cytometric analysis after DNA staining with propidium iodide (Figure 7.8). Quantification of fluorescence allows to distinguish between living and dead cells, as cell death correlates with the exclusion of parts of the labeled DNA. As the labeling of the silica nanoparticles with perylene may interfere with the propidium iodide used in this assay, nanoparticle-induced cell death was quantified after exposure to the unlabeled SiO₂-304. Flow cytometric analysis of DNA content was performed

7.4 Correlation of nanoparticle uptake to cytotoxicity

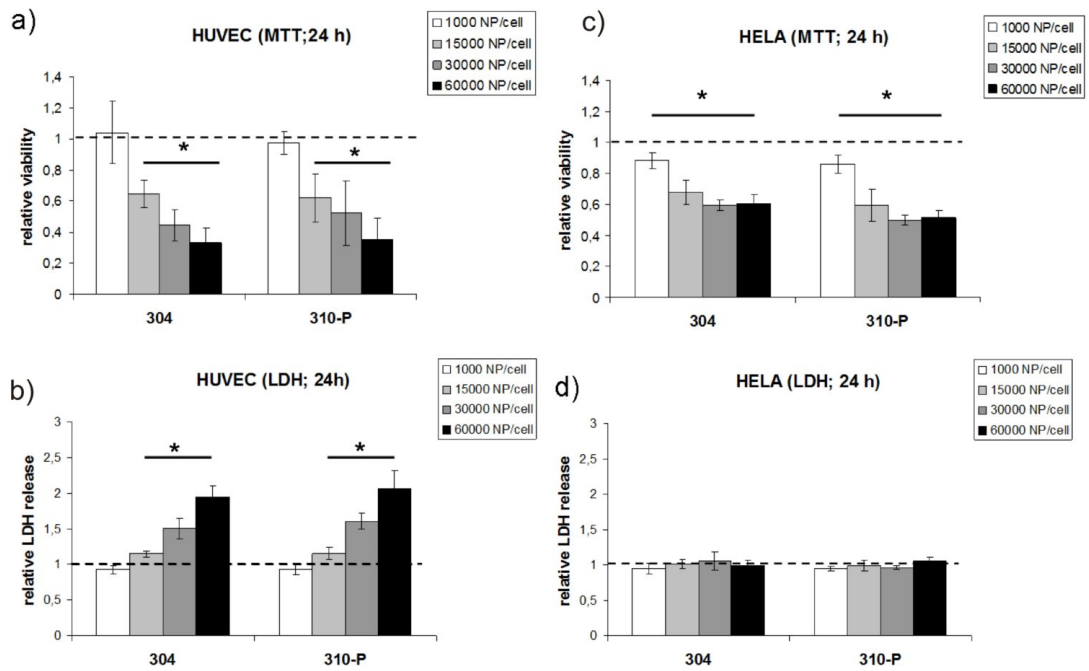


Figure 7.7: Cytotoxic effects of unlabeled silica nanoparticles (SiO_2 -304) and perylene-labeled SiO_2 nanoparticles (MPD- SiO_2 -310) on HUVEC and HeLa cells were analyzed by MTT and LDH measurements. Quantitative analysis revealed a strong correlation between a) reduced metabolic activity and b) membrane damage followed by LDH release in HUVEC. c) Mitochondrial activity in HeLa cells decreased within the first 24 h of exposure d) without showing altered membrane leakage compared to the control (dashed line). Particles with modified surface (MPD- SiO_2 -310) showed no different toxicity compared to the unlabeled controls (SiO_2 -304). Data represent mean \pm standard deviation from three independent experiments ($n = 6-9$) or with pooled triplicates (* $p < 0.05$).

7 SiO₂ nanoparticles and cells

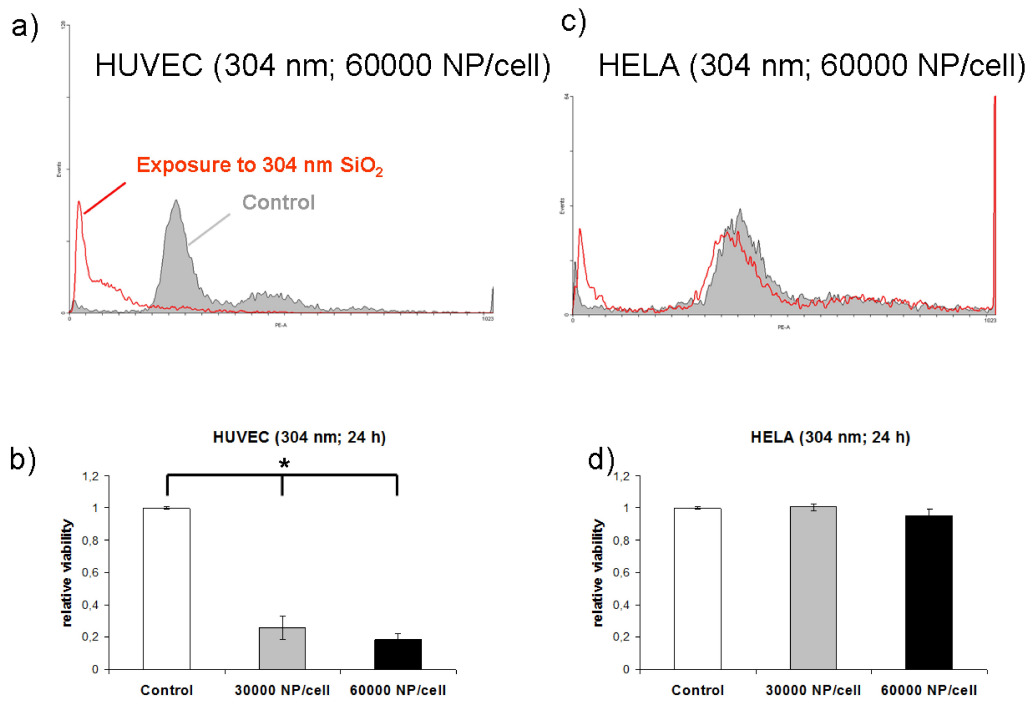


Figure 7.8: HUVEC and HeLa cells were exposed to SiO₂-304 nanoparticles at concentrations of 30000 nanoparticles/cell and 60000 nanoparticles/cell for 24 h. Cell viability was assessed by propidium iodide (PI) staining. a) FACS analysis and b) quantitative analysis showed a significantly reduced cell viability of HUVEC after exposure to nanoparticles. c, d) In contrast, HeLa cells showed no signs of cell death neither after exposure to 30000 nanoparticles/cell nor after 60000 nanoparticles/cell. Results represent the means of two independent experiments (n = 2-5) and error bars represent the standard error of the mean (* p < 0.05).

using propidium iodide (PI) staining. After exposure to 30000 and 60000 nanoparticles/cell for 24 h, HUVEC and HeLa cells were harvested with accutase (PAA, Pasching, Austria), washed with PBS and permeabilized with 70% ethanol for 1 h at 4 °C. The cells were then centrifuged, washed with PBS and re-suspended in 50 µg/mL PI for 5 min. Cells were analyzed using FACS SLR II and Diva Software. The percentage of dead cells was quantified with WinMDI software. In line with our MTT and LDH results, the rate of viable cells in HUVEC after exposure to 30000 nanoparticles/cell for 24 h was significantly reduced to $25.90\% \pm 0,07\%$ compared to the untreated control group. Living endothelial cells treated with 60000 nanoparticles/cell further decreased to $18.33\% \pm 0.04\%$ (Figure 7.8 a, b). In contrast to the HUVEC, SiO₂-304 showed no effect on the viability of HeLa cells neither after incubation with 30000 nanoparticles/cell nor with 60000 nanoparticles/cell (Figure 7.8 c, d). Quantitative analysis revealed a relative viability of 1.01 ± 0.02 for exposure to 30000 nanoparticles/cell and 0.95 ± 0.04 after incubation with 60000 nanoparticles/cell (Figure 7.8 d). These findings are in accordance with LDH assays showing no differences in membrane leakage compared to control (Figure 7.8 d). Thus, treatment with SiO₂-304 is associated with cell death of HUVEC, whereas an effect on the viability of HeLa cells can be excluded. These results are in agreement with those obtained from an earlier report, where a reduction of viability was observed in different cell types after incubation with amorphous silica [67]. By contrast, nanoparticles caused less cytotoxicity in different tumor cell lines in the same study. Silica nanoparticle-induced cell death has been also reported for different cell types [162]. In this context we could show in a previous study that cytotoxicity of SiO₂ nanoparticles lead to the induction of necrotic processes in HUVEC and not apoptosis [68].

7.5 Summary and conclusions

In summary, the current toxicological study clearly indicates that the cytotoxic impact of SiO₂ nanoparticles correlates with the metabolic activity and the amount of nanoparticle uptake into HUVEC and HeLa cells. We showed that the intracellular uptake and accumulation of labeled silica nanoparticles was approximately 20 times as efficient in HUVEC compared to HeLa cells. In both cell types clathrin-mediated endocytosis seemed to be the predominant pathway for the uptake of the nanoparticles as was shown by experiments with specific inhibitors. Interestingly, the differences in amount of nanoparticle uptake were reflected in the cytotoxic response of HUVEC and HeLa cells to the nanoparticles. While mitochondrial activity and membrane leakage was affected in the endothelial cells, silica particles induced no alterations in the membrane permeability of the tumor cells. With these experiments we were also able to show that the surface functionalization with perylene of the silica nanoparticles did not introduce an artificial effect altering the nanoparticle-cell interactions. FACS analysis demonstrated nanoparticle-induced cell death in HUVEC, whereas the viability of HeLa cells was unaffected. The results clearly show that cytotoxic effects of nanoparticles can not be generalized and transferred from one cell type to another. In the current state of knowledge about nanotoxicity, it is inevitable to access the data for each cell type of interest experimentally. Therefore, it is important to analyze human cells with physiological relevance and to compare the

7 SiO_2 nanoparticles and cells

interactions of defined nanoparticles with different cell types in order to predict the potential toxicity effects of nanoparticles on humans.

8 Microfluidic system

All experiments described in the previous sections were carried out applying static standard cell culture conditions. Nevertheless, in real life, HUVEC grow on the inner surface of blood vessel where they are constantly exposed to shear forces from the blood flow. In a next step, to further approach in-vivo conditions, a microfluidic system will be used to mimic the blood flow during the experiments. The microfluidic system used in this work was developed and provided by Prof. A. Wixforth (University of Augsburg) and M.F Schneider (Boston University). In the next chapter, the design, working principle and the assembly of the system are described. In addition the system is characterized concerning temperature, flow and evaporation behavior and suggestions to further improve the channels system for live-cell cytotoxicity assessment are made.

8.1 Design and working principle

The microfluidic system which is characterized by its small size allowing the integration of the system into optical microscopes, its flexibility concerning the channel design and its non-invasive pumping technology. It is composed of two major components, the aluminum mount including the piezoelectric chip used for flow generation and the flow chamber (see Figure 8.1 a). The flow chamber is made of the Polydimethylsiloxan (PDMS) and contains a circular channel, the artificial blood vessel. The channel has a width of approx. 1 mm and a depth of approx. 5 mm. On the lower side of the PDMS the channel is closed by a coverglass (see Figure 8.1 b) which allows to visualize the inside of the channel system by fluorescence microscopy. The flow chamber is put, coverglass first, into the mount and the whole mount can be placed onto the widefield fluorescence microscope (see Figure 8.1 c). Due to the geometry of the microfluidic system, only the middle part of the PDMS block with the channel is accessible for the objective and can be investigated by fluorescence microscopy as is indicated in Figure 8.1 b.

The flow inside the microfluidic system is generated by surface acoustic waves (SAW) working as a nanopump. SAW are generated, when an electrical signal is fed into so-called transducers on the surface of a piezoelectric chip. In our case, the piezoelectric chip is made of LiNbO_3 . The signal is converted into a deformation of the crystal and a mechanical wave is launched across the chip when the right frequency of the signal is applied [163]. The wave is transduced from the piezoelectric chip to the coverglass of the flow chamber by a droplet of immersion oil used to contact the two components. When the SAW reaches the air-liquid boundary at the surface of the substrate, streaming is induced which can lead to a flow of the whole liquid. In Figure 8.2 this process is depicted schematically. At the boundary ($x = 0$), the SAW is absorbed by the fluid as indicated by the decaying amplitude of the blue curve in positive x -direction [163]. By the interaction of the

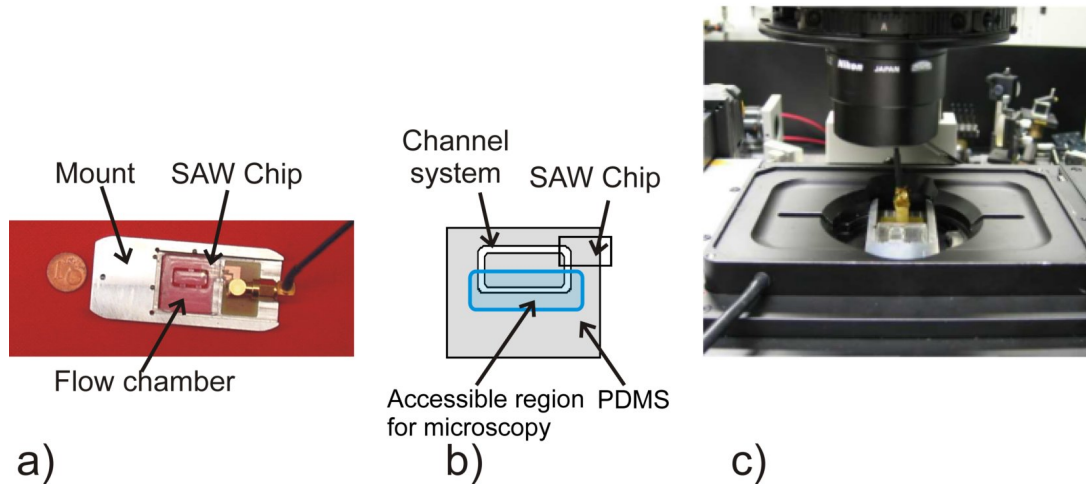


Figure 8.1: a) Photograph of the microfluidic system which is composed of an aluminum mount with the piezoelectric SAW chip and a flow chamber. b) Scheme of the flow chamber made of PDMS which contains the circular channel. The position of the SAW chip and the region accessible for widefield microscopy are shown in addition. c) Photograph of the microfluidic system placed on the widefield microscope.

liquid with the SAW, a sound wave is excited in the liquid. Due to different sound velocities in the liquid and the solid substrate, the wave is launched under a diffraction angle Θ_R and an acoustically induced streaming is generated [163, 164].

8.2 Assembly of the microfluidic system

The PDMS-flow chamber is synthesized with the SYLGARD 184 Silicon Elastomer Kit (DOW Corning). A 1:10 mixture of curing agent and silicon is casted into an aluminum casting mold cleaned with isopropanol. The design of the casting mold determines the geometry of the artificial blood vessel which can therefore easily be redesigned and changed. The filled casting mold is placed into an exsiccator and the vacuum is increased approx. every 5 minutes to remove air bubbles from the gel. When no more air bubbles are emerging, the casting mold is placed for 1 h onto a heating plate at 90°C to harden the polymer. The PDMS is chilled with cold water and carefully removed from the mold.

To clean the coverglasses, they are placed in a 0.5 % Helmanex solution. The beaker glass is covered by parafilm and the fluid is heated to 60°C for 20 min. Afterwards the coverglasses are treated with ultrasound for 3 min within the Helmanex solution. They are removed from beaker glass, rinsed with deionized water and air dried.

The coverglasses are then pressed to the lower side of the PDMS gel and all air bubbles are excluded.

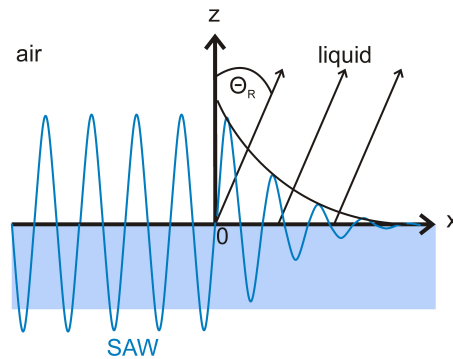


Figure 8.2: Interaction of SAW with a liquid at the surface of the piezoelectric material. The SAW, which is propagating from left to right, hits the liquid at $x = 0$ leading to a longitudinal sound wave that is radiated into the fluid under the refraction angle θ_R . The image is adapted from [163] and [165].

8.3 Characterization and adaption to live-cell imaging requirements

The microfluidic system will be used to mimic blood flow conditions for endothelial cells. For this reason the system should provide optimal conditions for cellular growth. Thus the volume and temperature of the cell medium should be constant and well controllable. Furthermore all kind of non-natural external stimuli of the cells should be avoided as the cytotoxic impact of nanoparticles on the cells will be investigated. An influence on results by an artificial stimulation of the cells e.g. by a sudden change of external conditions should be avoided.

8.3.1 Fluid evaporation from the microfluidic channel

As the cells should be exposed to non-changing conditions, the fluid volume inside the microfluidic channel should be constant between a time period of about 0 - 7 h which is the typical time range of the experiments carried out under static conditions. Furthermore, variations in the volume of the cell media would also influence the flow characteristics in the channel system and thus change the experimental settings. The channel system with the original channel design (see Figure 8.1) contains a channel volume of approx. 200 μl . To avoid overflow, the channel was filled with 180 μl of cell medium during the experiments. First experiments showed that the fluid flow is stopped after an average time of 95 min due to solvent evaporation. The main fluid loss occurred at the contact point between SAW-Chip and coverglass due to very high temperatures in this region (see Section 8.3.2). We therefore tested two further channel designs. In one channel system, a reservoir was added by manually cutting an additional channel into the PDMS. The resulting system had a volume of approx. 320 μl . For the second channel system, the original design was retained but the channel was closed by a PDMS layer preventing fluid evaporation. To allow filling the channel system two holes were cut in the closing layer as far away as possible from the hot SAW chip (see

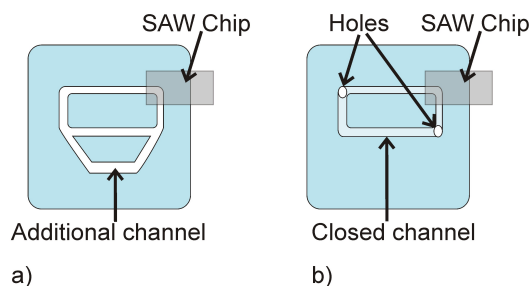


Figure 8.3: Additional channel designs to reduce evaporation from the microfluidic system. a) An additional channel is used to increase the channel volume. b) The channel is closed by a PDMS layer to avoid evaporation. The system can be filled by two holes in the PDMS layer.

Figure 8.3).

The increased volume of the first channel results in a fluid flow which is retained over two hours. Unfortunately, the fluid flow is changed as the fluid is now mainly streaming through the added channel whereas fluid flow in the original channel is reduced to a minimum. This is problematic as due to the geometry of the microfluidic system, fluorescence imaging is only possible in the middle of the PDMS block. The closed channel design efficiently avoids fluid evaporation. Two hours after starting the flow, the channel was still sufficiently filled, and fluid volume was only slightly reduced near the holes. The desired measurement time of 7 h can still not be reached by this channel design, but measurement time is long enough that e.g. refilling the cell medium during the experiments should not significantly influence the experiments. Therefore the closed channel design was used for further experiments.

8.3.2 Temperature characteristics

The temperature inside the channel system is another critical point and should be $37\text{ }^{\circ}\text{C}$ to provide optimal conditions for the cells. We monitored the temperature profile inside the channel system at two different localizations, the channel touching the SAW chip (temperature reading point 1, TRP1) and the channel region which is accessible for fluorescence microscopy measurements (temperature reading point 2, TRP2). Both reading points are marked in Figure 8.4. We used an IR thermometer (testo 830-T3, Testo AG) with an accuracy $0.5\text{ }^{\circ}\text{C}$ allowing contactless measurements. The emission ratio of the thermometer was set to 0.95 corresponding to the emission ratio of water. The diameter of the measurement area was 2 mm at a measurement distance of 2.5 cm, thus being twice the size of the channel. We assumed that the PDMS surrounding the liquid has the same temperature as the fluid within the channel. Control measurements with a contact measuring sensor placed directly into the cell medium proved that this assumption was right. As the measuring sensor interfered with the fluid flow, the contactless measurement setup was preferred. In a first experiment, we monitored

8.3 Characterization and adaption to live-cell imaging requirements

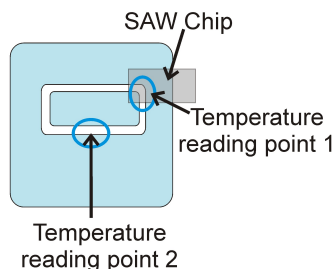


Figure 8.4: Location of the temperature reading points within the microfluidic channel system. Reading point 1 is localized on top of the SAW chip, reading point 2 is the channel region which is accessible for fluorescence microscopy measurements.

the temperature at TRP1 and TRP2 during a time period of 120 minutes. The temperature curves are presented in Figure 8.5 a. At both reading points the temperature is increasing within the first 20-30 minutes starting from 26 °C and reaching around 45 °C (TRP1) and 32 °C (TRP2). After this the temperature stays constant until, between 80 and 100 minutes a temperature jump from 45 to 50 °C occurs near the SAW chip. The increased temperature near the SAW chip is probably due to the hindered proliferation of the SAW from the LiNbO₃ chip through the immersion oil to the coverglass. The SAW is thereby damped leading to a localized heating of the system. This local heating at the SAW chip is critical as cell can not survive these temperatures. Cells that are subdued to such conditions might secrete messengers influencing other cells in the microfluidic systems. Furthermore the temperature in the region which is accessible for live-cell imaging is to low.

We therefore investigated if the temperature can be influenced by external heating with a heating stage. We measured the temperature profile in the channel at the two temperature reading points over a time range of 60 min. The temperature of the heating table was set to 32.5, 35 and 40 °C in subsequent experiments. It was not possible to use an additional heating ring for the objective due to a lack of space underneath the microfluidic system. The temperature curves are shown in Figure 8.5 b. The temperature increases in response to an increasing external temperature in both spots but the temperature of the cell media being in contact with the SAW (TRP1) reacts less to the external heating than the temperature at the fluorescence imaging spot (TRP2). The external temperature control is a good method to fine tune the temperature inside the system. Nevertheless it does not provide the possibility to cool the media near the SAW chip to avoid cell burning. Therefore external heating alone is not sufficient. The heating at the SAW region could probably be avoided by improving the contact between SAW chip and coverglass. Furthermore an external cooling with e.g. a Peltier Element would be possible and should be tried.

8 Microfluidic system

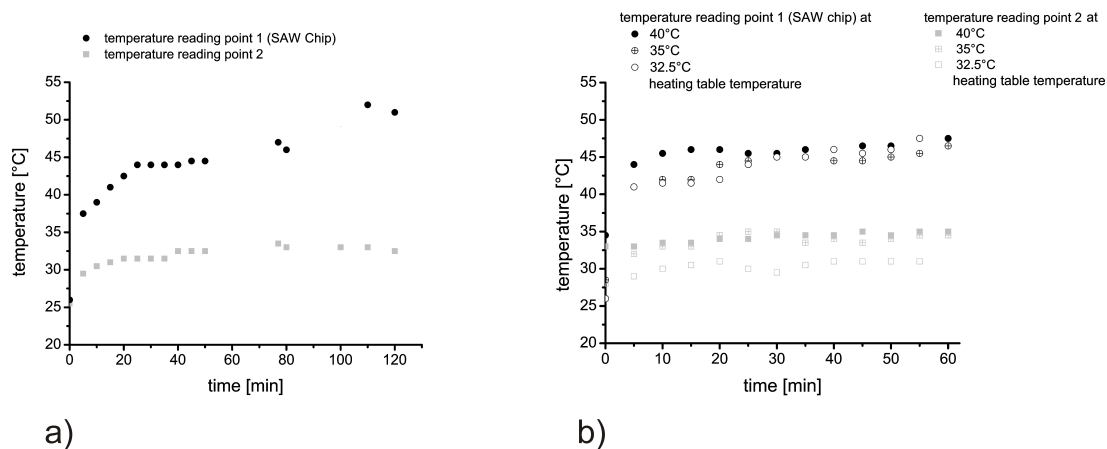


Figure 8.5: a) Temperature profile of the cell medium in the microfluidic channel on top of the SAW chip (reading point 1) and in the channel region accessible for fluorescence microscopy (reading point 2) without external heating. b) Influence of external temperature control on the temperature of the cell medium.

8.3.3 Flow rates

The microfluidic system will be used to generate an artificial blood flow on top of the cells. The flow velocities in the system should therefore be similar to flow velocities in the human body. The blood vessel system is very heterogeneous in size and morphology. For example, the arterial system can be divided into the macrovascular network which contains large arteries down to a diameter of 500 μm , the mesovascular network which are small arteries and arterioles from 500 μm down to 10 μm and the microvascular network representing the capillary bed [166]. Therefore it is not astonishing that a whole variety of blood flow velocities are mentioned in different publications. London *et al.* [167] state that blood flow velocities are in the order of cm/s. In another project coronary arterial flow was found to be around 20-40 cm/s [168]. The average flow velocity in capillaries is a fraction of mm/s [169] and was found to be in the range of 15-25 $\mu\text{m}/\text{s}$ for capillaries having a luminal diameter of 5 to 10 μm [170]. This is in agreement with the flow velocity of 10 $\mu\text{m}/\text{s}$ found in a capillary with 5 μm diameter [171] whereas another study claims that the capillary blood flow ranges from 500 - 1000 $\mu\text{m}/\text{sec}$ [172].

The diameter of the artificial blood vessel used in this work is 1 mm therefore corresponding to the dimensions of large arteries from the macrovascular system. We investigated the flow inside the microfluidic channel for two different excitation intensities for the SAW (27 dBm (500 mW) and 30 dBm (1 W)) by monitoring the movement of 170 μm surface-carboxylated fluorescent polymerbeads via a widefield fluorescence microscope. Movies of the particle motion were acquired approx. 20, 30 and 80 μm over the coverglass but, as widefield microscopy was used, also particles outside the focal region were visible. The motion of the particle was tracked by the program “virotracker” and the flow velocities of the particles were extracted. The particle’s movement increased with increasing distance from the coverglass which is typical for laminar flow conditions. 80 μm above the coverglass flow velocities were found to be 23 $\mu\text{m}/\text{s}$ (27 dBm excitation) and 71 $\mu\text{m}/\text{s}$ (30 dBm excitation).

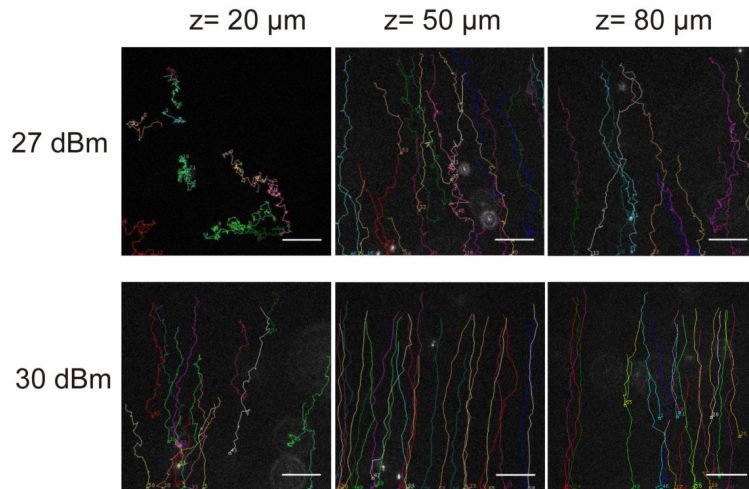


Figure 8.6: Tracks of polymer beads within the microfluidic system at three different coverglass distances and two SAW excitation intensities. Particles near the coverglass show diffusive behavior whereas with increasing coverglass distance the flow velocities increase resulting in linear particle movement. Scalebar = 10 μm

The closer to the coverglass and therefore to the cellular localization, the slower is the flow. At a coverglass distance of 30 μm , flow velocities were already reduced to 50 $\mu\text{m}/\text{s}$ (30 dBm excitation). Figure 8.6 shows the traces of particles within the microfluidic system at different SAW excitation intensities and coverglass differences. With decreasing flow velocities, the particles show a more and more pronounced diffusive motion.

Compared to the values found for arterial flow in the macrovascular network, the monitored flow velocities are approximately a factor 10^3 too small and therefore need to be increased. This could be achieved by higher SAW excitation intensities. Unfortunately this also induces additional heating of the system and thus worsens the heating problem. Another possibility is to enhance the SAW transition between the SAW chip and the coverglass leading to faster flow velocities as well as to reduced heating. Furthermore the channels could be narrowed meaning that lower flow velocities are needed to simulate natural blood flow conditions as well as less fluid has to be accelerated by the SAW.

8.4 Summary and conclusion

The microfluidic system provided by Prof. A. Wixforth (University of Augsburg) and M.F Schneider (Boston University) is designed to mimic the natural flow conditions for endothelial cells during live-cell imaging. Due to its compact size it is ideally suited for integration into a microscopic setup. The simple assembly and the flexible design of the channel system allows to vary the experimental conditions and to simulate a variety of blood vessel structures. The microfluidic flow is created using the surface acoustic wave (SAW) technology. The system was characterized concerning tempera-

8 Microfluidic system

ture, flow velocities and evaporation behavior of the liquid as stable experimental conditions are a prerequisite for a reliable cytotoxicity assessment. First experiments showed that the cell medium evaporates from the open system within 95 minutes. By using a closed channel system fluid flow could be sustained for over two hours. The fast fluid evaporation results from a strong heating of the medium above the SAW chip. Due to damping of the SAW, peak temperatures up to 50 °C were reached during the experiments. This is a serious problem which has to be addressed in future as the cells will not survive such temperatures and will probably release stress factors into the medium. In contrary, the temperature at the channel position monitored during live-cell imaging was shown to be well controllable by an external heating device. In a further experiment the flow velocities within the channel were assessed by recording the motion of polystyrene beads via widefield microscopy. Due to its dimensions, the used artificial blood vessel corresponds to an human artery from the macrovascular system where blood flow reaches velocities up to cm/s. During our experiments a maximal flow velocity of 71 $\mu\text{m/s}$ could be achieved. Further experiments e.g. with smaller vessel geometries or an increased SAW excitation power need to be carried out in order to solve this problem. In summary, the microfluidic system is very promising for live-cell imaging assessment of cytotoxicity at blood flow conditions but further improvements need to be done.

9 Interaction of nanoparticles with lipid vesicles

The cell membrane is the first barrier nanoparticles interact with and have to cross when being taken up into the cell. We were interested if nanoparticles may change the mechanical properties of the membranes and if cytotoxic impact of nanoparticles may be linked to particle membrane interactions. As a model system for cell membranes we used giant unilamellar vesicles (GUV)s. GUVs are known to show a very distinctive budding effects during phase transition. When incubated with nanoparticles, this behavior changes significantly allowing to draw conclusions about basic mechanisms of nanoparticle lipid membrane interactions. We observed the GUV morphologies during phase transition in presence and absence of nanoparticles by fluorescence widefield microscopy. The experiments were carried out in Munich, at AK Prof. Bräuchle, together with C. Westerhausen and F. Strobl (AK Prof. Wixforth, University of Augsburg). In the following the experiments are summarized and discussed. Details can also be found in the diploma thesis of F. Strobl [173].

9.1 Lipid membranes and giant unilamellar vesicles

Lipids are amphiphilic molecules consisting of a polar head group and an apolar hydrocarbon chain. When exposed to water, lipids spontaneously form aggregates in order to shield their apolar tails from the polar water molecules. One of the morphologies adapted are two-dimensional sheets, so called lipid bilayers. The latter have an apolar central double layer containing the apolar lipid tails which is enclosed from both sides by a polar layer formed by the head groups. Lipid bilayers can spontaneously adapt spherical shape in order to avoid contact between the hydrophobic layer and the water at the edges of the membrane. The resulting vesicles have different sizes and appearances. One type are unilamellar vesicles. They are composed of one single lipid bilayer. Depending on their diameter they are referred to as small unilamellar vesicles (10 nm - 100 nm), large unilamellar vesicles (100 nm - 1 μm) or giant unilamellar vesicles (10 μm - 100 μm). The lipids within the bilayer adapt different arrangements depending on the external conditions as depicted in Figure 9.1. At lower temperatures they form a two dimensional triangular lattice in the membrane plane with long range order. The hydrocarbon tails of the lipid are preferably in all-trans configuration. Lipids in this configuration, the so-called gel phase, can hardly diffuse within the bilayer (see Figure 9.1, left). At higher temperatures the membrane changes into the fluid phase (see Figure 9.1, right). The C-C bonds of the hydrocarbon chains now randomly adapt trans-, gauche⁻ and gauche⁺ configurations. The kinks resulting from the gauche conformation lead to a membrane area extension of about 25%

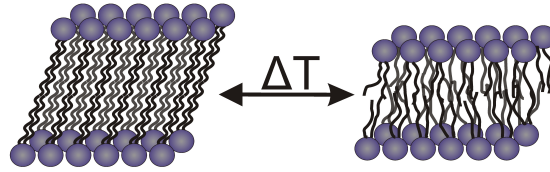


Figure 9.1: Lipid bilayers in the gel (left) and in the fluid phase (right). The gel phase is characterized by a predominant all-trans configuration of the hydrocarbon tails. This results in a two dimensional triangular lattice with long range order. In the fluid phase, the C-C bonds of the hydrocarbon chains adapt randomly trans-, gauche⁻ and gauche⁺ configurations leading to an area extension of about 25% compared to the gel phase. Lipid molecules can diffuse more or less freely in the bilayer whereas they are rather fixed in the gel phase. The phase transition between gel and fluid phase is triggered by an increase in temperature whereas cooling leads to a change back into the gel phase. The image was adapted from [174].

with respect to the gel phase. Lipid molecules in the fluid phase can diffuse more or less freely in the bilayer, leading to a loss in long range order [173, 174]. Depending on the lipid types composing the bilayers, phase transition between the gel and the fluid phase may occur at different temperatures, the so called transition temperature T^* . The vesicles used in the experiments were composed of 1,2-dipalmitoyl-*sn*-glycero-3-phosphocholine (DPPC) leading to a phase transition temperature of $T^* \approx 41^\circ\text{C}$ [173].

9.2 Experimental details

GUVs composed of 1,2-dipalmitoyl-*sn*-glycero-3-phosphocholine (DPPC) were prepared in saccharose solution by electroformation. During synthesis, they were labeled with the membrane dye DiD (Invitrogen; Karlsruhe, Germany). The resulting vesicles had a diameter of 10 - 50 μm . 5 μL of this mixture were added to 60 μL glucose solution containing Atto488-SiO₂-89 which are 89 ± 24.4 nm sized particles labeled with Atto 488 (ATTO-Tec, Germany). The mixture was filled into the sample chamber (see Figure 9.2). The latter was closed by a cover glass and sealed with silicon. The temperature in the chamber can be regulated by a peltier element which allows heating and cooling rates of up to ± 1 K/s.

The sample chamber was placed on the widefield fluorescence microscope and image sequences were captured with a time resolution of 100 ms or 300 ms per channel, exciting DiD and Atto488 with 633 nm and 488 nm laser light respectively. During observation, the GUVs were brought from one phase to the other by heating/cooling the sample solution in the temperature range of 35 to 55°C.

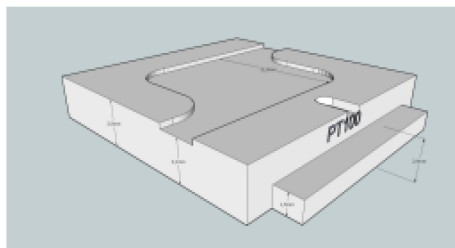


Figure 9.2: Sample chamber used to heat the sample solution containing giant unilamellar vesicles (GUVs) and SiO_2 nanoparticles across the phase transition temperature ($T^* \approx 41^\circ\text{C}$) of the vesicles. The change in vesicle morphology during phase transition is monitored by widefield fluorescence microscopy. The image is taken from [173].

9.3 Observations and discussion

In the following sections the observations made during the experiments are summarized. The phase transition behavior of GUVs in absence and presence of nanoparticles is compared and possible explanations for the observed differences are proposed. For a complete understanding of the underlying processes, further experiments, e.g. with differently sized particles, need to be done to support and expand the current knowledge.

9.3.1 Phase transition of giant unilamellar vesicles

When GUVs are heated across their phase transition temperature T^* they show a distinctive behavior. In image 9.3 the most prominent vesicle shapes occurring during this transition are depicted.

Vesicles in the gel phase have a spherical shape (Figure 9.3 a). Upon heating, the membrane surface expands but the enclosed vesicle volume stays constant as only very low amounts of water can diffuse through the membrane. This increased surface to volume ratio leads first to an elongation of the vesicle (Figure 9.3 b). Later on buds with varying shapes are formed on the surface (Figure 9.3 c). These daughter vesicles are attached to the mother vesicle via thin membrane necks. If the GUVs are now cooled quickly beyond their transition temperature, these buds can be released from the membrane. If the sample is cooled slowly, the previous process is reversible and the vesicles fuse back leading again to spherical vesicles (Figure 9.3 d). This typical behavior of GUVs during phase transition can be explained applying the so called area-difference elasticity model (ADE model) [175]. Briefly, the model ascribes morphological changes of lipid vesicles to changes in the surface area of the vesicles. The change in surface area influences two parameters, the reduced volume \bar{v} and the reduced area difference \bar{a} which determine the shape of the vesicles. The reduced area difference describes the difference between the relaxed and the actual membrane area. The relaxed membrane area is calculated from the number of lipid molecules times their average size whereas the actual membrane area is equal to the area occupied by the lipid molecules in the current structure. The reduced volume shows the ratio between the real volume and the maximal obtainable volume (sphere)

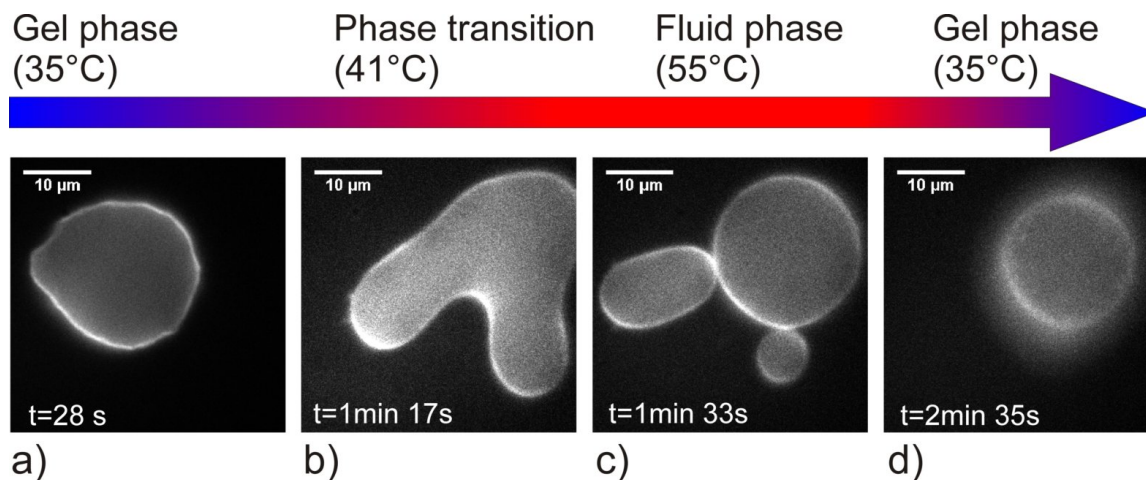


Figure 9.3: Typical morphologies occurring during the phase transition of giant unilamellar vesicles in absence of nanoparticles. a) In the gel phase the vesicles show spherical morphology. b) When the vesicle reaches the fluid phase, its surface increases whereas the enclosed volume stays constant. To account for this changed surface to volume ratio, the vesicle adopts an elongated shape before c) buds are formed on the surface. d) When the vesicle is cooled slowly beyond its phase transition point, the daughter vesicles fuse back and the vesicle relaxes back into its spherical shape.

for the given surface area. Depending on these parameters, the morphology with the lowest energy will be adopted by the system.

9.3.2 Phase transition of giant unilamellar vesicles in the presence of nanoparticles

Nanoparticles that interact with the lipid membrane change the vesicle behavior during phase transition. Figure 9.4 a shows a GUV at a temperature slightly below the transition temperature. Nanoparticles and nanoparticle aggregates (both depicted in green) are visible on the surface of the GUV (shown in magenta). The probe solution is heated with a rate of $\approx 0.5^\circ\text{K/s}$, inducing membrane area enlargement. When the phase transition temperature is reached, the particles and particle aggregates start moving towards each other (see white arrows in Figure 9.4 b and c) until they attach and form new aggregates (Figure 9.4 d, blue arrows). As indicated with blue arrows in Figure 9.4 d, the membrane bends inwards at the site of the newly formed aggregates and the vesicle is narrowed down. When cooled down beyond the phase transition point, the membrane relaxes back into its spherical shape (Figure 9.4 e). The nanoparticles are now distributed more irregularly on the vesicle.

Another effect which can be observed for some vesicles is intravesicular budding during phase transition. Two examples for this morphology can be seen in Figure 9.5 where both vesicles are in the fluid phase. When the temperature is decreased, the daughter vesicle remains stable and enclosed into the mother vesicle. Both mother and daughter vesicles relax back into the spherical shape. Most particles are localized within the internal vesicles after this process. This intravesicular

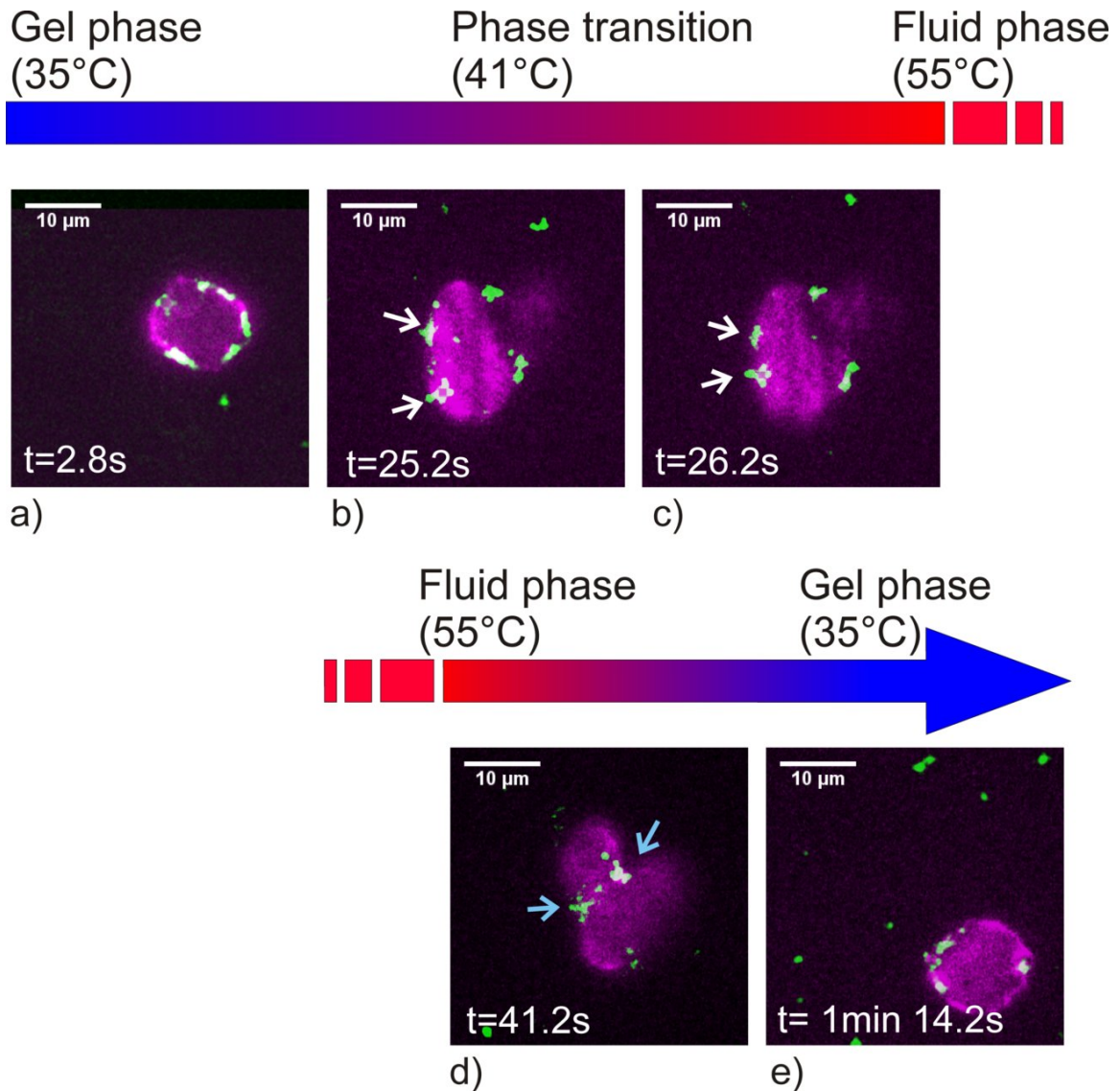


Figure 9.4: Typical morphologies of giant unilamellar vesicles during phase transition when they are in contact with nanoparticles. a) Before phase transition, the GUV (magenta) has a spherical shape with nanoparticles and nanoparticle aggregates (green) attached to its surface. b, c) During phase transition, the particles and aggregates move towards each other (see white arrows) and finally form d) bigger aggregates. At the site of the aggregates an inward membrane bending can be observed (see blue arrows). e) When the GUVs are cooled down beyond their phase transition temperature, the vesicles adopt a spherical shape. The distribution of particles on the surface appears to be more irregularly than initially.

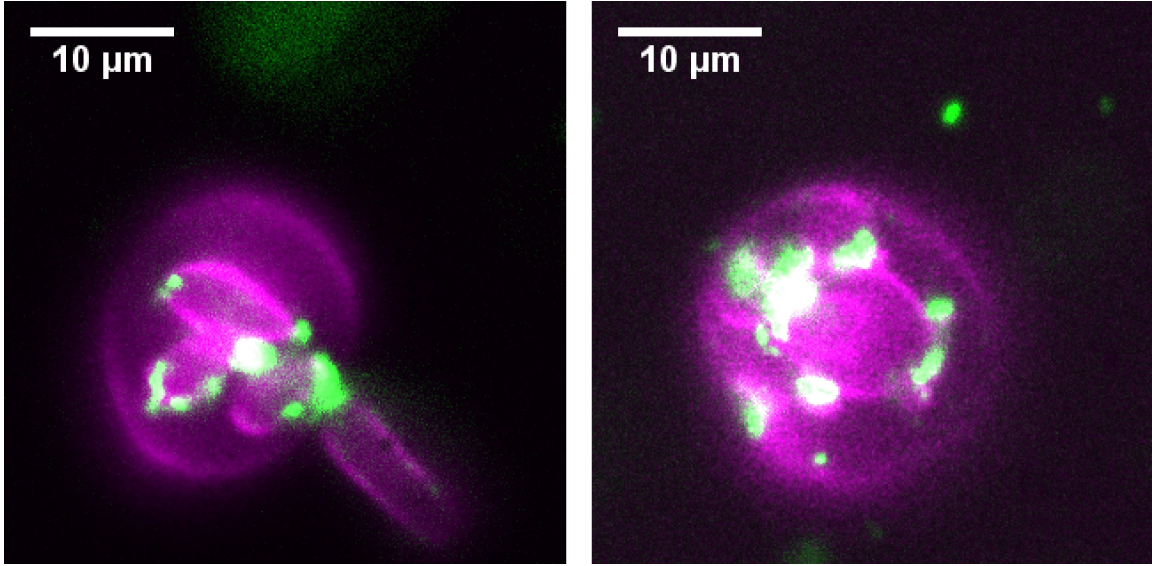


Figure 9.5: Giant unilamellar vesicles with enclosed daughter vesicles (magenta). The daughter vesicles are formed during phase transition from the gel to the fluid phase. Most particles and particle aggregates (both shown in green) are transferred to the internalized vesicles.

budding reminds strongly on endocytosis in living cells. It is interesting that this process can be induced in artificial systems purely by the presence of nanoparticles. In addition also a kind of exocytosis can be observed in the artificial system. When cooled beyond the phase transition point, the daughter vesicles were found to cross the membrane and be expelled from the mother vesicle in some cases.

The observed morphological changes of the vesicles during the phase transition can be explained by the Lipowsky-Döbenreiner model [176]. This model explains the encapsulation of nanoparticles by an interplay of the adhesion energy (E_{ad}) and the bending energy (E_{bend}) which are balancing each other. Both energies are calculated as following when adhesive particles with diameters clearly exceeding the membrane thickness (approx. 4nm) are considered.

$$E_{ad} = -A_{ca} |W| \quad (9.3.1)$$

$$E_{bend} = \frac{A_{ca} 2\kappa}{R_{pa}^2} \quad (9.3.2)$$

where W is equal to the adhesion energy per unit area ($W < 0$), R_{pa} is the radius of the particle, and κ the bending rigidity of the membrane. The contact area A_{ca} between particle and vesicle for a certain covered surface fraction X is given by

$$A_{ca} = X 4\pi R_{pa}^2 \quad (9.3.3)$$

Depending on the radius of the particle in comparison to a critical radius R^* , the particle will be fully enclosed by the membrane ($X=1$, for $R_{pa} > R^*$) or will be released from the surface (X

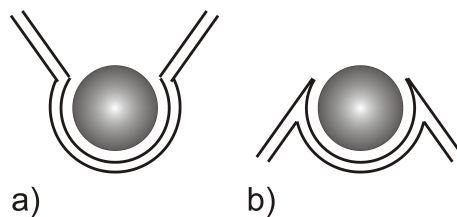


Figure 9.6: The direction of membrane bending at the neck of membrane-wrapped nanoparticles determines the bending energy. a) Negative membrane bending results in lower bending energies compared to b) positive surface bending if both particles have the same surface fraction covered by the membrane. The image was adapted from [173].

$= 0$, for $R_{pa} < R^*$). As in the fluid phase, R^* is approximately equal to 5 nm [176], the particles used in the experiments should be fully encapsulated. In addition to E_{ad} and E_{bend} , two further energies have to be considered in our system. First, the strong bending at the neck between mother vesicle and enclosed particle induces an additional bending energy term. Second, different fractions of membrane area are used on the inside and the outside of the vesicle for particle encapsulation. According to the ADE model (see Section 9.3.1, [175]) the resulting increase in the reduced area difference \bar{a} induces an additional energy. This energy cannot be balanced by flip flop processes of the lipids as they have been shown to be too slow [177]. The two additional energy contributions are minimized when the nanoparticles are incorporated into an area having a small or negative membrane bending, like the observed inwards bended regions of vesicles (see Figure 9.4 d). A schematic representation of this effect is shown in Figure 9.6. If a constant surface fraction X of the vesicle is enclosed by the membrane, the bending energy at the neck is smaller for a negative (see Figure 9.6 a) compared to a positive bending of the membrane (Figure 9.6 b). As soon as a bended region has been formed, it is favorable for other particles to move towards this location. Another region with negative membrane bending are the intravesicular buds which are shown in Figure 9.5. Nanoparticles should therefore preferentially accumulate in these buds. Both, particle movement towards the inwards bended region and particle accumulation in intravesicular daughter vesicles were clearly observed during our experiments.

9.4 Summary and conclusions

The investigation of nanoparticle-membrane-interactions showed that nanoparticles indeed influence the morphological behavior of lipid vesicles, most probably because of changes in their mechanical properties. During phase transition, vesicles without nanoparticle contact form daughter vesicles on the outer surface which are connected to the mother vesicles via thin necks during phase transition. By this morphological transformation, the vesicle adapts to the increased surface to volume ratio induced by the change from the gel to the fluid phase of the lipid membrane. The presence of nanoparticles on the vesicle surface changes this behavior significantly. Instead of budding to the outside an inwards bending of the membrane is observed. This bending is accompanied by a particle

9 Interaction of nanoparticles with lipid vesicles

diffusion within the membrane leading to particle agglomeration. During this process, intravesicular daughter vesicles are often formed containing most of the nanoparticles. This morphology change is probably induced by the additional energy contributions due to the nanoparticle adhesion and increased membrane bending. This intravesicular budding reminds strongly of endocytosis in cells. It is astonishing that the addition of nanoparticles to an artificial cellular system leads to a spontaneous inwards budding and an accumulation of the particles in intravesicular compartments which is very similar to cellular endocytosis processes observed in nature. These findings suggest that the basic mechanisms of these highly regulated and complicated natural processes can be explained by simple physical effects.

Bibliography

- [1] L. Wolz. Die Zwerge sind unter uns. *Stern*, <http://www.stern.de/wissen/mensch/nanotechnologie-riskant-oder-harmlos-die-zwerge-sind-unter-uns-1685724.html>, 2011.
- [2] Bund fuer Umwelt und Naturschutz Deutschland e.V. (BUND). http://www.bund.net/bundnet/themen_und_projekte/nanotechnologie/.
- [3] SPP1313 Biological Responses to Nanoscale Particles. www.spp1313.de. 2007.
- [4] J. Blechinger, R. Herrmann, D. Kiener, F. J. Garcia-Garcia, C. Scheu, A. Reller, and C. Bräuchle. Perylene-labeled silica nanoparticles: synthesis and characterization of three novel silica nanoparticle species for live-cell imaging. *Small*, 6(21):2427–35, 2010.
- [5] J. Blechinger, A. A. Torrano, C. Argyo, A. Reller, T. Bein, and C. Bräuchle. A fast analysis method to quantify nanoparticle uptake on a single cell leve. *submitted to Nanomedicine*, 2011.
- [6] J. Blechinger, A. T. Bauer, A. A. Torrano, C. Gorzelanny, C. Bräuchle, and S. W. Schneider. Silica nanoparticles: Nanotoxicity is dependent on the uptake behavior of the cell and therefore cell type dependent. *submitted to Small*, 2012.
- [7] H. F. Krug and P. Wick. Nanotoxicology: An interdisciplinary challenge. *Angew Chem Int Ed Engl*, 2011.
- [8] C. Buzea, II Pacheco, and K. Robbie. Nanomaterials and nanoparticles: sources and toxicity. *Biointerphases*, 2(4):MR17–71, 2007.
- [9] H. Goesmann and C. Feldmann. Nanoparticulate functional materials. *Angewandte Chemie-International Edition*, 49(8):1362–1395, 2010.
- [10] A. Nel, T. Xia, L. Madler, and N. Li. Toxic potential of materials at the nanolevel. *Science*, 311(5761):622–7, 2006.
- [11] R. F. Service. Nanotoxicology. nanotechnology grows up. *Science*, 304(5678):1732–4, 2004.
- [12] D. A. Taylor. Dust in the wind. *Environ Health Perspect*, 110(2):A80–7, 2002.
- [13] P. R. Buseck and M. Posfai. Airborne minerals and related aerosol particles: Effects on climate and the environment. *Proceedings of the National Academy of Sciences of the United States of America*, 96(7):3372–3379, 1999.

Bibliography

- [14] S. T. Ballard, J. C. Parker, and C. R. Hamm. Restoration of mucociliary transport in the fluid-depleted trachea by surface-active instillates. *Am J Respir Cell Mol Biol*, 34(4):500–4, 2006.
- [15] B. M. Simonet and M. Valcarcel. Monitoring nanoparticles in the environment. *Analytical and Bioanalytical Chemistry*, 393(1):17–21, 2009.
- [16] Bund fuer Umwelt und Naturschutz Deutschland e.V. (BUND). http://www.bund.net/bundnet/themen_und_projekte/nanotechnologie/nanoproduktdatenbank/.
- [17] Surinder Mann. Nanoforum report: Nanotechnology and construction. Technical report, Institute of Nanotechnology, 2006.
- [18] B. G. Priestly, A. J. Harford, and M. R. Sim. Nanotechnology: a promising new technology—but how safe? *Med J Aust*, 186(4):187–8, 2007.
- [19] R. A. Drezek and J. M. Tour. Is nanotechnology too broad to practise? *Nat Nanotechnol*, 5(3):168–9, 2010.
- [20] A. Grobe. Verantwortlicher umgang mit nanotechnologien - bericht und empfehlungen der nanokommission 2011.
- [21] A. Seaton and K. Donaldson. Nanoscience, nanotoxicology, and the need to think small. *Lancet*, 365(9463):923–4, 2005.
- [22] P. H. Hoet, I. Bruske-Hohlfeld, and O. V. Salata. Nanoparticles - known and unknown health risks. *J Nanobiotechnology*, 2(1):12, 2004.
- [23] G. Oberdorster, J. Ferin, and B. E. Lehnert. Correlation between particle size, in vivo particle persistence, and lung injury. *Environ Health Perspect*, 102 Suppl 5:173–9, 1994.
- [24] W. G. Kreyling, M. Semmler-Behnke, J. Seitz, W. Scymczak, A. Wenk, P. Mayer, S. Takenaka, and G. Oberdorster. Size dependence of the translocation of inhaled iridium and carbon nanoparticle aggregates from the lung of rats to the blood and secondary target organs. *Inhal Toxicol*, 21 Suppl 1:55–60, 2009.
- [25] M. Geiser, B. Rothen-Rutishauser, N. Kapp, S. Schurch, W. Kreyling, H. Schulz, M. Semmler, V. Im Hof, J. Heyder, and P. Gehr. Ultrafine particles cross cellular membranes by nonphagocytic mechanisms in lungs and in cultured cells. *Environ Health Perspect*, 113(11):1555–60, 2005.
- [26] A. Nemmar, H. Vanbilloen, M. F. Hoylaerts, P. H. Hoet, A. Verbruggen, and B. Nemery. Passage of intratracheally instilled ultrafine particles from the lung into the systemic circulation in hamster. *Am J Respir Crit Care Med*, 164(9):1665–8, 2001.
- [27] G. Oberdorster. Pulmonary effects of inhaled ultrafine particles. *Int Arch Occup Environ Health*, 74(1):1–8, 2001.

- [28] T. Kato, T. Yashiro, Y. Murata, D. C. Herbert, K. Oshikawa, M. Bando, S. Ohno, and Y. Sugiyama. Evidence that exogenous substances can be phagocytized by alveolar epithelial cells and transported into blood capillaries. *Cell Tissue Res*, 311(1):47–51, 2003.
- [29] N. Hussain, V. Jaitley, and A. T. Florence. Recent advances in the understanding of uptake of microparticulates across the gastrointestinal lymphatics. *Adv Drug Deliv Rev*, 50(1-2):107–42, 2001.
- [30] H. Lippert. *Lehrbuch Anatomie*, volume 5. Urban and Fischer, Muenchen, 2000.
- [31] G. J. Nohynek, J. Lademann, C. Ribaud, and M. S. Roberts. Grey goo on the skin? nanotechnology, cosmetic and sunscreen safety. *Crit Rev Toxicol*, 37(3):251–77, 2007.
- [32] J. Lademann, M. Meinke, W. Sterry, and A. Patzelt. How safe are nanoparticles? *Hautarzt*, 60(4):305–9, 2009.
- [33] H. Nabeshi, T. Yoshikawa, K. Matsuyama, Y. Nakazato, K. Matsuo, A. Arimori, M. Isobe, S. Tochigi, S. Kondoh, T. Hirai, T. Akase, T. Yamashita, K. Yamashita, T. Yoshida, K. Nagano, Y. Abe, Y. Yoshioka, H. Kamada, T. Imazawa, N. Itoh, S. Nakagawa, T. Mayumi, S. Tsunoda, and Y. Tsutsumi. Systemic distribution, nuclear entry and cytotoxicity of amorphous nanosilica following topical application. *Biomaterials*, 32(11):2713–24, 2011.
- [34] M. P. Monopoli, D. Walczyk, A. Campbell, G. Elia, I. Lynch, F. B. Bombelli, and K. A. Dawson. Physical-chemical aspects of protein corona: relevance to in vitro and in vivo biological impacts of nanoparticles. *J Am Chem Soc*, 133(8):2525–34, 2011.
- [35] A. E. Nel, L. Madler, D. Velegol, T. Xia, E. M. Hoek, P. Somasundaran, F. Klaessig, V. Castanova, and M. Thompson. Understanding biophysicochemical interactions at the nano-bio interface. *Nat Mater*, 8(7):543–57, 2009.
- [36] Z. J. Deng, G. Mortimer, T. Schiller, A. Musumeci, D. Martin, and R. F. Minchin. Differential plasma protein binding to metal oxide nanoparticles. *Nanotechnology*, 20(45):455101, 2009.
- [37] M. Lundqvist, J. Stigler, G. Elia, I. Lynch, T. Cedervall, and K. A. Dawson. Nanoparticle size and surface properties determine the protein corona with possible implications for biological impacts. *Proc Natl Acad Sci U S A*, 105(38):14265–70, 2008.
- [38] T. Ishida, H. Harashima, and H. Kiwada. Interactions of liposomes with cells in vitro and in vivo: opsonins and receptors. *Curr Drug Metab*, 2(4):397–409, 2001.
- [39] B. D. Chithrani and W. C. Chan. Elucidating the mechanism of cellular uptake and removal of protein-coated gold nanoparticles of different sizes and shapes. *Nano Lett*, 7(6):1542–50, 2007.
- [40] G. Oberdorster. Safety assessment for nanotechnology and nanomedicine: concepts of nanotoxicology. *J Intern Med*, 267(1):89–105, 2010.

Bibliography

- [41] D. Walczyk, F. B. Bombelli, M. P. Monopoli, I. Lynch, and K. A. Dawson. What the cell "sees" in bionanoscience. *J Am Chem Soc*, 132(16):5761–8, 2010.
- [42] M. Lundqvist, I. Sethson, and B. H. Jonsson. Protein adsorption onto silica nanoparticles: conformational changes depend on the particles' curvature and the protein stability. *Langmuir*, 20(24):10639–47, 2004.
- [43] S. S. Karajanagi, A. A. Vertegel, R. S. Kane, and J. S. Dordick. Structure and function of enzymes adsorbed onto single-walled carbon nanotubes. *Langmuir*, 20(26):11594–9, 2004.
- [44] I. Lynch, K. A. Dawson, and S. Linse. Detecting cryptic epitopes created by nanoparticles. *Sci STKE*, 2006(327):pe14, 2006.
- [45] K. Wiench, W. Wohlleben, V. Hisgen, K. Radke, E. Salinas, S. Zok, and R. Landsiedel. Acute and chronic effects of nano- and non-nano-scale tio(2) and zno particles on mobility and reproduction of the freshwater invertebrate daphnia magna. *Chemosphere*, 76(10):1356–65, 2009.
- [46] B. Halliwell and J. M. Gutteridge. *Free Radicals in Biology and Medicine*. Oxford, Clarendon Pr., 1986.
- [47] A. Nel. Atmosphere. air pollution-related illness: effects of particles. *Science*, 308(5723):804–6, 2005.
- [48] G. G. Xiao, M. Wang, N. Li, J. A. Loo, and A. E. Nel. Use of proteomics to demonstrate a hierarchical oxidative stress response to diesel exhaust particle chemicals in a macrophage cell line. *J Biol Chem*, 278(50):50781–90, 2003.
- [49] W. J. Stark. Nanoparticles in biological systems. *Angewandte Chemie-International Edition*, 50(6):1242–1258, 2011.
- [50] E. K. Richman and J. E. Hutchison. The nanomaterial characterization bottleneck. *ACS Nano*, 3(9):2441–6, 2009.
- [51] M. A. Dobrovolskaia, D. R. Germolec, and J. L. Weaver. Evaluation of nanoparticle immunotoxicity. *Nat Nanotechnol*, 4(7):411–4, 2009.
- [52] P. M. Hinderliter, K. R. Minard, G. Orr, W. B. Chrisler, B. D. Thrall, J. G. Pounds, and J. G. Teeguarden. Isdd: A computational model of particle sedimentation, diffusion and target cell dosimetry for in vitro toxicity studies. *Part Fibre Toxicol*, 7(1):36, 2010.
- [53] E. C. Cho, Q. Zhang, and Y. Xia. The effect of sedimentation and diffusion on cellular uptake of gold nanoparticles. *Nat Nanotechnol*, 6(6):385–91, 2011.
- [54] D. Napierska, L. C. Thomassen, D. Lison, J. A. Martens, and P. H. Hoet. The nanosilica hazard: another variable entity. *Particle and fibre toxicology*, 7(1):39, 2010.

- [55] IARC. Iarc monographs on the evaluation of carcinogenic risks to humans, volume 86, silica, 1997.
- [56] National Center for Biotechnology Information, U.S. National Library of Medicine. <http://www.ncbi.nlm.nih.gov/pubmed>.
- [57] H. Nabeshi, T. Yoshikawa, K. Matsuyama, Y. Nakazato, A. Arimori, M. Isobe, S. Tochigi, S. Kondoh, T. Hirai, T. Akase, T. Yamashita, K. Yamashita, T. Yoshida, K. Nagano, Y. Abe, Y. Yoshioka, H. Kamada, T. Imazawa, N. Itoh, S. Tsunoda, and Y. Tsutsumi. Size-dependent cytotoxic effects of amorphous silica nanoparticles on langerhans cells. *Die Pharmazie*, 65(3):199–201, 2010.
- [58] D. Napierska, L. C. Thomassen, V. Rabolli, D. Lison, L. Gonzalez, M. Kirsch-Volders, J. A. Martens, and P. H. Hoet. Size-dependent cytotoxicity of monodisperse silica nanoparticles in human endothelial cells. *Small*, 5(7):846–53, 2009.
- [59] Y. Li, L. Sun, M. Jin, Z. Du, X. Liu, C. Guo, P. Huang, and Z. Sun. Size-dependent cytotoxicity of amorphous silica nanoparticles in human hepatoma hepg2 cells. *Toxicology in vitro : an international journal published in association with BIBRA*, 2011.
- [60] T. Morishige, Y. Yoshioka, H. Inakura, A. Tanabe, X. Yao, S. Tsunoda, Y. Tsutsumi, Y. Mukai, N. Okada, and S. Nakagawa. Cytotoxicity of amorphous silica particles against macrophage-like thp-1 cells depends on particle-size and surface properties. *Die Pharmazie*, 65(8):596–9, 2010.
- [61] X. Yang, J. Liu, H. He, L. Zhou, C. Gong, X. Wang, L. Yang, J. Yuan, H. Huang, L. He, B. Zhang, and Z. Zhuang. Sio2 nanoparticles induce cytotoxicity and protein expression alteration in hacat cells. *Particle and fibre toxicology*, 7:1, 2010.
- [62] D. Drescher, G. Orts-Gil, G. Laube, K. Natte, R. W. Veh, W. Osterle, and J. Kneipp. Toxicity of amorphous silica nanoparticles on eukaryotic cell model is determined by particle agglomeration and serum protein adsorption effects. *Analytical and Bioanalytical Chemistry*, 400(5):1367–73, 2011.
- [63] M. Al-Rawi, S. Diabate, and C. Weiss. Uptake and intracellular localization of submicron and nano-sized sio(2) particles in hela cells. *Archives of toxicology*, 85(7):813–26, 2011.
- [64] K. M. Waters, L. M. Masiello, R. C. Zangar, B. J. Tarasevich, N. J. Karin, R. D. Quesenberry, S. Bandyopadhyay, J. G. Teeguarden, J. G. Pounds, and B. D. Thrall. Macrophage responses to silica nanoparticles are highly conserved across particle sizes. *Toxicological sciences : an official journal of the Society of Toxicology*, 107(2):553–69, 2009.
- [65] L. Sun, Y. Li, X. Liu, M. Jin, L. Zhang, Z. Du, C. Guo, P. Huang, and Z. Sun. Cytotoxicity and mitochondrial damage caused by silica nanoparticles. *Toxicology in vitro : an international journal published in association with BIBRA*, 2011.

Bibliography

- [66] J. Palomaki, P. Karisola, L. Pylkkanen, K. Savolainen, and H. Alenius. Engineered nanomaterials cause cytotoxicity and activation on mouse antigen presenting cells. *Toxicology*, 267(1-3):125–31, 2010.
- [67] J. S. Chang, K. L. Chang, D. F. Hwang, and Z. L. Kong. In vitro cytotoxicity of silica nanoparticles at high concentrations strongly depends on the metabolic activity type of the cell line. *Environ Sci Technol*, 41(6):2064–8, 2007.
- [68] A. T. Bauer, E. A. Strozyk, C. Gorzelanny, C. Westerhausen, A. Desch, M. F. Schneider, and S. W. Schneider. Cytotoxicity of silica nanoparticles through exocytosis of von willebrand factor and necrotic cell death in primary human endothelial cells. *Biomaterials*, accepted, 2011.
- [69] H. Bayir and V. E. Kagan. Bench-to-bedside review: Mitochondrial injury, oxidative stress and apoptosis—there is nothing more practical than a good theory. *Critical care*, 12(1):206, 2008.
- [70] Y. S. Lin and C. L. Haynes. Impacts of mesoporous silica nanoparticle size, pore ordering, and pore integrity on hemolytic activity. *Journal of the American Chemical Society*, 132(13):4834–42, 2010.
- [71] C. Colliex. *Elektronenmikroskopie - Eine anwendungsbezogene Einführung*. WVG Wissenschaftliche Verlagsgesellschaft mbH, Stuttgart, 2008.
- [72] M. Kaszuba and M. T. Connah. Protein and nanoparticle characterisation using light scattering techniques. *Particle & Particle Systems Characterization*, 23(2):193–196, 2006.
- [73] M. Medebach, C. Moitzi, N. Freiburger, and O. Glatter. Dynamic light scattering in turbid colloidal dispersions: A comparison between the modified flat-cell light-scattering instrument and 3d dynamic light-scattering instrument. *Journal of Colloid and Interface Science*, 305(1):88–93, 2007.
- [74] E. C. Cho, J. Xie, P. A. Wurm, and Y. Xia. Understanding the role of surface charges in cellular adsorption versus internalization by selectively removing gold nanoparticles on the cell surface with a i2/ki etchant. *Nano Lett*, 9(3):1080–4, 2009.
- [75] A. Villanueva, M. Canete, A. G. Roca, M. Calero, S. Veintemillas-Verdaguer, C. J. Serna, P. Morales Mdel, and R. Miranda. The influence of surface functionalization on the enhanced internalization of magnetic nanoparticles in cancer cells. *Nanotechnology*, 20(11):115103, 2009.
- [76] B. J. Kirby and E. F. Hasselbrink. Zeta potential of microfluidic substrates: 1. theory, experimental techniques, and effects on separations. *Electrophoresis*, 25(2):187–202, 2004.
- [77] A. V. Delgado, E. Gonzalez-Caballero, R. J. Hunter, L. K. Koopal, and J. Lyklema. Measurement and interpretation of electrokinetic phenomena - (iupac technical report). *Pure and Applied Chemistry*, 77(10):1753–1805, 2005.

- [78] Malvern instruments. Zetasizer nano series user manual. MAN 0317(3), 2007.
- [79] P. J. Walla. *Modern Biophysical Chemistry*. Wiley-VCH, Weinheim, 2009.
- [80] J. W. Lichtman and J.-A. Conchello. Fluorescence microscopy. *Nature Methods*, 2(12):910–919, 2005.
- [81] J. R. Lakowicz. *Principles of Fluorescence Spectroscopy*. Springer, New York, 3 edition, 2006.
- [82] Olympus America Inc. <http://www.olympusmicro.com>, 2010.
- [83] M. Mueller. *Confocal fluorescence microscopy*. SPIE PRESS, Bellingham, Washington USA, 2006.
- [84] J. B. Pawley. *Handbook of Biological Confocal Microscopy*. Springer, New York, 3 edition, 2006.
- [85] D. J. Stephens and V. J. Allan. Light microscopy techniques for live cell imaging. *Science*, 300(5616):82–6, 2003.
- [86] W. E. Moerner and D. P. Fromm. Methods of single-molecule fluorescence spectroscopy and microscopy. *Review of Scientific Instruments*, 74(8):3597–3619, 2003.
- [87] S. D. Conner and S. L. Schmid. Regulated portals of entry into the cell. *Nature*, 422(6927):37–44, 2003.
- [88] S. Mayor and R. E. Pagano. Pathways of clathrin-independent endocytosis. *Nat Rev Mol Cell Biol*, 8(8):603–12, 2007.
- [89] M. C. Kerr and R. D. Teasdale. Defining macropinocytosis. *Traffic*, 10(4):364–371, 2009.
- [90] P. P. Di Fiore and P. De Camilli. Endocytosis and signaling. an inseparable partnership. *Cell*, 106:1–4, 2001.
- [91] E. S. Seto, H. J. Bellen, and T. E. Lloyd. When cell biology meets development: endocytic regulation of signaling pathways. *Genes Dev*, 16(11):1314–36, 2002.
- [92] G. J. Doherty and H. T. McMahon. Mechanisms of endocytosis. *Annual Review of Biochemistry*, 78:857–902, 2009.
- [93] R. G. Parton and K. Simons. The multiple faces of caveolae. *Nat Rev Mol Cell Biol*, 8(3):185–94, 2007.
- [94] K. Sandvig, M. L. Torgersen, H. A. Raa, and B. van Deurs. Clathrin-independent endocytosis: from nonexisting to an extreme degree of complexity. *Histochem Cell Biol*, 129(3):267–76, 2008.
- [95] R. G. Parton. Caveolae—from ultrastructure to molecular mechanisms. *Nat Rev Mol Cell Biol*, 4(2):162–7, 2003.

Bibliography

- [96] P. Thomsen, K. Roepstorff, M. Stahlhut, and B. van Deurs. Caveolae are highly immobile plasma membrane microdomains, which are not involved in constitutive endocytic trafficking. *Mol Biol Cell*, 13(1):238–50, 2002.
- [97] W. M. Krajewska and I. Maslowska. Caveolins: structure and function in signal transduction. *Cell Mol Biol Lett*, 9(2):195–220, 2004.
- [98] M. P. Lisanti, Z. Tang, P. E. Scherer, E. Kubler, A. J. Koleske, and M. Sargiacomo. Caveolae, transmembrane signalling and cellular transformation. *Mol Membr Biol*, 12(1):121–4, 1995.
- [99] B. D. Grant and J. G. Donaldson. Pathways and mechanisms of endocytic recycling. *Nature reviews. Molecular cell biology*, 10(9):597–608, 2009.
- [100] B. Qualmann, M. M. Kessels, and R. B. Kelly. Molecular links between endocytosis and the actin cytoskeleton. *J Cell Biol*, 150(5):F111–6, 2000.
- [101] C. J. Merrifield, M. E. Feldman, L. Wan, and W. Almers. Imaging actin and dynamin recruitment during invagination of single clathrin-coated pits. *Nature Cell Biology*, 4(9):691–698, 2002.
- [102] C. J. Merrifield, B. Qualmann, M. M. Kessels, and W. Almers. Neural wiskott aldrich syndrome protein (n-wasp) and the arp2/3 complex are recruited to sites of clathrin-mediated endocytosis in cultured fibroblasts. *European journal of cell biology*, 83(1):13–8, 2004.
- [103] L. M. Fujimoto, R. Roth, J. E. Heuser, and S. L. Schmid. Actin assembly plays a variable, but not obligatory role in receptor-mediated endocytosis in mammalian cells. *Traffic*, 1(2):161–71, 2000.
- [104] T. A. Gottlieb, I. E. Ivanov, M. Adesnik, and D. D. Sabatini. Actin microfilaments play a critical role in endocytosis at the apical but not the basolateral surface of polarized epithelial cells. *The Journal of cell biology*, 120(3):695–710, 1993.
- [105] H. Girao, M. I. Geli, and F. Z. Idrissi. Actin in the endocytic pathway: from yeast to mammals. *FEBS letters*, 582(14):2112–9, 2008.
- [106] K. Matter, K. Bucher, and H. P. Hauri. Microtubule perturbation retards both the direct and the indirect apical pathway but does not affect sorting of plasma membrane proteins in intestinal epithelial cells (caco-2). *The EMBO journal*, 9(10):3163–70, 1990.
- [107] T. Soldati and M. Schliwa. Powering membrane traffic in endocytosis and recycling. *Nature Reviews Molecular Cell Biology*, 7(12):897–908, 2006.
- [108] G. Apodaca. Endocytic traffic in polarized epithelial cells: role of the actin and microtubule cytoskeleton. *Traffic*, 2(3):149–59, 2001.
- [109] A. Piasek and J. Thyberg. Effects of colchicine on endocytosis of horseradish peroxidase by rat peritoneal macrophages. *Journal of cell science*, 45:59–71, 1980.

- [110] M. Gekle, S. Mildenerger, R. Freudinger, G. Schwerdt, and S. Silbernagl. Albumin endocytosis in ok cells: dependence on actin and microtubules and regulation by protein kinases. *The American journal of physiology*, 272(5 Pt 2):F668–77, 1997.
- [111] M. K. Pratten and J. B. Lloyd. Effects of temperature, metabolic inhibitors and some other factors on fluid-phase and adsorptive pinocytosis by rat peritoneal macrophages. *The Biochemical journal*, 180(3):567–71, 1979.
- [112] R. Gronheid, J. Hofkens, F. Kohn, T. Weil, E. Reuther, K. Mullen, and F. C. De Schryver. Intramolecular forster energy transfer in a dendritic system at the single molecule level. *J Am Chem Soc*, 124(11):2418–9, 2002.
- [113] A. Dubois, M. Canva, A. Brun, F. Chaput, and J. P. Boilot. Photostability of dye molecules trapped in solid matrices. *Appl Opt*, 35(18):3193–9, 1996.
- [114] A. Margineanu, J. Hofkens, M. Cotlet, S. Habuchi, A. Stefan, J. Q. Qu, C. Kohl, K. Müllen, J. Vercammen, Y. Engelborghs, T. Gensch, and F. C. De Schryver. Photophysics of a water-soluble rylene dye: Comparison with other fluorescent molecules for biological applications. *Journal of Physical Chemistry B*, 108(32):12242–12251, 2004.
- [115] C. Jung, B. K. Müller, D. C. Lamb, F. Nolde, K. Müllen, and C. Bräuchle. A new photostable terrylene diimide dye for applications in single molecule studies and membrane labeling. *J Am Chem Soc*, 128(15):5283–91, 2006.
- [116] L. Feiler, H. Langhals, and K. Polborn. Synthesis of perylene-3,4-dicarboximides - novel highly photostable fluorescent dyes. *Liebigs Annalen*, (7):1229–1244, 1995.
- [117] H. Kaiser, J. Lindner, and H. Langhals. Synthesis of nonsymmetrically substituted perylene fluorescent dyes. *Chemische Berichte*, 124(3):529–535, 1991.
- [118] H. Langhals. Synthesis of highly pure perylene fluorescent dyes in large-scale amounts - specific preparation of atropic isomers. *Chemische Berichte-Recueil*, 118(11):4641–4645, 1985.
- [119] J. L. Yan, M. C. Estevez, J. E. Smith, K. M. Wang, X. X. He, L. Wang, and W. H. Tan. Dye-doped nanoparticles for bioanalysis. *Nano Today*, 2(3):44–50, 2007.
- [120] M. Schneider and K. Muellen. Hybrid materials doped with covalently bound perylene dyes through the sol-gel process. *Chemistry of Materials*, 12(2):352–362, 2000.
- [121] Y. Luo and J. Lin. Solvent induced different morphologies of bis(propyl)triethoxysilane substituted perylenediimide and their optical properties. *Journal of Colloid and Interface Science*, 297(2):625–630, 2006.
- [122] W. Stoeber, A. Fink, and E. Bohn. Controlled growth of monodisperse silica spheres in micron size range. *Journal of Colloid and Interface Science*, 26(1):62, 1968.

Bibliography

- [123] N. Jungmann, M. Schmidt, M. Maskos, J. Weis, and J. Ebenhoch. Synthesis of amphiphilic poly(organosiloxane) nanospheres with different core-shell architectures. *Macromolecules*, 35(18):6851–6857, 2002.
- [124] N. Jungmann, M. Schmidt, J. Ebenhoch, J. Weis, and M. Maskos. Dye loading of amphiphilic poly(organosiloxane) nanoparticles. *Angewandte Chemie-International Edition*, 42(15):1714–1717, 2003.
- [125] C. Roos, M. Schmidt, J. Ebenhoch, F. Baumann, B. Deubzer, and J. Weis. Design and synthesis of molecular reactors for the preparation of topologically trapped gold clusters. *Advanced Materials*, 11(9):761–766, 1999.
- [126] C. Bantz and M. Maskos. personal communication, 2010.
- [127] S. Utech, C. Scherer, and M. Maskos. Multifunctional, multicompartment polyorganosiloxane magnetic nanoparticles for biomedical applications. *Journal of Magnetism and Magnetic Materials*, 321(10):1386–1388, 2009.
- [128] U. Wiesner, D. R. Larson, H. Ow, H. D. Vishwasrao, A. A. Heikal, and W. W. Webb. Silica nanoparticle architecture determines radiative properties of encapsulated fluorophores. *Chemistry of Materials*, 20(8):2677–2684, 2008.
- [129] A. Elsaesser, A. Taylor, G. S. de Yanes, G. McKerr, E. M. Kim, E. O’Hare, and C. V. Howard. Quantification of nanoparticle uptake by cells using microscopical and analytical techniques. *Nanomedicine*, 5(9):1447–57, 2010.
- [130] H. Suzuki, T. Toyooka, and Y. Ibuki. Simple and easy method to evaluate uptake potential of nanoparticles in mammalian cells using a flow cytometric light scatter analysis. *Environ Sci Technol*, 41(8):3018–24, 2007.
- [131] O. Lunov, T. Syrovets, C. Loos, J. Beil, M. Delacher, K. Tron, G. U. Nienhaus, A. Musyanovych, V. Mailänder, K. Landfester, and T. Simmet. Differential uptake of functionalized polystyrene nanoparticles by human macrophages and a monocytic cell line. *ACS Nano*, 5(3):1657–69, 2011.
- [132] W. K. Oh, S. Kim, M. Choi, C. Kim, Y. S. Jeong, B. R. Cho, J. S. Hahn, and J. Jang. Cellular uptake, cytotoxicity, and innate immune response of silica-titania hollow nanoparticles based on size and surface functionality. *ACS Nano*, 4(9):5301–13, 2010.
- [133] K. de Bruin, N. Ruthardt, K. von Gersdorff, R. Bausinger, E. Wagner, M. Ogris, and C. Bräuchle. Cellular dynamics of egf receptor-targeted synthetic viruses. *Mol Ther*, 15(7):1297–305, 2007.
- [134] A. M. Sauer, K. G. de Bruin, N. Ruthardt, O. Mykhaylyk, C. Plank, and C. Bräuchle. Dynamics of magnetic lipoplexes studied by single particle tracking in living cells. *J Control Release*, 137(2):136–45, 2009.

- [135] R. Pepperkok and J. Ellenberg. High-throughput fluorescence microscopy for systems biology. *Nature reviews. Molecular cell biology*, 7(9):690–6, 2006.
- [136] H. Peng, Z. Ruan, F. Long, J. H. Simpson, and E. W. Myers. V3d enables real-time 3d visualization and quantitative analysis of large-scale biological image data sets. *Nature biotechnology*, 28(4):348–53, 2010.
- [137] R. Henriques, M. Lelek, E. F. Fornasiero, F. Valtorta, C. Zimmer, and M. M. Mhlanga. Quickpalm: 3d real-time photoactivation nanoscopy image processing in imagej. *Nature Methods*, 7(5):339–40, 2010.
- [138] M. Fero and K. Pogliano. Automated quantitative live cell fluorescence microscopy. *Cold Spring Harbor perspectives in biology*, 2(8):a000455, 2010.
- [139] W.S. Rasband. Image j, 1997-2011.
- [140] F. Zanella, J. B. Lorens, and W. Link. High content screening: seeing is believing. *Trends in biotechnology*, 28(5):237–45, 2010.
- [141] P. Denner, J. Schmalowsky, and S. Prechtl. High-content analysis in preclinical drug discovery. *Combinatorial chemistry & high throughput screening*, 11(3):216–30, 2008.
- [142] A. E. Carpenter, T. R. Jones, M. R. Lamprecht, C. Clarke, I. H. Kang, O. Friman, D. A. Guertin, J. H. Chang, R. A. Lindquist, J. Moffat, P. Golland, and D. M. Sabatini. Cellprofiler: image analysis software for identifying and quantifying cell phenotypes. *Genome biology*, 7(10):R100, 2006.
- [143] J. C. Waters. Accuracy and precision in quantitative fluorescence microscopy. *Journal of Cell Biology*, 185(7):1135–48, 2009.
- [144] V. Cauda, C. Argyo, and T. Bein. Impact of different pegylation patterns on the long-term bio-stability of colloidal mesoporous silica nanoparticles. *Journal of Materials Chemistry*, 20(39):8693–8699, 2010.
- [145] E. Limpert, W. A. Stahel, and M. Abbt. Log-normal distributions across the sciences: Keys and clues. *Bioscience*, 51(5):341–352, 2001.
- [146] J. Rejman, V. Oberle, I. S. Zuhorn, and D. Hoekstra. Size-dependent internalization of particles via the pathways of clathrin- and caveolae-mediated endocytosis. *Biochem J*, 377(Pt 1):159–69, 2004.
- [147] B. Alberts, A. Johnson, and J. Lewis. *Molecular Biology of the Cell*, volume 4. Garland Publishing, New York, 2002.
- [148] A. Bajaj, O. R. Miranda, I. B. Kim, R. L. Phillips, D. J. Jerry, U. H. Bunz, and V. M. Rotello. Detection and differentiation of normal, cancerous, and metastatic cells using nanoparticle-polymer sensor arrays. *Proc Natl Acad Sci U S A*, 106(27):10912–6, 2009.

Bibliography

- [149] D. Vercauteren, R. E. Vandenbroucke, A. T. Jones, J. Rejman, J. Demeester, S. C. De Smedt, N. N. Sanders, and K. Braeckmans. The use of inhibitors to study endocytic pathways of gene carriers: optimization and pitfalls. *Mol Ther*, 18(3):561–9, 2010.
- [150] J. Dausend, A. Musyanovych, M. Dass, P. Walther, H. Schrezenmeier, K. Landfester, and V. Mailänder. Uptake mechanism of oppositely charged fluorescent nanoparticles in hela cells. *Macromol Biosci*, 8(12):1135–43, 2008.
- [151] H. Raghu, N. Sharma-Walia, M. V. Veettil, S. Sadagopan, and B. Chandran. Kaposi’s sarcoma-associated herpesvirus utilizes an actin polymerization-dependent macropinocytic pathway to enter human dermal microvascular endothelial and human umbilical vein endothelial cells. *J Virol*, 83(10):4895–911, 2009.
- [152] L. H. Wang, K. G. Rothberg, and R. G. Anderson. Mis-assembly of clathrin lattices on endosomes reveals a regulatory switch for coated pit formation. *Journal of Cell Biology*, 123(5):1107–17, 1993.
- [153] D. W. Goddette and C. Frieden. Actin polymerization - the mechanism of action of cytochalasin-d. *Journal of Biological Chemistry*, 261(34):5974–5980, 1986. F2084 Times Cited:119 Cited References Count:37.
- [154] R. J. Vasquez, B. Howell, A. M. Yvon, P. Wadsworth, and L. Cassimeris. Nanomolar concentrations of nocodazole alter microtubule dynamic instability in vivo and in vitro. *Mol Biol Cell*, 8(6):973–85, 1997.
- [155] Y. Zhang, L. Hu, D. Yu, and C. Gao. Influence of silica particle internalization on adhesion and migration of human dermal fibroblasts. *Biomaterials*, 31(32):8465–74, 2010.
- [156] S. E. Gratton, P. A. Ropp, P. D. Pohlhaus, J. C. Luft, V. J. Madden, M. E. Napier, and J. M. DeSimone. The effect of particle design on cellular internalization pathways. *Proc Natl Acad Sci U S A*, 105(33):11613–8, 2008.
- [157] H. Lodish, A. Berk, S. L. Zipursky, P. Matsudaira, D. Baltimore, and J. Darnell. *Molecular Cell Biology*, volume 4. Freeman, New York, 1999.
- [158] F. Denizot and R. Lang. Rapid colorimetric assay for cell growth and survival. modifications to the tetrazolium dye procedure giving improved sensitivity and reliability. *J Immunol Methods*, 89(2):271–7, 1986.
- [159] G. Haslam, D. Wyatt, and P. A. Kitos. Estimating the number of viable animal cells in multi-well cultures based on their lactate dehydrogenase activities. *Cytotechnology*, 32(1):63–75, 2000.
- [160] E. Chang, N. Thekkek, W. W. Yu, V. L. Colvin, and R. Drezek. Evaluation of quantum dot cytotoxicity based on intracellular uptake. *Small*, 2(12):1412–7, 2006.

- [161] R. E. Serda, J. H. Go, R. C. Bhavane, X. W. Liu, C. Chiappini, P. Decuzzi, and M. Ferrari. The association of silicon microparticles with endothelial cells in drug delivery to the vasculature. *Biomaterials*, 30(13):2440–2448, 2009.
- [162] Y. Jin, S. Kannan, M. Wu, and J. X. Zhao. Toxicity of luminescent silica nanoparticles to living cells. *Chem Res Toxicol*, 20(8):1126–33, 2007.
- [163] A. Wixforth. Acoustically driven planar microfluidics. *Superlattices and Microstructures*, 33(5-6):389–396, 2003.
- [164] Z. Guttenberg, A. Rathgeber, S. Keller, J. O. Rädler, A. Wixforth, M. Kostur, M. Schindler, and P. Talkner. Flow profiling of a surface-acoustic-wave nanopump. *Phys Rev E Stat Nonlin Soft Matter Phys*, 70(5 Pt 2):056311, 2004.
- [165] A. Wixforth, C. Strobl, Ch Gauer, A. Toegl, J. Scriba, and Z. v Guttenberg. Acoustic manipulation of small droplets. *Analytical and Bioanalytical Chemistry*, 379(7-8):982–91, 2004.
- [166] T. Anor, L. Grinberg, H. Baek, J. R. Madsen, M. V. Jayaraman, and G. E. Karniadakis. Modeling of blood flow in arterial trees. *Wiley Interdiscip Rev Syst Biol Med*, 2(5):612–23, 2010.
- [167] G. M. London and B. Pannier. Arterial functions: how to interpret the complex physiology. *Nephrol Dial Transplant*, 25(12):3815–23, 2010.
- [168] C. Seiler. The human coronary collateral circulation. *Eur J Clin Invest*, 40(5):465–76, 2010.
- [169] S. Hu and L. V. Wang. Photoacoustic imaging and characterization of the microvasculature. *J Biomed Opt*, 15(1):011101, 2010.
- [170] S. J. Tang, M. L. Gordon, V. X. Yang, M. E. Faughnan, M. Cirocco, B. Qi, E. S. Yue, G. Gardiner, G. B. Haber, G. Kandel, P. Kortan, A. Vitkin, B. C. Wilson, and N. E. Marcon. In vivo doppler optical coherence tomography of mucocutaneous telangiectases in hereditary hemorrhagic telangiectasia. *Gastrointestinal Endoscopy*, 58(4):591–8, 2003.
- [171] D. R. Larson, W. R. Zipfel, R. M. Williams, S. W. Clark, M. P. Bruchez, F. W. Wise, and W. W. Webb. Water-soluble quantum dots for multiphoton fluorescence imaging in vivo. *Science*, 300(5624):1434–6, 2003.
- [172] M. Oda, H. Yokomori, and J. Y. Han. Regulatory mechanisms of hepatic microcirculation. *Clin Hemorheol Microcirc*, 29(3-4):167–82, 2003.
- [173] F. Strobl. *Diplomarbeit Zur Interaktion von Lipidmembranen und Nanopartikeln*. Diploma thesis, 2011.
- [174] T. Heimburg. *Thermal Biophysics of Membranes*. Wiley-VCH, 2007.
- [175] L. Miao, U. Seifert, M. Wortis, and H. G. Dobereiner. Budding transitions of fluid-bilayer vesicles - the effect of area-difference elasticity. *Physical Review E*, 49(6):5389–5407, 1994.

Bibliography

- [176] R. Lipowsky and H. G. Dobereiner. Vesicles in contact with nanoparticles and colloids. *Europhysics Letters*, 43(2):219–225, 1998.
- [177] R. D. Kornberg and H. M. McConnell. Inside-outside transitions of phospholipids in vesicle membranes. *Biochemistry*, 10(7):1111–20, 1971.
- [178] G. Baier, C. Costa, A. Zeller, D. Baumann, C. Sayer, P. H. Araujo, V. Mailänder, A. Musyanovych, and K. Landfester. Bsa adsorption on differently charged polystyrene nanoparticles using isothermal titration calorimetry and the influence on cellular uptake. *Macromolecular bioscience*, 11(5):628–38, 2011.

Appendix: Deposition of Nanoparticles

Referring to the experiments dealing with the celltype dependent nanoparticle uptake and cytotoxicity which were presented in Chapter 7, the deposition behavior of nanoparticles in the given experimental environment was investigated. It was aimed on correlating the uptake of nanoparticles into cells to the number of particles reaching the cells by sedimentation and diffusion. Due to local convection in small parts of the fluid, which could not be avoided due to the experimental conditions, and the therefore very komplex interplay between sedimentation, diffusion and convection driven movement of nanoparticles, the analysis of the data exceeds the scope of this work. It was therefore not presented in relation with the above mentioned experiments but will be discussed in the following section.

An important aspect of nanoparticle cytotoxicity investigations is dosimetry. It has been shown by several publications that the response of cells upon nanoparticle contact is dependent on the amount of nanoparticles presented to the cells. An overview of these publications can be found in section 2.2.4. The number of particles in contact with the cells depends on the amount of nanoparticles added to the sample as well as on their deposition properties. Depending on the size and density of the particles an interplay between diffusion and sedimentation takes place. Both processes evoke different types of nanoparticle-cell interactions. Sedimentation leads to a nanoparticle deposition on the cellular membrane and therefore to long contact times between the nanoparticles and the cell. Diffusing particles shortly bump into the cell surface and are immediately released again if not getting caught by a receptor, in a surface structure or by electrostatic interactions. The influence of sedimentation and diffusion on cellular uptake was previously studied with differently sized gold nanoparticles by comparing cellular nanoparticle uptake in standard and inverted cell cultures [53]. In standard cell cultures, the cells are growing at the bottom of the well allowing nanoparticles to reach them via sedimentation and diffusion. In the inverted geometry, cells are placed into the cell medium from the upper side, facing towards the bottom of the well. Nanoparticles can only interact with these cells via diffusion. Cells in the standard configuration showed an increased nanoparticle uptake compared to the inverted cells. The differences in particle uptake were strongly dependent on particle size. While the 15 nm gold particles showed only slight differences in uptake, about 5 times more particles were taken up by cells in standard cell culture than in the inverted one when the particles had a size of 118 nm.

To estimate the influence of nanoparticle deposition in our experiments, we investigated the deposition behavior of the MPD-SiO₂-310 nanoparticles on collagen coated coverslides for three different nanoparticle concentrations. We used $6.0 \cdot 10^8$ particles per well, the concentration applied for the cellular uptake experiments and $1.5 \cdot 10^9$ as well as $3.0 \cdot 10^9$ nanoparticles per well, corresponding to two concentrations used for cytotoxicity assessment studies. The nanoparticles were dispersed in cell media, and the mixture was transferred into one well of the Lab-Tek-chambered cover slides (NUC, Rochester, NY, USA). Nanoparticle deposition was monitored by measuring stacks of confocal images of the nanoparticles lying on the coverslide by confocal spinning disk microscopy. The deposition was monitored regularly at least within the first 6 h after nanoparticle addition. Fur-

Appendix: Deposition of Nanoparticles

thermore additional images were captured after 24 or 69 h. To avoid the influence of local inhomogeneities different regions all over the coverslide were observed. The stacks of confocal cross-sections were evaluated by the `Outside_Region` routine of the custom-made `Nano_In_Cell_3D` software described in Chapter 6. Briefly, this routine integrates over the intensity in the region of interest and calculates the number of particles present in the observed region by dividing the total intensity by the intensity of a single particle. The number of deposited nanoparticles per well was extrapolated and then plotted against the deposition time.

Figure 7 depicts the deposition curves for the three different concentrations and an overlay of all datasets. All curves follow the same trend. The number of nanoparticles deposited on the coverslide initially increases within the first 3 to 6 hours before reaching a constant value. Interestingly, after 24 or 69 h the number of nanoparticles deposited on the coverslide is significantly decreased compared to the number of particles observed after 6 h for the lowest concentration (see Figure 7 a). This effect is also clearly visible in the corresponding confocal images which are depicted in Figure 8. After 24 or 69 h considerably less particles can be observed compared to the images taken after 6 or 8 h. This trend does not exist when the deposition of $1.5 \cdot 10^9$ nanoparticles per well is observed (see Figure 7 b).

A possible explanation for this effect would be that the concentration of free nanoparticles in solution is reduced during long incubation times. Therefore, less particles are expected to stay settled on the coverslide provided an equilibrium between nanoparticle sedimentation and diffusion. One possible process leading to a decrease in the concentration of free nanoparticles would be an attachment of nanoparticles to the walls of the Lab Tex-chambered cover slides. The walls of the coverslide are made of polystyrene, a non-charged polymer. Polystyrene, in the form of nanoparticles has a slightly negative surface charge which can be explained by the absorption of hydroxyl ions at their surface [178]. The protein bovine serum albumin has been shown to attach to polystyrene particles despite being negatively charged as well. We therefore think that proteins which are present in the cell medium might mediate an interaction between the negatively charged silica nanoparticles and the polystyrene walls of the coverslide and lead to a stable attachment. For higher concentration the number of particles attaching to the walls may be negligible compared to the number of particles added to the sample resulting in constant numbers of deposited particles. For the highest concentration investigated it was not possible to evaluate the datasets obtained after 24 h as too many particles had deposited. During evaluation, the mean intensity of a single nanoparticle (*IntDens_NP*) is used to estimate the number of particles within one stack of confocal cross-sections. To account for possible variations in the external settings as e.g. the laser intensity, this *IntDens_NP* is reassessed from time to time. Due to the long gap between the individual measurements the *IntDens_NP* needed to be recalculated for the 24 h measurements as major changes in the external settings might have occurred. However, due to the vast amount of nanoparticles present in the images it was not possible to obtain the *IntDens_NP* and therefore calculate the number of deposited particles for this dataset.

To test whether the observed deposition behavior is in agreement with theoretical values, we calculated the "gravitationally driven deposition rate" V [52] applying Stokes' law (Equation 0.1)

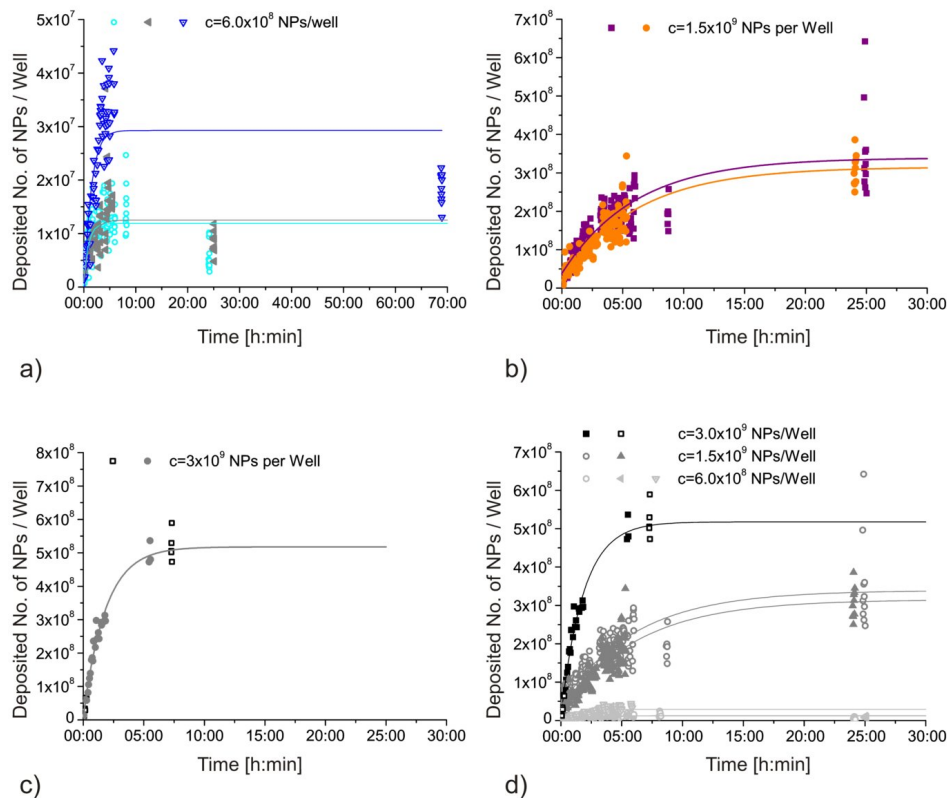


Figure 7: Deposition behavior of MPD-SiO₂-310 nanoparticles at three different concentrations. The deposited number of particles increases within the first 3 to 6 hours before reaching a constant value. a) Deposition curve for $6.0 \cdot 10^8$ nanoparticles per well. The number of deposited nanoparticles is strongly reduced after 24 of 69 h. This decrease can be explained by nanoparticle adsorption on the walls of the Lab-Tek-chambered cover slides removing particles from the solution. This effect is not visible in the deposition curve of b) $1.5 \cdot 10^9$ particles per well. Due to the increased concentration, the binding of particles to the walls is probably negligible. c) Deposition behavior observed at a concentration of $3.0 \cdot 10^9$ nanoparticles per well. Long term data could not be evaluated due to the huge number of particles present on the coverslide. d) Overlay of all deposition curves shown before.

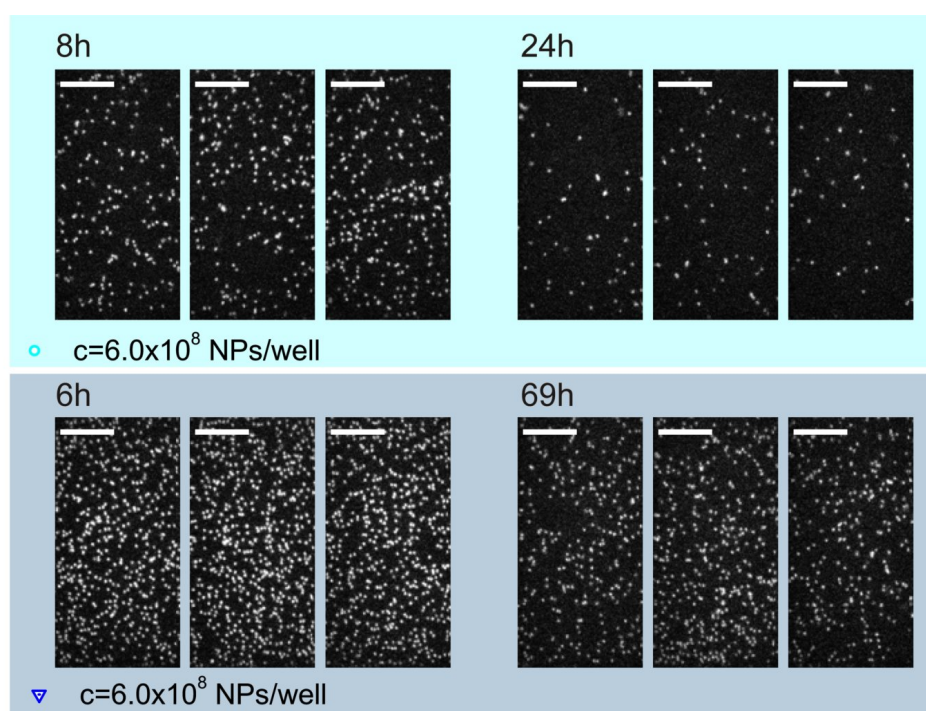


Figure 8: Representative confocal images of particles deposited on the coverslide. The upper images show nanoparticle deposition after 8 and 24 h in one experiment, the lower images originate from a second experiment and represent nanoparticle deposition after 6 and 69 h. The corresponding deposition curves (cyan and blue) can be seen in Figure 7. Scalebar. 5 μm

and used the Stokes-Einstein equation to assess the diffusion coefficient D (Equation 0.2) [52].

$$V = \frac{g(\rho_p - \rho_f)d^2}{18\mu} \quad (0.1)$$

The "gravitationally driven deposition rate" V [52] is dependent on the acceleration due to gravity g , the density of the fluid ρ_f and of the particles ρ_p , the diameter of the particles d and the viscosity of the fluid μ . The diffusion coefficient D is dependent on the temperature T , the particle diameter and the viscosity of the fluid. R is the gas constant and N_A the Avogadro's number.

$$D = \frac{RT}{3N_A\mu d} \quad (0.2)$$

The calculation results in a "gravitationally driven deposition rate" V of 226 $\mu\text{m}/\text{h}$ for the MPD-SiO₂-310 nanoparticles in cell medium. To plot the sedimentation curve, we assumed an homogeneous particle distribution in solution. All particles with a distance of 226 μm from the coverslide will sediment within one hour if no diffusion takes place. After 2 h all particles within 452 μm coverslide distance reach the coverslide. In Figure 9, the calculated sedimentation curve is overlaid with the experimentally obtained data. The black curves correspond to the sedimentation of the MPD-SiO₂-310 nanoparticles. In addition, the sedimentation behavior of hypothetic aggregates having a diameter of twice the nanoparticle radius was calculated. These aggregates have a "sedimentation rate" V of 900 $\mu\text{m}/\text{h}$ (shown in gray). The experimentally observed deposition behavior shows similarities to the calculated data. At the very beginning of the deposition experiments, the slopes of the deposition curves have the same order of magnitude as the calculated sedimentation curves, pointing out the influence of sedimentation. On longer timescales nanoparticle diffusion becomes more pronounced leading to a bending of the curves. With increasing nanoparticle concentration (compare Figure 9 a - c), the slope of the deposition curves increases slightly probably showing the increasing influence of nanoparticle aggregation. The influence of nanoparticle diffusion was estimated by calculating the diffusion coefficient of the particles. The monodisperse particles have a diffusion coefficient of 1.5 $\mu\text{m}^2/\text{s}$ corresponding to an average displacement of about 73 μm within one hour. Both sedimentation and diffusion therefore lead to a displacement in the micrometer range. This indicates that both sedimentation and diffusion should contribute to the deposition behavior observed. In addition to these processes the nanoparticles were influenced by convection of the cell medium. This convection was probably evoked by local heating in the chamber due to the laser and the heating plate as well as by movements of the sample chamber due to focussing and looking for a new region of interest and could therefore not be avoided.

The fraction of nanoparticles that deposits compared to the added nanoparticle number is calculated from the constant values reached on longer time scales. The individual percentages of deposited particles are shown in table 1.

The percentage of deposited particles strongly increases between the lowest and the two higher concentrations. Nevertheless only a part of added particles is deposited in all cases. This could have several reasons. On the one hand, particles are probably removed from the medium by attachment to the walls. These particles are not available for deposition. This effect is more significant for lower

Appendix: Deposition of Nanoparticles

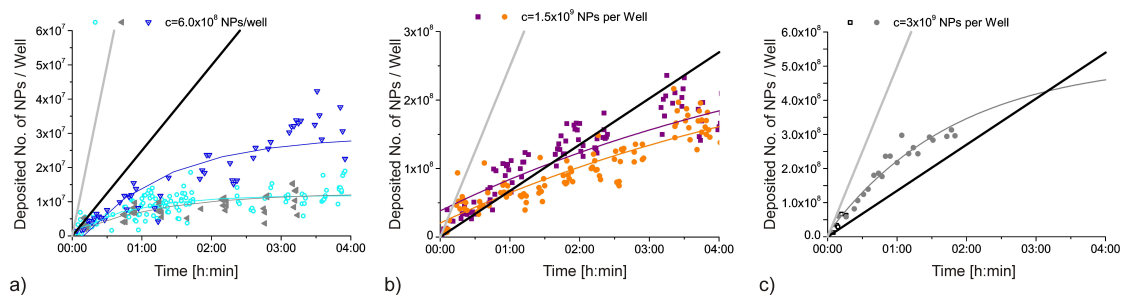


Figure 9: Comparison of the experimentally observed nanoparticle deposition with the pure sedimentation behavior expected from calculations for monodisperse nanoparticles (black line) and hypothetical aggregates having twice the nanoparticle diameter (gray line). At the very beginning of the experiments both the experimentally observed deposition behaviors and the calculated sedimentation curves are in good agreement. Nevertheless, with increasing concentration from a) $6.0 \cdot 10^8$ to b) $1.5 \cdot 10^9$ and to c) $3.0 \cdot 10^9$, the experimentally observed deposition increases and approaches the gray line, indicating nanoparticle aggregation. On longer time scales, diffusion processes clearly influence the deposition behavior leading to a bending in the deposition curve.

Number of added NPs / well	Percentage of deposited NPs
$3.0 \cdot 10^9$	17 %
$1.5 \cdot 10^9$	22 %
	21 %
$3 \cdot 10^8$	5 %
	2 %
	2 %

Table 1: Estimated percentage of deposited MPD-SiO₂-310 nanoparticles (NPs) onto a collagen coated coverslide for the three different concentrations $6.0 \cdot 10^8$, $1.5 \cdot 10^9$ and $3.0 \cdot 10^9$ nanoparticles per well.

then for higher concentrations leading to an increase deposition. On the other hand, nanoparticle agglomeration influences the deposition behavior. Agglomeration is known to be a concentration dependent effect. If more particles are present in solution, more and bigger aggregates are likely to be formed. The increased size of the particle then leads to a stronger influence of particle sedimentation compared to diffusion and therefore to a higher number of deposited nanoparticles. This was also apparent within the fluorescence images where the images of the lowest nanoparticle concentration revealed very homogeneous individual fluorescent spots, whereas for higher concentrations agglomerates emerged. Nevertheless, as diffusional processes strongly influence nanoparticle deposition behavior at the used nanoparticle size range, many particles will stay in solution. Furthermore, due to the experimental conditions, fluid convection cannot be avoided. This additional movement of the fluid strongly influences the nanoparticle deposition behavior. A final conclusion about the deposition behavior of nanoparticle in this system cannot be drawn and further experiments are needed to obtain the full picture of all processes taking place.

Acknowledgements

Many people have contributed to this work and I hereby want to express my gratitude for their support.

First of all, I'd like to thank Prof. C. Bräuchle for giving me the opportunity to work in his group and on this interesting topic. Furthermore I'd like to thank him for his continuous support and encouragement.

I also owe many thanks to my colleges within the SPP 1313 Project: Prof. Armin Reller, Prof. Achim Wixforth, Prof. Matthias F. Schneider, Prof. Stefan W. Schneider and Prof. Ingrid Hilger, as well as to Dr. Rudolf Herrmann, Dr. Christoph Westerhausen, Florian Strobl, Dr. Jürgen Neumann, Dr. Alexander Bauer, Dr. Elwira Strozyk and Claudia Strobel. It was a pleasure for me to work together with you on this project and I always enjoyed our meetings and discussions. Especially I'd like to thank Rudi for his continuous fight to improve and optimize the nanoparticles, for immediately answering all my questions and for sending me new particles whenever I needed some. Without this great support a lot of things would not have been possible! Furthermore I'd like to thank Christian and Florian for the very enjoyable and productive time during our experiments with the lipid vesicles and for their support in proof-reading this thesis. In addition I'd like to thank Alexander for his support with the HUVEC cells and for the great cooperation while investigating the cytotoxic impact of nanoparticles on the different cell lines.

I furthermore want to thank Prof. Christina Scheu and Dr. Daniel Kiener for providing me with TEM images, and for their help and support. I had a lot of fun working on the overlay of TEM and widefield fluorescence images and learned a lot during the experiments.

In addition I'd like to thank Prof. Thomas Bein and Christian Argyo for preparing the quenchable nanoparticles and for the good discussions.

My deepest thanks go to my colleagues. Above all to Anna Sauer, Frauke König and Dorothee Schupp who became true friends. I'm more than grateful for all the time I could spend with you! It was always great and I learned a lot from your professionalism, your ideas, your creativity and your assertiveness! I wish you all the best for your future and I hope we will keep in touch!

Adriano, it was a pleasure supervising you during your diploma thesis! And I am very happy that you joined the work on the SPP1313 project. With all your great ideas you are a gain for the project and the workgroup!

In addition I'd like to thank my Master Student Ellen Broda for the nice time we had while working on the project and for all her commitment throughout her work.

I extend my warmest appreciations to Martin Sikor, Robert Lewis, Aurelie Dupont, Adam Muschielok, Veronika Weiss and Christoph Jung and all the other colleagues of the AK Bräuchle, Michaelis and Lamb who made life at university so pleasant. I am grateful for all the help you gave me no matter if I needed an explanation, an assistance or just a good laugh!

A special thank goes to our "Cell-Queen" Monika Franke. Thank you for taking such good care of the cells and for helping me wherever you could, especially while fighting with the HMEC-1 and HUVEC cells! Another special thank goes to Dr. Moritz Ehrl, for organizing all the "little things" and for stepping in whenever the worst comes to the worst! In addition I'd like to express my thanks to Silke Steger for helping me with all the bureaucratic things.

Acknowledgements

I also thank my students Julia Janik, Annekathrin Ranft and Alexander André. It was a pleasure working with you and I wish you all the best for your future studies! I was also fortunate to benefit from the support of the IDK-NBT. Above all from the great support of Marilena Pinto. Thank you so much for organizing all the talks and events from which I benefited so much during the last years! This thesis would not have been possible without the financial support of the DFG (SPP 1313), IDK-NBR, CeNS, CiPS and NIM.

Last but not least I want to thank some very special people. First, I want to express my deepest gratitude to my parents! Thank you for always believing in me, for your continuous support and your confidence! Without you many things would not have been possible!

In addition my deepest thanks go to my husband Ondrej! I was fortunate to benefit from your love and support throughout the last years and I hereby want to express my gratefulness! I'm looking forward to all the future adventures we will experience during the years to come! Little David, thank you for bringing the sun to my life, for your catching laugh and your curiosity! Being with you is never boring!

List of publications

Peer-reviewed publications (included in this work)

J. Blechinger, R. Herrmann, D. Kiener, F. J. García-García, C. Scheu, A. Reller, and C. Bräuchle. Perylene-labeled silica nanoparticles: synthesis and characterization of three novel silica nanoparticle species for live-cell imaging. *Small*, **6**(21):2427-35, 2010.

J. Blechinger*, A. A. Torrano*, C. Argyo, A. Reller, T. Bein, and C. Bräuchle. A fast analysis method to quantify nanoparticle uptake on a single cell level. *submitted to Nanomedicine*, 2011.

J. Blechinger*, A. T. Bauer*, A. A. Torrano, C. Gorzelanny, C. Bräuchle, S. W. Schneider. Silica Nanoparticles: Nanotoxicity is dependent on the uptake behavior of the cell and therefore cell type dependent. *submitted to Small*, 2012.

* contributed equally

Peer-reviewed publications (not included in this work)

Fredrik Westerlund, Pär Nordell, Julia Blechinger, Teresa M. Santos, Bengt Nordén and Per Lincoln. Complex DNA-Binding Kinetics Resolved by Combined Circular Dichroism and Luminescence Analysis. *The Journal of Physical Chemistry*, **112**(21):6688-94, 2008

Timo Lebold, Julia Blechinger, Lea Mühlstein, Jens Michaelis, Thomas Bein, Klaus Müllen and Christoph Bräuchle. Mesopore functionalization as highly specific tool for the control of single molecule dynamics in silica materials. *Chemistry - A European Journal*, **15**(7):1661-72, 2009

List of publications

Oral presentations

J. Blechinger, Characterization of fluorescence properties and morphology of labeled nanoparticles for live-cell imaging of nanoparticle-cell interactions, SPP 1313 Meeting, Fulda, Germany, February 2009

J. Blechinger, Uptake characteristics and trafficking of silica nanoparticles, SPP 1313 Meeting, Fulda, Germany, February 2010

J. Blechinger, Uptake behavior of SiO₂ nanoparticles into HeLa and HUVEC cells: Similarities and differences, Workshop “Zell-Internalisierung, Nanopartikeldesign und Oberflächenfunktionalisierung”, Jena, Germany, May 2010

J. Blechinger, Uptake behavior of SiO₂ nanoparticles into HeLa and HUVEC cells analyzed through scanning laser microscopy, IDK Summerschool, Aiterbach, Germany, Juli 2010

Poster presentations

J. Blechinger, N. Ruthardt, C. Bräuchle, Nanoparticles and human health- Characterization of single particles for application in live-cell imaging, Interdisciplinary school on Nano Objects in living cells from physics to physiology, Villeneuve d'Ascq, France, September 2008

AG Bräuchle, Bioactivity and cellular uptake of distinct NPs in human endothelial cells, SPP1313 Fortsetzungscolloquium, Essen, Germany, October 2010

J. Blechinger, A. A. Torrano, A. T. Bauer, R. Herrmann, A. Reller, S. W. Schneider, C. Bräuchle, Uptake kinetics, uptake pathways and cytotoxicity of SiO₂-nanoparticles interacting with HeLa and HUVEC cells, Biophysical Society Meeting, Baltimore, USA, March 2011